NREL
NATIONAL RENEWABLE ENERGY LABORATORY

Medium-Speed Drivetrain Test Report

September 1, 2002 — December 30, 2007

C. Walford, K. Lybarger, T. Lettenmaier, and D. Roberts
DNV Renewables (USA) Inc.
Seattle, Washington

NREL Technical Monitor: H. Link

NREL is a national laboratory of the U.S. Department of Energy, Office of Energy Efficiency & Renewable Energy, operated by the Alliance for Sustainable Energy, LLC.

Subcontract Report
NREL/SR-5000-51175
September 2012

Contract No. DE-AC36-08GO28308

NATIONAL RENEWABLE ENERGY LABORATORY

Medium-Speed Drivetrain Test Report

September 1, 2002 — December 30, 2007

C. Walford, K. Lybarger, T. Lettenmaier, and D. Roberts
DNV Renewables (USA) Inc.
Seattle, Washington

NREL Technical Monitor: H. Link
Prepared under Subcontract No. YAM-1-30209-01

NREL is a national laboratory of the U.S. Department of Energy, Office of Energy Efficiency & Renewable Energy, operated by the Alliance for Sustainable Energy, LLC.

National Renewable Energy Laboratory
15013 Denver West Parkway
Golden, Colorado 80401
303-275-3000 • www.nrel.gov

Subcontract Report
NREL/SR-5000-51175
September 2012

Contract No. DE-AC36-08GO28308

This publication received minimal editorial review at NREL.

NOTICE

This report was prepared as an account of work sponsored by an agency of the United States government. Neither the United States government nor any agency thereof, nor any of their employees, makes any warranty, express or implied, or assumes any legal liability or responsibility for the accuracy, completeness, or usefulness of any information, apparatus, product, or process disclosed, or represents that its use would not infringe privately owned rights. Reference herein to any specific commercial product, process, or service by trade name, trademark, manufacturer, or otherwise does not necessarily constitute or imply its endorsement, recommendation, or favoring by the United States government or any agency thereof. The views and opinions of authors expressed herein do not necessarily state or reflect those of the United States government or any agency thereof.

Available electronically at http://www.osti.gov/bridge

Available for a processing fee to U.S. Department of Energy
and its contractors, in paper, from:

U.S. Department of Energy
Office of Scientific and Technical Information
P.O. Box 62
Oak Ridge, TN 37831-0062
phone: 865.576.8401
fax: 865.576.5728
email: mailto:reports@adonis.osti.gov

Available for sale to the public, in paper, from:

U.S. Department of Commerce
National Technical Information Service
5285 Port Royal Road
Springfield, VA 22161
phone: 800.553.6847
fax: 703.605.6900
email: orders@ntis.fedworld.gov
online ordering: http://www.ntis.gov/help/ordermethods.aspx

Cover Photos: (left to right) PIX 16416, PIX 17423, PIX 16560, PIX 17613, PIX 17436, PIX 17721

Printed on paper containing at least 50% wastepaper, including 10% post consumer waste.

List of Acronyms

AC	alternating current
CARB	compact aligning roller bearing, registered trademark of SKF
CCW	counterclockwise
CW	clockwise
DAS	data-acquisition system
DC	direct current
DNG	Danish Nacelle Group
DNV	Det Norske Veritas
DOE	United States Department of Energy
DRS	DRS Electric Power Technologies
DTF	Dynamometer Test Facility
DTSC	drivetrain supervisory controller
EMF	electromotive force
FastDAS	Fast Data Acquisition System
GRT	generator rotor torque
ICP	integrated circuit piezoelectric
IGBT	insulated gate bipolar transistor
kip	kilopound
kN	kilonewton
kNm	kilonewton meter
kVA	kilovolt ampere
NREL	National Renewable Energy Laboratory
NWTC	National Wind Technology Center
PBL	planet bearing load
PSD	power spectral density
RTD	resistance temperature detector
SCADA	supervisory control and data acquisition
SGA	sun gear axial displacement
TDC	top dead center
THD	total harmonic distortion
TTA	torque tube axial displacement
TTA-SGD	torque tube and sun gear relative axial displacement
TTR	torque tube radial displacement
VAC	voltage in alternating current

Executive Summary

As part of the National Renewable Energy Laboratory (NREL) WindPACT Advanced Wind Turbine Drivetrain Design Study, Det Norske Veritas (DNV) tested a proof-of-concept drivetrain prototype using the National Wind Technology Center (NWTC) 2.5-MW Dynamometer Test Facility (DTF). The proof-of-concept test article is a full-scale, 1.5-MW integrated drivetrain consisting of a single-stage, epicyclic gearbox and close-coupled medium-speed permanent magnet generator. In addition to the innovative generator design, several developments were included in the gearbox design and also were tested. These improvements include a new type of bearing for the planet gears, a double-helical ring gear, and an axially floating output pinion.

The test objectives were to characterize the generator and gearbox, and to evaluate thermal performance, efficiency, vibration of the drivetrain, and loading in the gearbox. Characterization of the generator included measuring the magnitude and frequency content of the output voltage and current, and measuring temperatures at various locations on the stator and rotor. The gearbox characterization involved measuring the planet gear loads and alignment, the planet bearing roller loads, and the sun gear and torque tube displacements. The thermal performance was evaluated by measuring the stator temperatures, and measuring the generator coolant and gearbox lubrication temperatures and flow rates. Efficiency calculations were performed using the input-output method and the calorimetric method. The input-output method involved measuring the input mechanical power to the main shaft and the electrical output of the generator. The calorimetric efficiency was calculated by summing all of the sources of loss coming from the generator in the form of heat. The vibration of the drivetrain was measured in three orthogonal directions at two locations by using accelerometers.

During the initial testing of the 1.5-MW integrated drivetrain, one of the stator windings short-circuited. This required halting the testing and then redesigning the stator windings. The original windings were arranged in a parallel configuration and the redesigned windings were arranged in an edgewound series configuration.

The drivetrain was operated open-circuit and at several power levels ranging from 400 kW to 1,500 kW. Most test runs were conducted until the drivetrain achieved a quasi–steady state condition and the speed and power were relatively constant. A subset of the test runs was conducted until the drivetrain reached thermal equilibrium. The maximum power for which the generator was able to achieve thermal equilibrium at less than the design temperature limits was 1.0 MW.

During the generator characterization testing, the measured current values were greater than the design current values, and the measured voltage levels were less than the design voltage values. One of the causes of this discrepancy was that the design calculations assumed that the generator would operate at unity power factor. The measured power factor of the generator was lagging, however, which resulted in an increase in the current. Additionally, the design calculations did not account for the reduction in voltage caused by increased magnet temperature. The elevated current that resulted from the lagging power factor and reduced voltage caused increased conduction losses. This increased magnet temperature and caused further voltage reductions. The elevated current also caused additional voltage drop across the stator circuit, which reduced the terminal voltage even more. The relationship between voltage, current, and magnet temperature

forms a positive-feedback system in which even small perturbations can have significant effects. The analyses documented in this report were able to account for some—but not all—of the discrepancy between the measured and design current and voltage.

In general, the measured generator temperatures were greater than the design values. Comparison of the series and parallel winding configurations indicates that the series windings generated more heat and were less effective at dissipating the loss to the coolant system. At rated power the generator windings overheated relatively quickly. Calorimetric efficiency calculations showed greater-than-expected losses in the drivetrain. This suggests that the overheating of the generator is caused, at least in part, by increased loss. A portion of the increased loss can be attributed to the greater-than-expected current levels.

In addition to the calorimetric efficiency calculations, the efficiency of the drivetrain was calculated using the input-output method and calorimetric method. Comparison of input-output efficiency results from several days of testing demonstrated that input and output power measurements are not reliable enough to use to perform efficiency calculations.

The gearbox performed as expected. Ring gear strain measurements showed that the load on the ring gear teeth becomes more uniform across a given tooth as the power level increases. Measurement of the sun gear and torque tube axial displacement indicated that the spline joint between the sun gear and torque tube was effectively isolating the two parts by sliding axially. Planet bearing strain measurements showed a relatively linear relationship between mechanical load in the bearing and the input power of the gearbox. It also demonstrated that the bearing load spreads out circumferentially along the bearing as the load increases.

Table of Contents

List of Figures ..... **v**
List of Tables ..... **vii**
1 Introduction **1**
1.1 Background 1
1.2 Scope 2
1.3 Objectives 2
1.3.1 Component Characterization 2
1.3.2 Thermal Performance 5
1.3.3 Efficiency Tests 6
1.3.4 Vibration and Acoustic Noise Levels 7
2 Test Article Installation **8**
2.1 Test Article Arrangement 8
2.2 Test Articles 8
2.3 Test Facility 9
2.4 Test Article Drawings 10
3 Test Instrumentation and Data Acquisition **10**
3.1 Instrumentation 10
3.1.1 Electrical System 10
3.1.2 Motion and Mechanical Loads 10
3.1.3 Thermal 11
3.1.4 Vibration 13
3.2 Data-Acquisition Systems 13
4 Test Campaign **14**
5 Test Results **16**
5.1 Component Characterization 16
5.1.1 Generator Characterization 17
5.1.2 Harmonics 28
5.1.3 Gearbox Characterization 35
5.2 Thermal Performance 65
5.2.1 Gearbox Fluid Cooling System 65
5.2.2 Generator Stator Fluid Cooling System 65
5.2.3 Generator Rotor Air / Water Cooling System 74
5.3 Efficiency 74
5.3.1 Input-Output Method 75
5.3.2 Calorimetric Method 77
5.4 Vibration Levels 79
6 Conclusions **86**
Appendix A. Signal Lists **87**

List of Figures

Figure 1. Cutaway of test article 1
Figure 2. Generator equivalent per-phase circuit diagram 3
Figure 3. Generator phasor diagram for passive rectification, α = 0° 4
Figure 4. Drivetrain test setup 8
Figure 5. Gearbox (left); generator assembly power electronic converter (right) 9
Figure 6. Resistive thermal device locations 12
Figure 7. Top view of drivetrain with accelerometer coordinates system and accelerometer locations labeled 13
Figure 8. Generator open-circuit voltage 17
Figure 9. DC-link open-circuit voltage 18
Figure 10. Generator current versus rotor torque 19
Figure 11. Generator voltage versus main shaft speed 19
Figure 12. DC-link voltage versus main shaft speed 20
Figure 13. Generator current versus generator power 21
Figure 14. Generator voltage versus generator power 21
Figure 15. Generator power factor 22
Figure 16. Magnet temperature and generator open-circuit voltage 23
Figure 17. Stator temperatures and open-circuit generator voltage 23
Figure 18. Generator voltage drop with temperature 24
Figure 19. Generator voltage versus generator power 25
Figure 20. Generator current versus generator power 26
Figure 21. Generator current waveforms at one third rated power 27
Figure 22. Generator current waveforms at rated power 27
Figure 23. Generator voltage waveforms at one third rated power 28
Figure 24. Generator voltage waveforms at rated power 28
Figure 25. Generator current power spectral density at one third rated power 29
Figure 26. Generator current power spectral density at rated power 29
Figure 27. Generator voltage power spectral density at one third rated power 30
Figure 28. Generator voltage power spectral density at rated power 30
Figure 29. Total harmonic distortion of generator voltage and current 31
Figure 30. Cogging torque measurement test setup 31
Figure 31. Rotation scale with tics at 2-mm intervals 32
Figure 32. Static cogging torque 33
Figure 33. Generator no-load torque 33
Figure 34. Generator current imbalance 34
Figure 35. Inverter power factor 35
Figure 36. Ring gear strain gage configuration 36
Figure 37. Ring gear strain gages at X position 36
Figure 38. Ring gear strain gages at Y position 37
Figure 39. Ring gear strain gages at Z position 37
Figure 40. Measuring change in strain level 38
Figure 41. Tooth load distribution at 1,448 kW 38
Figure 42. Tooth load distribution from RGZA 40
Figure 43. Tooth load distribution from RGZB 40

Figure 44. Tooth load distribution from RGYA 41
Figure 45. Tooth load distribution from RGYB 42
Figure 46. Tooth load distribution from RGXA 42
Figure 47. Tooth load distribution from RGXB 43
Figure 48. Tooth loading caused by pinion offset 43
Figure 49. Test article cutaway 44
Figure 50. Sun gear and torque tube axial displacement 45
Figure 51. Relative sun gear and torque tube axial displacement 46
Figure 52. Torque tube radial displacements 47
Figure 53. Sun gear axial position 47
Figure 54. Torque tube axial position 48
Figure 55. Torque tube radial position 48
Figure 56. Relative axial displacement between sun gear and torque tube 48
Figure 57. Sun gear and torque tube axial displacements 49
Figure 58. Planetary gear instrumentation location 50
Figure 59. Planetary gear installed instrumentation 50
Figure 60. Planet gear axial displacement, lagging 52
Figure 61. Planet gear axial displacement, outboard 52
Figure 62. Planet gear axial displacement, leading 53
Figure 63. Planet gear axial displacement, lagging 53
Figure 64. Planet bearing, side and section view 54
Figure 65. Instrumented planet bearing 54
Figure 66. Planet bearing inner race, side view 55
Figure 67. Bearing load calibration fixture 56
Figure 68. CARB bearing calibration, PBL3 (Slot A) 57
Figure 69. Planet bearing load (PBL2) at 1,100 kW 57
Figure 70. Planet bearing load (PBL2) at 1,100 kW 58
Figure 71. Planet bearing strain gage peak loads at slot A 59
Figure 72. Planet bearing strain gage peak loads at slot B 59
Figure 73. Planet bearing strain gage peak loads, ratio of slot B to slot A 60
Figure 74. Roller load distribution 61
Figure 75. Planet bearing load distribution 61
Figure 76. Magic Roller waveform (generator power = 1,457 kW) 62
Figure 77. Magic Roller mean load (generator power = 1,457 kW) 63
Figure 78. Magic Roller load zone (generator power = 1,457 kW) 63
Figure 79. Torque response run #1 (rotor speed = 15.5 rpm) 64
Figure 80. Torque response run #2 (rotor speed = 15.5 rpm) 64
Figure 81. Gearbox lubrication system temperature 65
Figure 82. Winding temperature comparison at 600 kW 66
Figure 83. Winding temperature comparison at 700 kW 67
Figure 84. Temperature run at 1.0 MW 68
Figure 85. Temperature run at 1.2 MW 69
Figure 86. Temperature run at 1.5 MW 70
Figure 87. Design stator temperature breakdown 71
Figure 88. Stator temperature breakdown at 1.0 MW 71
Figure 89. Stator temperature comparison 72

Figure 90. Stator temperature drops at 1.0 MW 73
Figure 91. Stator temperature drop comparison 73
Figure 92. Magnet temperature 74
Figure 93. Combined gearbox and generator input-output efficiency by day 75
Figure 94. Combined gearbox and generator input-output efficiency 76
Figure 95. Power electronics and transformer input-output efficiency 76
Figure 96. Thermal image example 77
Figure 97. Gearbox calorimetric efficiency 78
Figure 98. Generator calorimetric efficiency 78
Figure 99. Combined gearbox and generator calorimetric efficiency 79
Figure 100. Velocity at one third rated power, east 80
Figure 101. Vibration at one third rated power, west 81
Figure 102. Vibration at rated power, east 82
Figure 103. Vibration at rated power, west 83
Figure 104. Magnitude of gearbox meshing frequency fundamental 84
Figure 105. Magnitude of gearbox meshing frequency second harmonic 85

List of Tables

Table 1. Generator Characterization Test Objectives 4
Table 2. Gearbox Characterization Test Objectives 5
Table 3. Thermal Performance Test Objectives 6
Table 4. Efficiency Test Objectives 6
Table 5. Vibration Test Objectives 8
Table 6. Test Article Component Manufacturer and References 9
Table 7. Component Dimensions and Weights 9
Table 8. Test System Drawing List 10
Table 9. Test Type Designations 15
Table 10. Test Matrix 16
Table A-1. Instrumentation Connected to the Drivetrain Supervisory Controller and Ported to the Dyno Data-Acquisition System (1 Hz) 87
Table A-2. Instrumentation Connected to the FastDAS System (2 kHz) 88
Table A-3. Accelerometer Signals 90
Table A-4. Calculated Channels 90

1 Introduction

1.1 Background

The Global Energy Concepts, LLC, later to become DNV Renewables (USA), participated in the National Renewable Energy Laboratory (NREL) WindPACT Advanced Wind Turbine Drivetrain Design Study (subcontract # YAM-1-30209-01). This participation was divided into three phases. Phase I was an in-depth and comprehensive investigation of innovative drivetrain designs that potentially could reduce the cost of energy for utility-scale wind turbines. At the end of Phase I, a design was selected from the viable candidates. Phase II involved detailed design and fabrication of a proof-of-concept version of the selected candidate. Phase III of the study involved testing of the final proof-of-concept drivetrain (the test article) using the National Wind Technology Center (NWTC) 2.5-MW Dynamometer Test Facility (DTF).

The test article was a full-scale, 1.5-MW integrated drivetrain. Figure 1 shows a three-dimensional cutaway of the test article drivetrain, comprised of the gearbox-generator assembly. The drivetrain was a single-stage epicyclical gearbox section close-coupled to the medium-speed (190 rpm) permanent magnet generator. The test article included a power electronic converter, which consists of a purpose-designed passive-diode rectifier and insulated gate bipolar transistor (IGBT) inverter. The power converter regulates generator torque and converts the variable frequency output of the generator power to 60 Hz. A transformer was included in the test setup only to match the 480 V output of the power converter with the 575 V service used at the DTF.

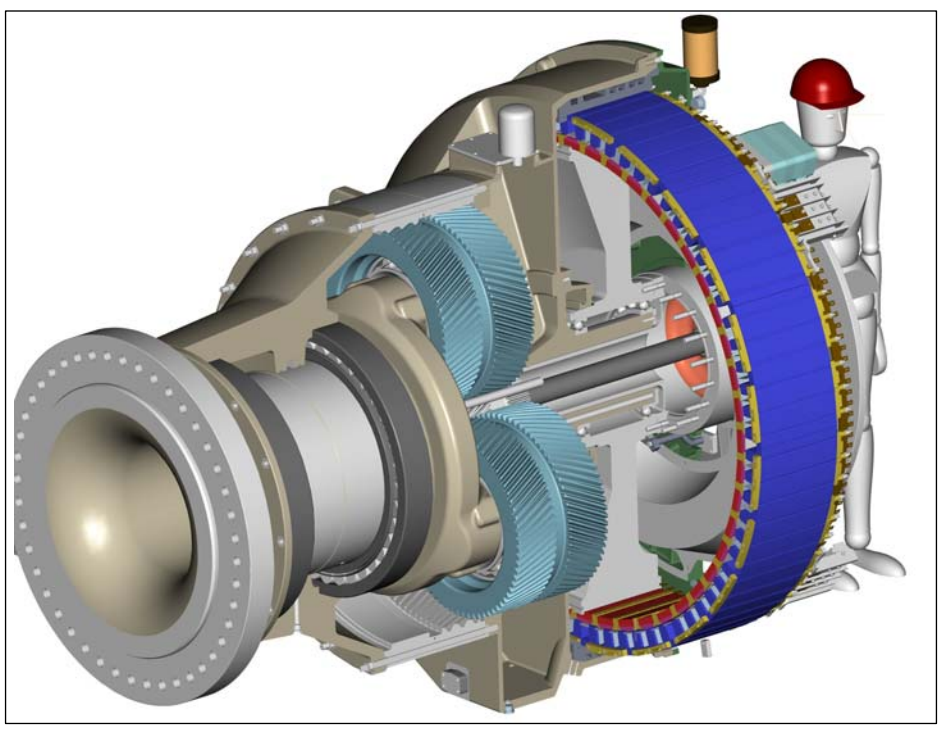

Figure 1. Cutaway of test article

During the initial testing of the 1.5-MW integrated drivetrain, one of the stator windings short-circuited. This required halting all testing and redesigning the stator windings, as described in *1.5 MW Drive Train Generator Coil Failure Event* (Global Energy Concepts, LLC, 2006). The original windings were arranged in a parallel configuration consisting of many loops of small-gage wire. The redesigned windings were arranged in an edgewound series configuration. The edgewound series configuration had much less coil turn-to-turn voltage stress, which improved robustness. The proof-of-concept article—with the redesigned stator windings—was tested at the DTF during the summer and fall of 2007. All results presented in this report are for the edgewound series generator configuration, unless otherwise noted.

1.2 Scope

This report covers the testing of the drivetrain system at the DTF. It provides an overview of the components that together comprise the entire drive system, and refers to drawing documents that define the various mechanical and electrical interfaces. This report briefly describes the test equipment, instrumentation, and procedures. A more detailed description of the test setup and procedure is provided in document N60006*, WindPACT Drive Train Test Plan*. The interconnection and integration of the various system components also is covered in a separate document, N60016, *WindPACT Drive Train Commissioning Plan* (Figure 1).[1]

1.3 Objectives

Within the overall goal of demonstrating and proving the capabilities of the DNV WindPACT drivetrain, several specific objectives motivated the test campaign, including:

- Component characterization,
- Thermal performance,
- Efficiency, and
- Vibration and acoustic noise level.

1.3.1 Component Characterization

The drivetrain is a proof-of-concept first article; therefore, assumptions about the operating characteristics of the gearbox, generator, and power electronic units were made during the design phase. The test campaign refined these assumptions by measuring internal characteristics such as deflection, impedance, and temperature rise as functions of load, speed, and time.

1.3.1.1 Generator Characterization

The WindPACT drivetrain includes a purpose-designed synchronous generator. The generator has a radial-flux permanent magnet design. The stator consists of 72 individual (salient) poles connected in four discrete quadrants; each quadrant includes all three phases in a “star” arrangement with an un-grounded neutral. The stator coils are surrounded by a water jacket to provide cooling. The rotor consists of 48 permanent-magnet poles mounted to the outer rim of a flanged disc. The rotor is mounted inside the stator and its nominal maximum rotational speed during normal operation is 191 rpm. The equivalent per-phase circuit diagram of the permanent magnet synchronous generator is shown in Figure 2. In this diagram, the assumed current flow follows the standard convention for a motor. The actual current flow for a generator will be negative if using this convention.

[1] Documents N60006 and N60016 are unpublished internal NREL reports.

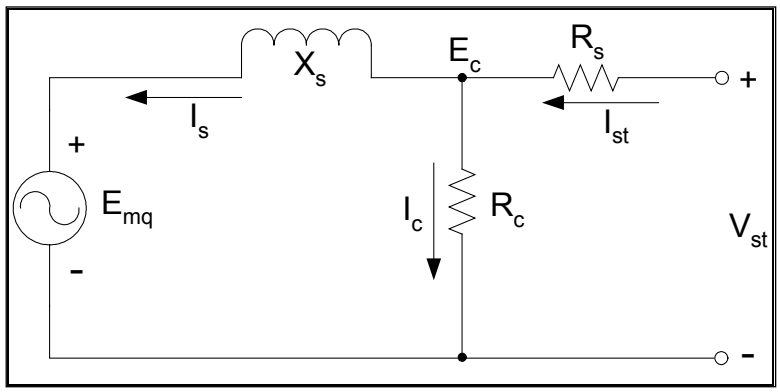

- E_{mq}—Internal electromotive force or open-circuit voltage
- X_s—Synchronous reactance
- R_s—Stator resistance
- R_c—Equivalent core loss
- V_{st}—Terminal voltage

Figure 2. Generator equivalent per-phase circuit diagram

Near the end of Phase II, a significant design change with regard to the power electronics was initiated. This change was required due to the adoption of grid codes (in particular, the low-voltage ride-through requirement) that the drivetrain would have had difficulty meeting if using the power electronics topology originally selected in Phase I. As a result of the new requirement, the NREL and DNV project team decided to replace the thyristor-based line-commutated current source converter selected in Phase I with an IGBT-based voltage-source converter. The converter utilized by Clipper Windpower in testing the DGD1 drivetrain at the DTF in 2003 was modified in October 2005 to enable its integration with the DNV drivetrain.

The output of the generator is connected to four diode-bridge rectifiers that provide DC current to four IGBT-based voltage-source inverters operated in parallel. Each 375-kW inverter accommodates one quadrant of the generator. The performance of the generator when connected to this passive rectifying power electronics system largely is determined by the generator internal electromotive force (EMF) and synchronous reactance. The relationship between these parameters and the per-phase voltages and currents is determined using the phasor diagram shown in Figure 2.

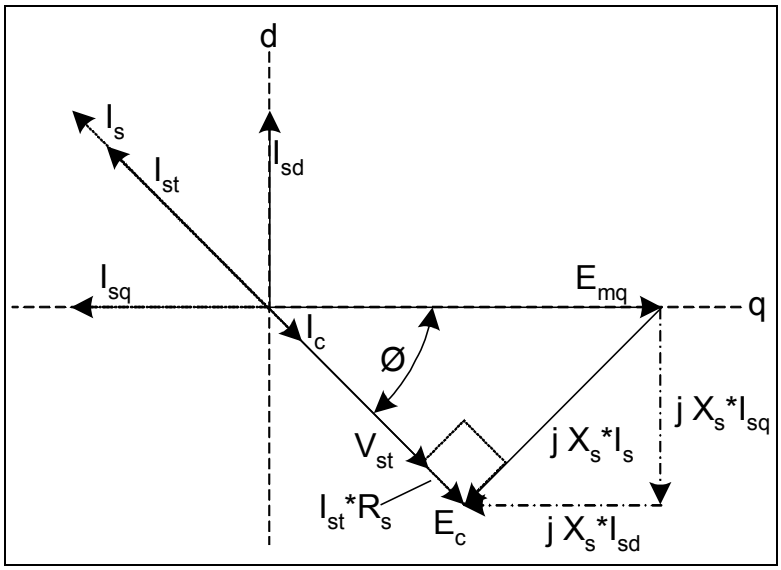

Figure 3. Generator phasor diagram for passive rectification, α = 0°

The parameters used in the circuit model shown in Figure 3 were measured during the acceptance tests performed at the assembly factory. The acceptance tests included measuring the "static" cogging torque, measuring the open-circuit voltage, validating the stator insulation scheme, and initially verifying the thermal performance of the stator cooling system under DC load. The generator was not run dynamically under load during these tests. The test campaign carried out at the DTF measured the performance of the generator when coupled to the rectifier/inverter system. Table 1 lists the objectives of the test campaign relative to the generator and power electronic system.

Table 1. Generator Characterization Test Objectives

Objective	Measurement
Measure generator electrical performance	AC voltage and current at generator terminals and DC voltage at rectifier terminals as functions of rotor torque and speed
Quantify generator electrical characteristics	Voltage and current waveforms at discrete operating points
Measure cogging torque pulsations	Generator torque variation at low speed
Characterize generator torque command transient response	Generator current and voltage waveforms, rotor torque time series
Quantify current balance between all 4 generator quadrants	Quadrant currents at discrete operating points
Evaluate converter output quality	Converter output power factor

1.3.1.2 Gearbox Characterization

The WindPACT drivetrain gearbox is a single-stage planetary (i.e., epicyclic) design with double-helical gearing. Helical gearing is preferred over spur gearing in gearboxes because it provides increased contact ratio, thereby increasing the load-carrying capacity and reducing noise generated by tooth meshing. Double-helical gearing—as opposed to single-helical—supports the sun and planet gears with the mesh itself, rather than relying on additional thrust bearings to react the axial load induced by the helix angle.

The challenge with the double-helical arrangement is that the gearing accuracy is critical to correct operation. Although tooth-to-tooth, profile, and lead accuracy are important for proper load-sharing in any planetary gearbox design, the double-helical arrangement is more demanding. Any deviation of the apexes (the theoretical intersection of each left and right helix) affects the ability of the planets to share the torque load equally.

The gearbox was manufactured with scrupulous attention paid to apex run-out. Additionally, a unique bearing was used to mount the planets to the carrier pins. This "toroidal" bearing enables the planet gear to float axially, thus allowing each planet to "follow" any run-out in the ring gear apex. This bearing also allows the planet to tilt with respect to the carrier pin so that it can accommodate any misalignment—due to errors or deflection—between the planet carrier and the ring gear.

The sun gear in this planetary arrangement is floating; it is held in position only by the planets meshing. Any misalignment motion of the planet gears also affects the position of the sun gear axially and radially. To accommodate this motion, the sun gear is connected to the generator by means of a torque tube that is compliant in the axial and radial (but not torsional) directions. The connection between the sun gear and torque tube is a sliding spline joint, which also allows each to move axially relative to the other. One of the goals of the test campaign was to characterize the operation of the planetary section of the drivetrain. Results from these characterizations enable evaluation of the effectiveness of the design techniques. The objectives are defined in Table 2.

Table 2. Gearbox Characterization Test Objectives

Objective	Measurement
Evaluate torque load share among planet gears	Planet bearing loads, ring gear tooth strain, and generator torque as functions of rotor torque and speed
Evaluate dynamic planet gear alignment with ring gear apex	Ring gear strain on each helix, displacement of planet and sun gears as functions of rotor torque and speed
Evaluate roller load distribution in planet bearing	Strain measurements in planet bearing as functions of rotor torque and speed
Evaluate torque tube/sun gear spline joint motion	Sun gear and torque tube displacements

1.3.2 Thermal Performance

The drivetrain includes a circulating lubrication system for the mechanical components with an integrated air cooler to remove heat from the oil. A variable flow-rate fluid system provides circulating coolant for the generator stator and rotor. One of the objectives of the test campaign

was to verify that these systems operate as intended, and maintain the system temperatures within the operational limits. Thermal performance test objectives are included in Table 3.

Table 3. Thermal Performance Test Objectives

Objective	Measurement
Evaluate gearbox fluid cooling system	Planet bearing, main bearing race, main bearing fluid, gearbox fluid inlet and return temperatures
Evaluate generator stator fluid cooling system	Selected stator coil temperatures, coolant inlet and outlet temperatures
Evaluate generator rotor air/water cooling system	Rotor magnet temperatures

1.3.3 Efficiency Tests

The overall goal of the study was to identify and demonstrate a drivetrain with improved cost of energy. An important objective therefore was quantifying the efficiency of the individual components and of the drivetrain system as a whole. Efficiency was measured at several points along the design torque-speed curve. Efficiency test objectives are included in Table 4.

Table 4. Efficiency Test Objectives

Objective	Measurement
Quantify mechanical efficiency	Coolant flow rates and temperature differentials; torque and speeds
Quantify generator efficiency	Generator torque and speed; output current and voltage

Efficiency is estimated using two distinct methods, the input-output method and the calorimetric method, as described below.

1.3.3.1 Input-Output Method

This method is defined in IEEE 115-1995, section 4.6.2, for motors and generators and also is applicable to the gearbox and power electronics unit. The subsystem input power and the output power are measured, then efficiency is calculated as the ratio of the output power to the input power.

$$\text{Efficiency (\%)} = 100 \cdot (\text{output power}) / (\text{input power})$$

For the gearbox, both the input and output power are calculated from the product of the main shaft and generator rotor shaft torques and speeds. For the generator, input power is calculated from the product of the generator rotor shaft torque and speed. The output power is calculated from the sum of the products of the four quadrant voltages and currents.

1.3.3.2 Calorimetric Method

This method is described in IEEE 115-1995, section 4.5 (available at http://standards.ieee.org/findstds/standard/115-1995.html). The output power and the calorimetric (heat) losses are measured. Power is calculated in same manner as for the input-output method.

Efficiency is calculated using the equation below.

$$\text{Efficiency (\%)} = 100 - (\text{losses} \cdot 100) / (\text{output power} + \text{losses})$$

The losses are defined as follows.

$$\text{Loss (kW)} = 0.264 \cdot c_{pc} \cdot G_c \cdot Q_c \cdot (t_{hc} - t_{cc})$$

- c_{pc}—The specific heat of the coolant (relative to water) at average temperature t_{hc} and t_{cc}
- G_c—The specific gravity of the coolant (relative to water) at average temperature t_{hc} and t_{cc}
- t_{hc}—The outlet coolant temperature (˚C)
- t_{cc}—The inlet coolant temperature (˚C)
- Q_c—The rate of coolant flow in gallons per minute

Both the generator and gearbox have distinct fluid systems, but these components essentially are housed in the same steel structure. Undefined thermal short-circuits in the housing structure, however, make it impossible to assign all of the heat energy absorbed by a particular fluid system to the losses associated with that device. The error associated with this "cross-talk" is difficult to estimate. The efficiency calculation for the generator/gearbox assembly is more accurate than the calculations used for each component. The calorimetric tests require that the heat transfer rates reach steady state. This was achieved by operating the test articles until the rates of change of the fluid temperatures and the structure or heat-sink temperature fall below an established value.

The drivetrain installation includes specific instrumentation at several locations to support efficiency measurements, including:

- Main shaft torque and speed;
- Generator torque and speed;
- Generator output current and voltage;
- Inverter output current and voltage;
- Lube system flow rate and temperatures; and
- Generator coolant flow rate and temperatures.

1.3.4 Vibration and Acoustic Noise Levels

The test plan calls for vibration and acoustic emission measurements of the gearbox/generator assembly to be made at selected points on the design torque-speed curve. The ambient noise of the DTF during testing (e.g., dynamometer, ventilation fans, lubrication pump), however, makes performing accurate sound-pressure levels difficult. Although some experimentation was performed with acoustic noise–level measurements, the acoustic emissions of the drivetrain were not evaluated. Vibration measurements are described in ANSI/AGMA 6000-B96 (available from ANSI at http://webstore.ansi.org/RecordDetail.aspx?sku=ANSI/AGMA%206000-B96%20(R2002)). Table 5 lists the vibration test objectives. Instrumentation for measuring vibration includes accelerometers mounted on the gearbox to measure longitudinal, lateral, and vertical acceleration.

Table 5. Vibration Test Objectives

Objective	Measurement
Evaluate drivetrain vibration levels	Linear acceleration

2 Test Article Installation

2.1 Test Article Arrangement

The test setup is shown in Figure 4. The drivetrain assembly, consisting of a single-stage gearbox integrated with a medium-speed permanent magnet generator, is driven by the dynamometer drive system. Each of the four three-phase windings of the generator is connected directly to a passive rectifier (three-phase diode bridge). Each rectifier output feeds one IGBT-based inverter bridge. The direct current (DC) link operates at a variable voltage which is dependent on generator speed. Generator current—and hence torque—is controlled by setting an alternating current (AC) output current to each inverter bridge. The inverters have been designed to operate at unity power factor only. Two 900 kVA output transformers provide voltage-matching between the 480 VAC inverter output and the 575 VAC utility source at the DTF.

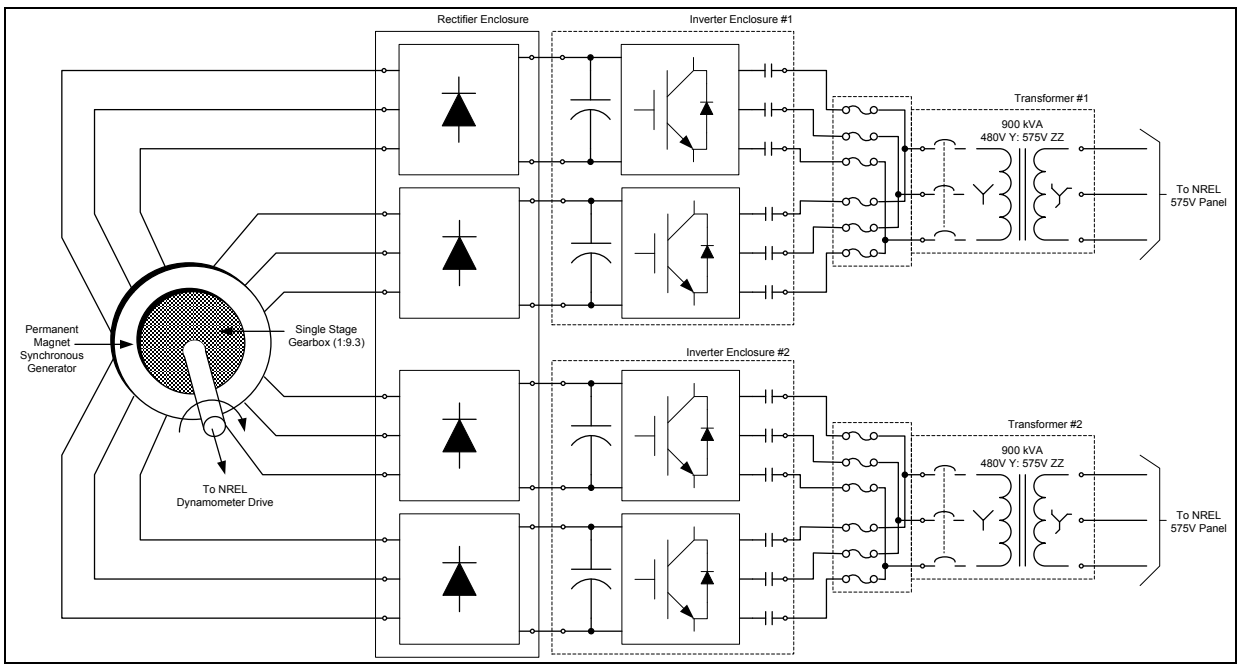

Figure 4. Drivetrain test setup

2.2 Test Articles

The articles tested are listed below and shown in Figure 5. Only one of each article was tested.

- Drivetrain assembly, consisting of a single-stage planetary gearbox (ratio 9.3: 1) and a 1,500-kW, 191-rpm, 690-volt permanent magnet generator, assembled on a test stand.
- Power electronic converter, consisting of a single rectifier cabinet containing four three-phase diode bridges, and two identical inverter cabinets, each containing two independently controlled voltage-source inverter bridges.

The manufacturer and reference specification or drawing number for each component is listed in Table 6. Dimensions and weights for all components are listed in Table 7.

Table 6. Test Article Component Manufacturer and References

Component	Manufacturer	Specification or Reference
Drivetrain assembly	Brad Foote Gear Works; DRS Electric Power Technologies	Mechanical: Powertrain Engineers, Inc. (PEI) dwg. 0202-10100-80; Generator: DNV specification N60004 Rev B
Test stand	Lindquist Manufacturing Corp.	Powertrain Engineers, Inc. dwg. DNV-0202-10205 Rev 6
Power electronic converter	Xantrex Technology, Inc.	Xantrex Schematic Drawing #151858
900-kVA transformers	Mag-Tran Equipment Corp.	DNV specification N60009

Table 7. Component Dimensions and Weights

Component	Length m (ft) -	Width m (ft) -	Height m (ft)	Weight kg (lb)
Gearbox/generator assembly	2.5 (8.2)	2.0 (6.5)	2.0 (6.5)	24,600 (54,120) *
Test stand	2.0 (6.6)	3.5 (11.5)	1.0 (2.2)	5,800 (12,760)
Rectifier cabinet	1.0 (3.1)	0.7 (2.3)	2.5 (7.7)	410 (900)
Inverter cabinet (each)	1.4 (4.3)	0.7 (2.3)	2.5 (7.7)	1,500 (3,300)
900-kVA transformers	2.4 (8)	2.1 (7)	3.0 (10)	5,910 (13,000)
* Note that gearbox section weighs 13,100 KG (28,820 lb); generator section weighs 11,500 kg (25,300 lb) ().				

Figure 5. Gearbox (left); generator assembly power electronic converter (right) (Photo credit: Chris Walford, DNV Renewables Inc.)

2.3 Test Facility

The tests were performed at the NREL 2.5-MW Dynamometer Test Facility located at the NWTC in Boulder, Colorado. The DTF is capable of driving the test article either at a defined fixed rotational speed, or at a nominal rotational speed with a superposed sinusoidal variation. The DTF includes a digital data-acquisition system, the "Dyno DAS." This system was used for short-term measurements of mechanical and electrical parameters at sample rates in the 1-kHz to

2-kHz range. Measurement of slowly varying parameters such as temperature, flow, and pressure were recorded by the DNV drivetrain supervisory controller (DTSC).

2.4 Test Article Drawings

The general arrangement, installation, and interconnections of the test articles are defined in the drawings listed in Table 8.

Table 8. Test System Drawing List

Drawing #	Title	Owner
B-N6-10054	General Arrangement	DNV
B-N6-10051	Sensor and Control Installation	DNV
B-N6-10052	Electrical Schematic	DNV
0202-10227-80	DNV Load Test Layout	PEI
0202-10100-80	Medium-Speed Turbine Assembly	PEI
No number assigned	Test System Wiring Diagram	BEW

3 Test Instrumentation and Data Acquisition

3.1 Instrumentation

To meet the objectives of the test plan, instrumentation was installed on the drivetrain to measure a variety of parameters including voltage, current, displacements, mechanical load, temperature, and vibration.

3.1.1 Electrical System

The generator, rectifiers, and inverters were instrumented with current and voltage transducers to measure current and voltage levels, power flow, power factor, and frequency content. The electrical instrumentation included the following.

- High-bandwidth current transducers on all phases from each generator quadrant
- High-bandwidth line-to-neutral voltage transducers on all phases from each generator quadrant
- High-bandwidth voltage transducers on output terminals of the rectifier bridge connected to each generator quadrant
- Power transducers on the output terminals of each inverter
- High-resolution position transducer on the generator rotor

3.1.2 Motion and Mechanical Loads

In addition to the torque transducer integrated into the DTF drive line, purpose-built instrumentation was incorporated into the drivetrain to measure the torque and speed of the main shaft and generator. Displacements and strain were measured with the following instrumentation.

- Four proximity probes at equal quadrants on one of the carrier pins to measure the axial displacement of the planet gear relative to the carrier pin (PGD1 through PGD4).
- Two strain-gauged slots in the inner race of one of the planet bearings to measure the strain as the loaded roller passes over them (PBL1 through PBL8).

- One proximity probe measuring radial displacement of the torque tube (TTR) and another measuring axial displacement of the torque tube (TTA), relative to the gearbox case.
- One proximity probe measuring axial displacement of the sun gear (SGA) relative to the gearbox case.
- Three pairs of strain-gage bridges measuring root strain along adjacent left-helix and right-helix teeth in the ring gear. These are relative measurements and are not calibrated to a particular load.
- A torsional strain gage in the torque tube to measure generator rotor torque (GRT) (high-speed torque). This has been laboratory calibrated to the torque load.

3.1.3 Thermal

Instrumentation was installed on the drivetrain to measure the generator winding, drivetrain case, and fluid temperatures. Thermal imaging also was used for measuring temperatures during and after particular test runs.

3.1.3.1 Generator Winding Temperature

To monitor the winding temperatures and flow of heat from the stator windings to the generator coolant, several stator temperatures were measured. This was accomplished through the installation of four sets of resistance temperature detectors (RTDs) on and around the windings at different locations on the stator. Each set of RTDs consists of five RTDs installed at the following positions (*see* Figure 6).

- Outside of the end-turn
- Inside of the end-turn
- Laminate tooth
- Back iron
- Cold plate

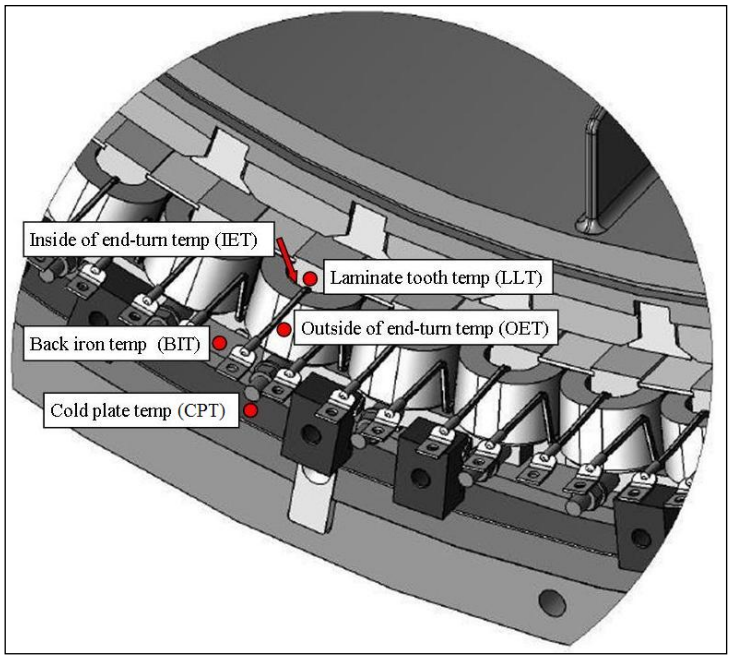

Figure 6. Resistive thermal device locations

Surface-mounted RTDs measured the temperatures at the outside of the end-turn, the inside of the end-turn, the laminate tooth, and the back iron. The cold plate temperatures were measured by embedding RTD probes approximately 1 inch deep into the cold plate.

3.1.3.2 Magnet Temperature

The magnet temperatures were measured directly using infrared thermometry and thermo-couples, and indirectly based on changes in the generator open-circuit voltage. Access ports were installed in the generator cover for directly measuring the rotor magnet temperatures. This required stopping the drivetrain and manually measuring the temperature. There is linear relationship between open-circuit voltage and magnet temperature, therefore the magnet temperatures were estimated by operating the generator open-circuit immediately before or after particular test runs.

3.1.3.3 Drivetrain Case Temperature

The temperature of the drivetrain case was measured using a surface-mount RTD as well as thermal imaging. To measure planet-bearing and main-bearing temperatures, sensors also were embedded in the gear case. To estimate the thermal heat loss of the drivetrain, a heat-flux sensor was installed next to the RTD on the drivetrain case. The heat-flux sensor consists of a thin film that functions as a thermopile transducer. To improve the signal-to-noise ratio, the heat-flux sensor is positioned on one of the hottest portions of the case. A linear relationship is assumed between case temperature and heat flux, which enables the measured heat flux to be scaled with temperature to approximate the average heat flux of the drivetrain.

Thermal images of the drivetrain were used to determine the average temperature of the generator and gearbox to account for thermal variation in the drivetrain case. The thermal images also enable analysis of the heat flow through salient features such as the drivetrain stand.

3.1.3.4 Fluid Temperature and Flow

Temperature sensors were installed in the lubrication and coolant lines to measure supply and return temperatures. Flow and pressure sensors also were installed in the lubrication and coolant systems. The fluid temperature measurements were used to ensure that the drivetrain was operating within acceptable limits. These fluid measurements were combined with the flow measurements to calculate heat loss.

3.1.4 Vibration

The linear vibration of the drivetrain was measured in three orthogonal directions, X, Y, and Z, as shown in Figure 7 (note that Z is coming out of the page). The X direction is defined along the axis of the drivetrain shaft, with X increasing from rotor to generator. The Y direction is defined as perpendicular to the X direction and in the horizontal plane, with Y increasing to the left of the generator when looking into the rotor. The Z direction is defined as perpendicular to the X and Y directions and in the vertical plane, with Z increasing upward.

Two vibration sensors—each consisting of three accelerometers, and capable of measuring vibration in the X, Y, and Z directions—were attached to the exterior of the drivetrain case over the bearings. The vibration sensors were fastened to the casing by gluing on small pads that had threaded holes and then screwing the sensors into the pads.

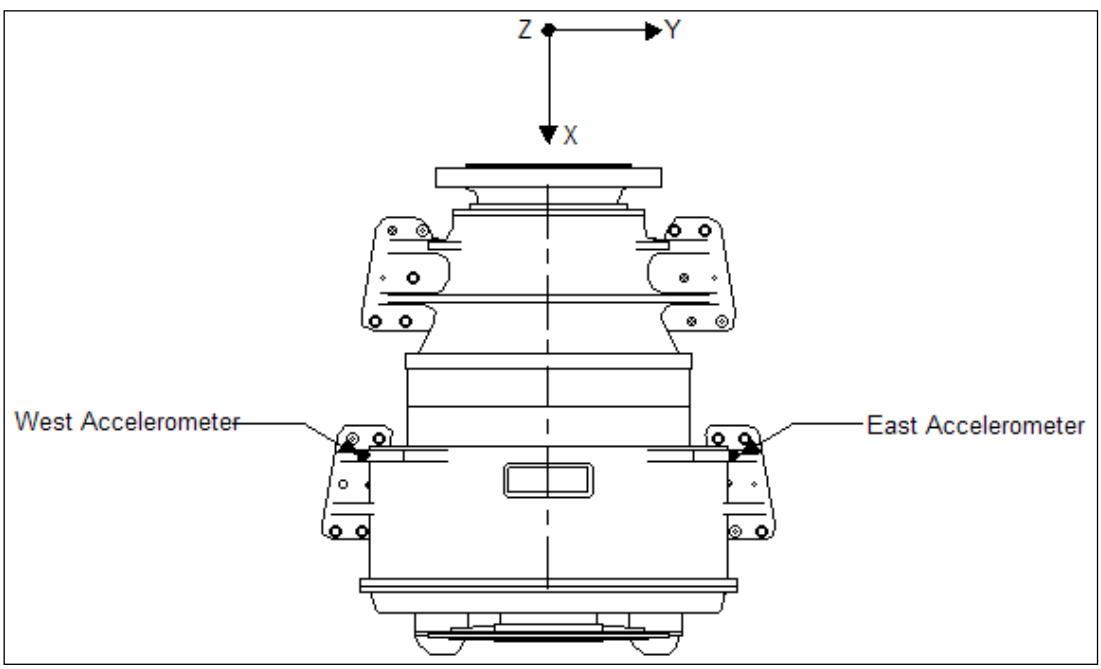

Figure 7. Top view of drivetrain with accelerometer coordinates system and accelerometer locations labeled

3.2 Data-Acquisition Systems

Most of the instrumentation is integrated into the test articles. These signals are accessible to the Dyno DAS at several locations as defined in document B-N6-10051, *Sensor Installation,* and document B-N6-10052, *Electrical Schematic*. Other instrumentation is incorporated into the DTF, or is portable laboratory equipment.

Four measurement systems ran simultaneously during the test:

- Dynamometer Test Supervisory Control;
- Dynamometer Test Facility Supervisory Control and Data Acquisition (SCADA);
- Dynamometer Test Facility Fast Data Acquisition System (FastDAS); and
- Dynamometer Test Facility Vibration Monitoring System (Vibration Monitor).

All four of these systems are based on National Instruments technology and run under the LabVIEW platform. The DataSocket interface was used to port signals between the DTSC, SCADA, and Fast DAS.

The DTSC ran continuously and recorded temperatures, fluid pressures, and flow rates of all of the critical electrical and mechanical components. These signals change relatively slowly, so they were sampled at 1 Hz. The signals were converted to engineering units in real time and displayed on the DTSC operator screen, but were not recorded by the DTSC. Appendix A, Table A-1, lists the sensors connected to the DTSC. The SCADA recorded the signals measured by the DTSC. FastDAS recorded the signals that require a high sampling rate. These were sampled at 2 kHz for short periods (less than one minute) to limit the size of the data files (Appendix A, Table A-2, lists these signals). Refer to drawing B-N6-10052, *Electrical Schematic,* for details on the electrical connections.

The vibration monitor recorded the accelerometer output at 2 kHz. Appendix A, Table A-3, lists the accelerometer signals. A vibration monitor calculates velocity and displacement from the accelerometer data. Some calculated channels also were required for monitoring drivetrain condition and status during the test campaign. These were implemented in "real-time" in the SCADA. These channels are defined in Appendix A, Table A-4. All of these signals were recorded at 2 kHz along with the measured signals. Additional portable or stand-alone instruments were required for some tests, such as for infrared temperature measurements and ongoing fluid-cleanliness checks. These are identified in the description of the particular test procedure.

4 Test Campaign

The DNV WindPACT drivetrain is a prototype system that was commissioned for the first time when it was installed at the DTF. This commissioning process, described in DNV document N60016, *Test System Commissioning Plan,* included installation and alignment to the dynamometer, connecting power and signal wiring, connecting the lubrication and fluid cooling systems, and power-up of the rectifier/inverter system.

During the testing phase, the test article gradually was brought up to rated speed and power in incremental steps. To ensure that the systems were operating as intended, the test article performance was evaluated at each step prior to beginning the next step. This approach ensured that if a problem with the test article developed and testing had to cease for a period, then some test data would be available and analysis could proceed in the interim.

This approach proved to be wise when the generator winding failure occurred after only a brief period of operating at near rated power. This failure was not entirely unanticipated, because similar failures had occurred during the factory test of the original coil design. At that time, the

coils were rewound with a more robust insulation scheme and successfully retested. The risk of an additional failure during the actual test was too great, however, and it was decided that the coils would be reconfigured. The generator rewind required disassembly of the test article in the DTF, shipment of the core assemblies to the rewind facility, and reassembly using the new coils. The entire process halted the test campaign for four months. The test campaign then was restarted as if the unit was a new test article, because the differences in the generator design were significant both electrically and thermally.

Overall, there were five test types; each was given a numeric designation as shown in Table 9. The basic test parameters for each test—speed and power—are listed in Table 10. The number in each test designation describes the type of test, and the letter corresponds to a specific torque-speed operating point. Except for the last test listed in the matrix, all of the tests were steady-state. The test article was brought to a constant speed and then enabled to generate at the target output power level. Note that the power level actually was set by a current command—in amps—to the Xantrex inverters. In practice this command was adjusted by trial-and-error to achieve the target output power level at constant speed. The service voltage at the DTF fluctuated during testing but generally was low. The power converter of the test article is current limited, therefore reduced service voltage reduces the allowable output power. The Stage 1 tests (levels a through c) shown in Table 10 are shaded grey because it was not possible to reach the target output power level due to insufficient bus voltage.

Table 9. Test Type Designations

Type	Title
1	Open-circuit DC voltage characterization (cold)
2	Power curve operation
3	Open-circuit DC voltage characterization (hot)
4	Efficiency
5	Vibration and acoustical

Table 10. Test Matrix

Stage	Main Shaft Speed (rpm)	Genera-tor Shaft Speed (rpm)	Drivetrain Output Power (kW)	Open-Circuit Cold Test#	Power Curve Test #	Open-Circuit Hot Test #	Efficiency Test #	Vibration & Acoustical Test #
				Series 1	Series 2	Series 3	Series 4	Series 5
1	12.2	114	233	1a	—	—	—	—
	12.4	116	301	1b	—	—	—	—
	13.4	124	378	1c	—	—	—	—
2	14.3	133	467	1d	2d	-	4d	5d
	15.4	142	568	1f	2f	3f	—	—
3	16.2	151	682	1g	2g	—	4g	5g
	17.2	161	811	1h	2h	—	—	—
	18.1	170	952	1j	2j	3j	4j	5j
4	19.1	178	1,110	1k	2k	3k	—	—
	20.1	187	1,284	1m	2m	3m	4m	5m
	20.5	191	1,460	1n	2n	3n	4n	5n
	20.5	191	1,500	1p	2p	3p	4p	5p
	—	Ramp 0 to 191 @ 10 rpm per second	0	—	—	—	—	5r

5 Test Results

5.1 Component Characterization

During all drivetrain testing the dynamometer was operated using speed control. Using this function, the desired speed is specified in the dynamometer controller and the torque applied by the dynamometer is adjusted to maintain the desired speed. The output of the inverters connected to the generator was controlled by specifying the desired output current in the inverter controller. For a given current command, the output power of the inverters fluctuated based on changes in the grid voltage. The generator power was determined by setting the desired speed in the dynamometer and the desired current in the inverters. The current command values for the inverter current that correspond with the operating points in the test matrix were determined empirically. During the commissioning of the drivetrain, the inverter current set points were determined by operating the generator at each speed in the test matrix and adjusting the inverter current until the output power matched the value stipulated in the test matrix.

5.1.1 Generator Characterization

5.1.1.1 Electromotive Force Voltage Constant

The open-circuit voltage of the generator, with both the original parallel windings and the reworked series windings, was slightly greater than expected. Figure 8 is a plot of the generator open-circuit voltage. It was not possible to operate the generator open-circuit faster than 169 rpm due to protective voltage limits in the power electronics. The parallel windings generated an open-circuit voltage that was 3.5% greater than that specified in the design, and the series windings generated an open-circuit voltage that was 4.4% greater than specified in the design.

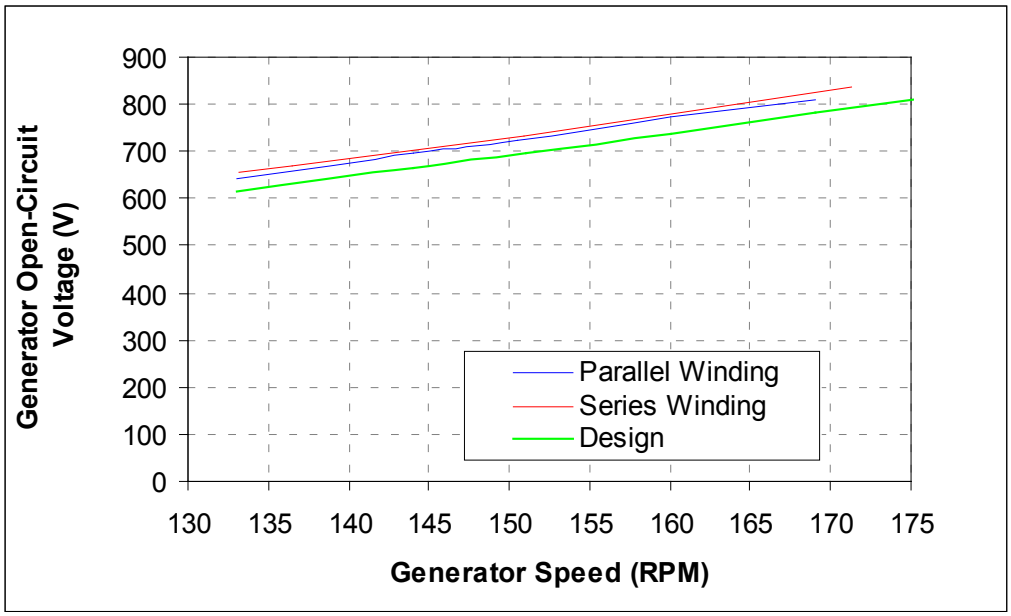

Figure 8. Generator open-circuit voltage

The DC-link voltage is measured at the output of the rectifier. Figure 9 is a plot of the DC-link open-circuit voltage of the power electronics as a function of the generator speed. The series and parallel winding configurations produced similar open-circuit voltages in the DC-link.

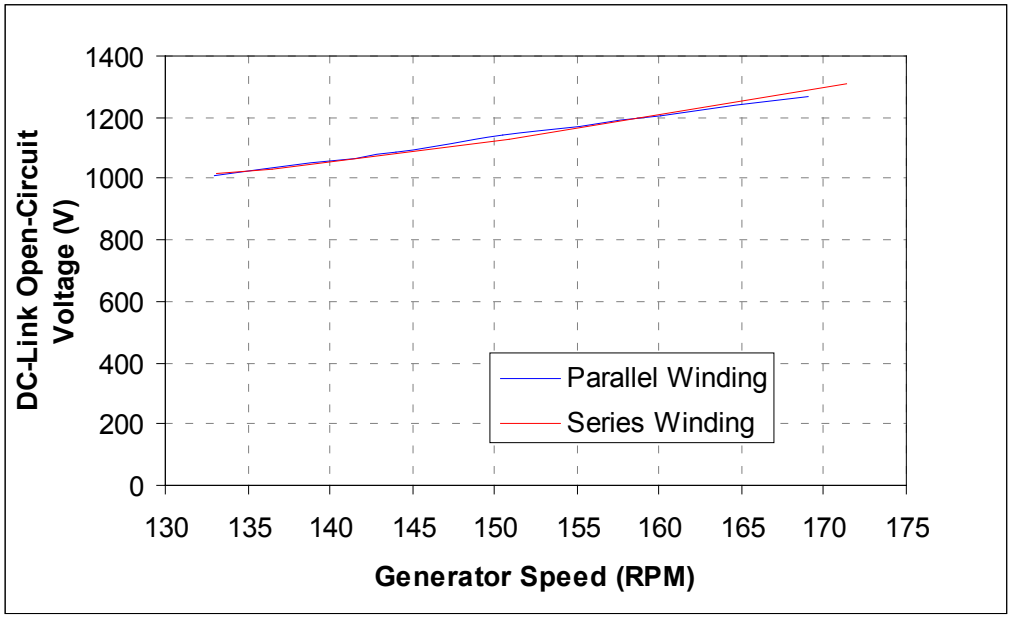

Figure 9. DC-link open-circuit voltage

Figure 10 is a plot of the design and measured generator current as a function of rotor torque. All references to current in this document refer to the total generator current, which is calculated by summing the average current of each quadrant. At low torque levels the measured current is relatively close to the design values. At greater torque values, however, the measured generator current is significantly greater than that specified in the design.

The test matrix in Table 10 defines the operating envelope of the drivetrain. In this test matrix, increased power is achieved by simultaneously increasing torque and speed. Consequently, all plots of torque also have varying speed, and all plots of speed also have varying torque. Speed was not held constant for the measurements in Figure 10, and torque was not held constant for the measurements in Figure 11.

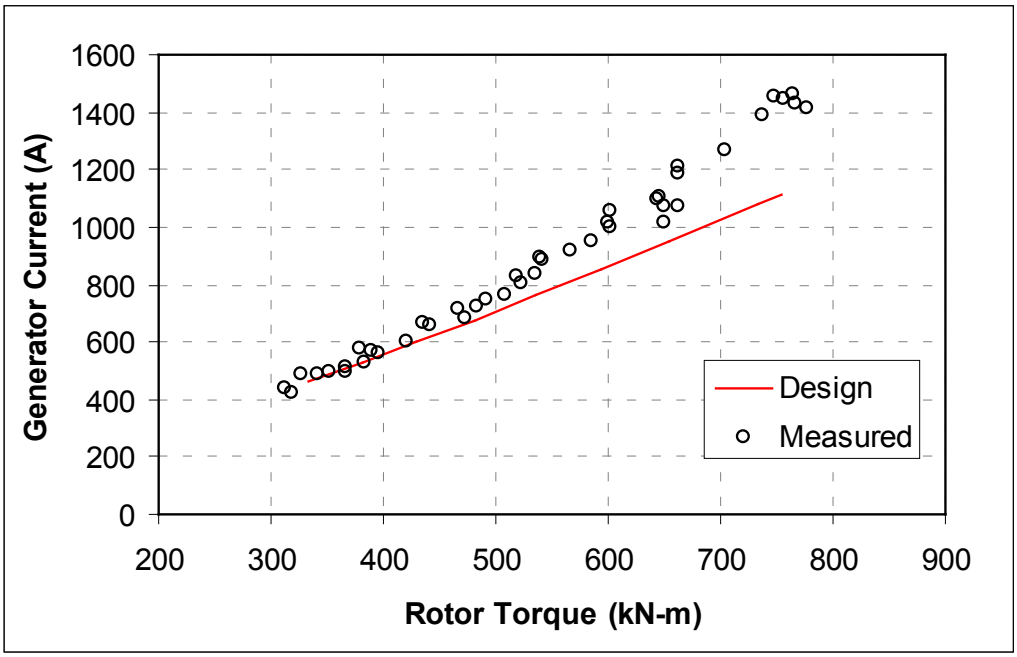

Figure 10. Generator current versus rotor torque

Figure 11 is a plot of the measured and design generator voltage as a function of main shaft speed. The measured generator voltage is near the design value at low speeds but drops to less than the design value at greater speeds. The discrepancy between the two voltage values propagates to the DC-link voltage, as shown in Figure 12. The voltage data in Figure 11 and Figure 12 has a large amount of scatter, indicating that the generator voltage is being influenced by a factor other than generator speed.

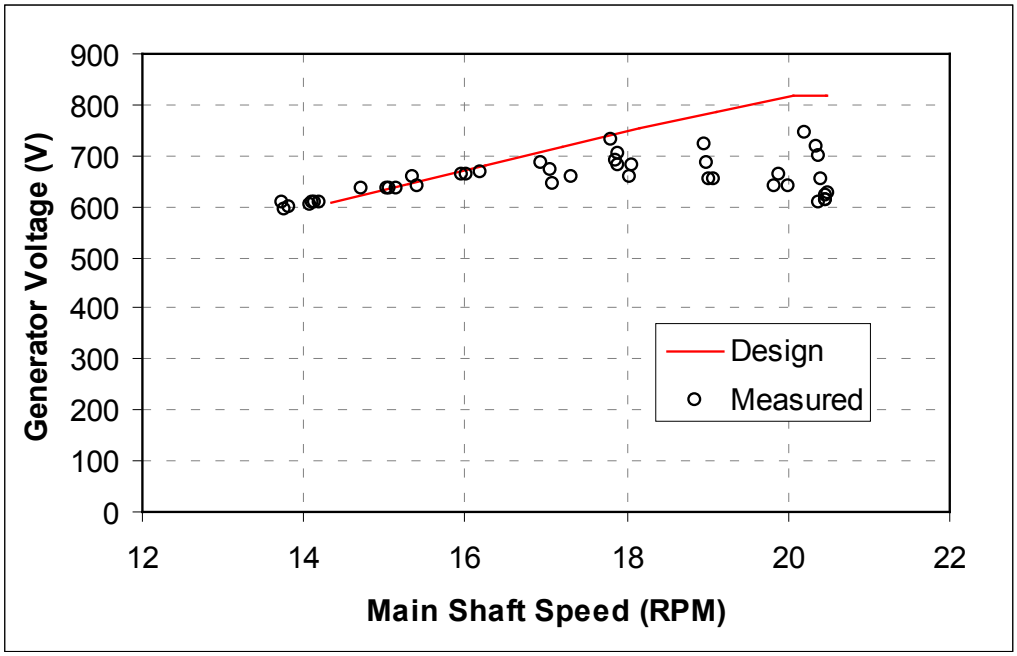

Figure 11. Generator voltage versus main shaft speed

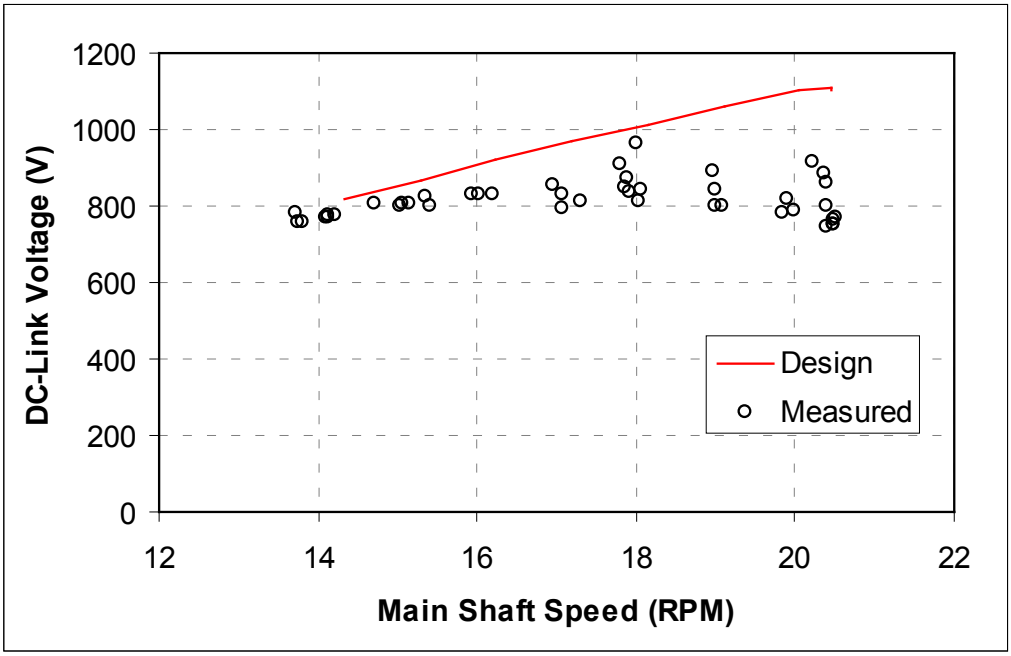

Figure 12. DC-link voltage versus main shaft speed

Although there are correlations between current and torque and between voltage and speed, the plots of current and voltage provided above could be misinterpreted because speed is not held constant during period shown in the torque plots and torque is not held constant in the speed plots provided. The generator current and voltage are plotted against generator power in Figure 13 and Figure 14. Measured results are presented for the original parallel winding configuration and for the reworked series winding configuration. The measured generator current and voltage for both winding configurations is consistent with the design values at low power levels but diverges at greater power levels. There is scatter in the current data—despite the tight regulation of the inverters—because variations in voltage affect the power of the generator. The scatter in generator voltage data increases dramatically as the power level increases. Some of the discrepancy between the measured and design values of current and voltage and the scatter of the voltage data can be explained by taking into account the power factor and thermal effects.

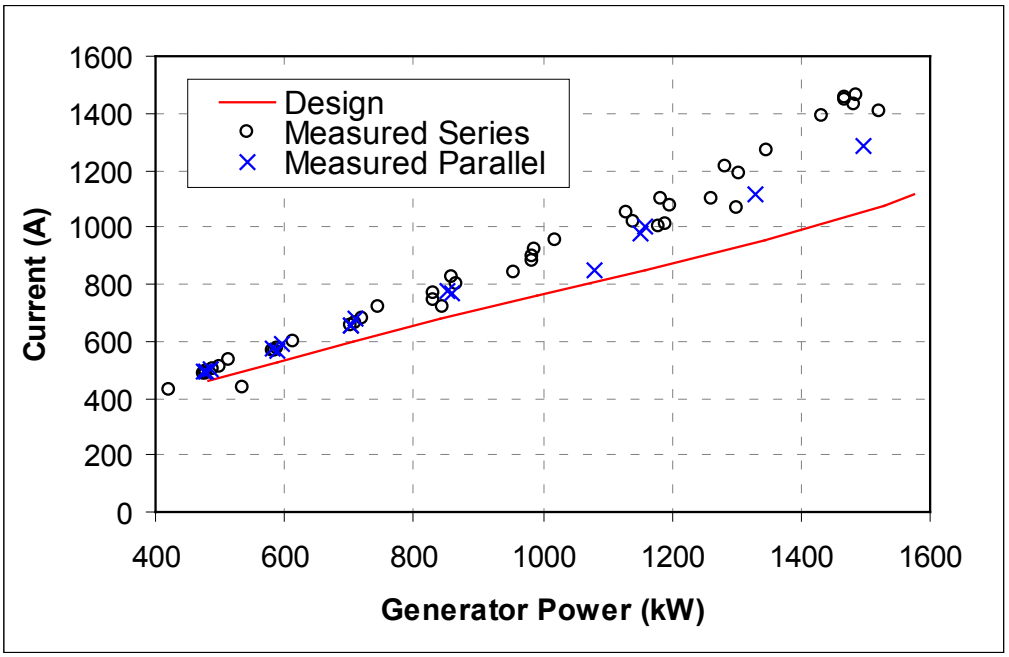

Figure 13. Generator current versus generator power

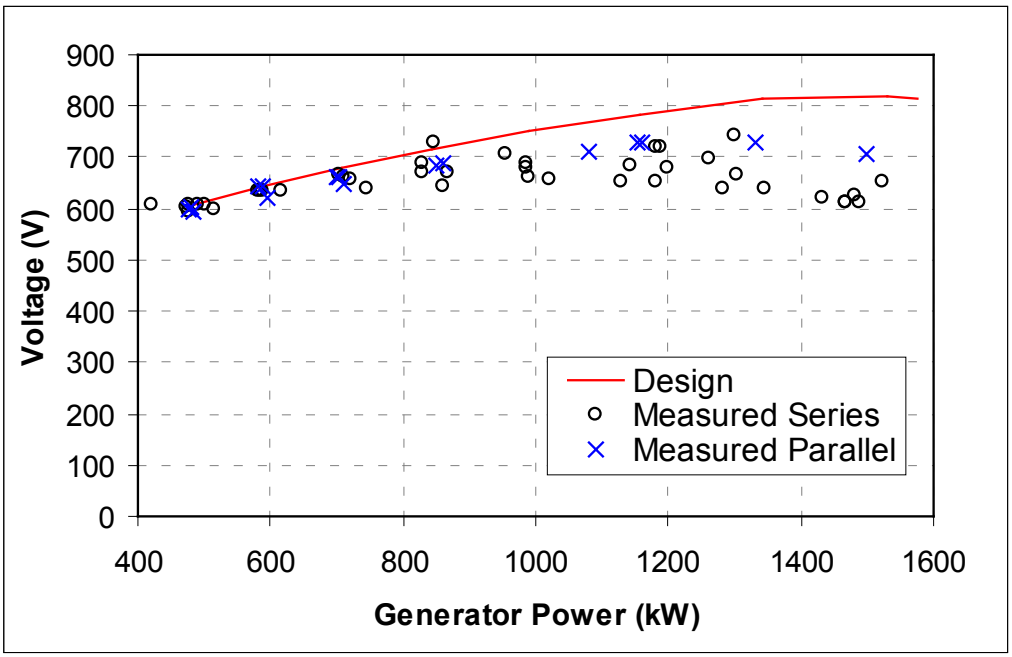

Figure 14. Generator voltage versus generator power

Figure 15 is a plot of the generator power factor. This factor ranges from 0.93 to 0.96, which is consistent with the theoretical power factor of a passive rectifier. The design assumed that the generator would operate at unity power factor. Operation at a power factor of 0.93 to 0.96 results in 4% to 7% more current than operation at unity power factor. The lagging power factor of the generator accounts for some of the discrepancy between the design and measured current in Figure 13. The lagging power factor, however, does not explain why the measured generator

current diverges from the design current as the power level increases. There is very little scatter in the data points of Figure 15; power factor is not causing the scatter present in the current and voltage data in Figure 13 and Figure 14.

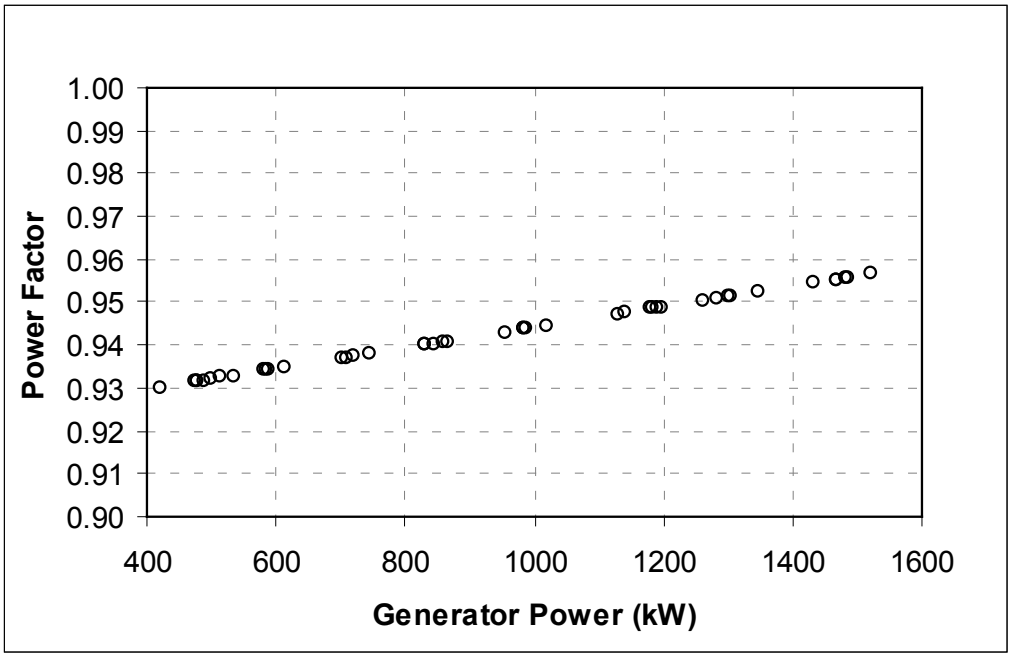

Figure 15. Generator power factor

The theoretical temperature coefficient of the generator electromotive force is -0.11% per degree Celsius. Therefore for every 1°C increase in magnet temperature the open-circuit generator voltage should decrease by 0.11%. Figure 16 provides a plot of the measured and calculated magnet temperature as a function of generator open-circuit voltage. The calculated magnet temperature is based on the theoretical temperature coefficient of the magnets. To measure the magnet temperature, the drivetrain was stopped immediately after an open-circuit test and the temperature was measured through an access port using a temperature probe. This measurement method has inherent inaccuracy due to the great amount of heat radiating from the windings, which are designed to operate at 165°C. The proximity of the magnets to the windings and the lack of convection caused the magnets to heat up after the generator was stopped. Using the open-circuit voltage to estimate the magnet temperature is more accurate than directly measuring the magnet temperature through the access ports. Consequently, the magnet temperatures calculated using the open-circuit voltage in Figure 16 better reflect the actual magnet temperature than do the temperature-probe results.

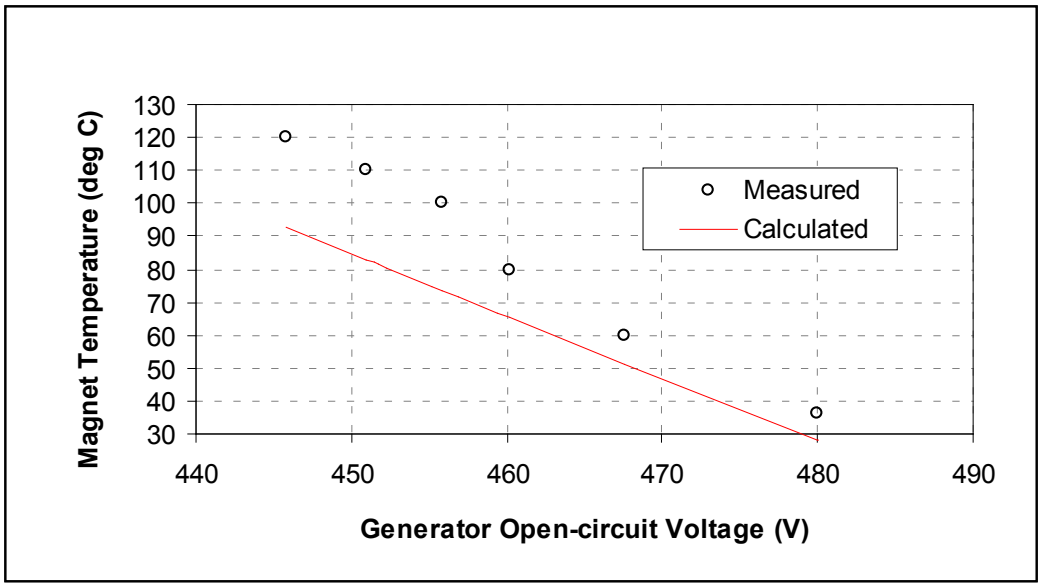

Figure 16. Magnet temperature and generator open-circuit voltage

Figure 17 is time-series plot of the open-circuit generator voltage and stator temperatures. As the stator temperatures increase, the generator voltage decreases. The decrease in generator voltage as temperatures increase is prevalent in all open-circuit and loaded test runs.

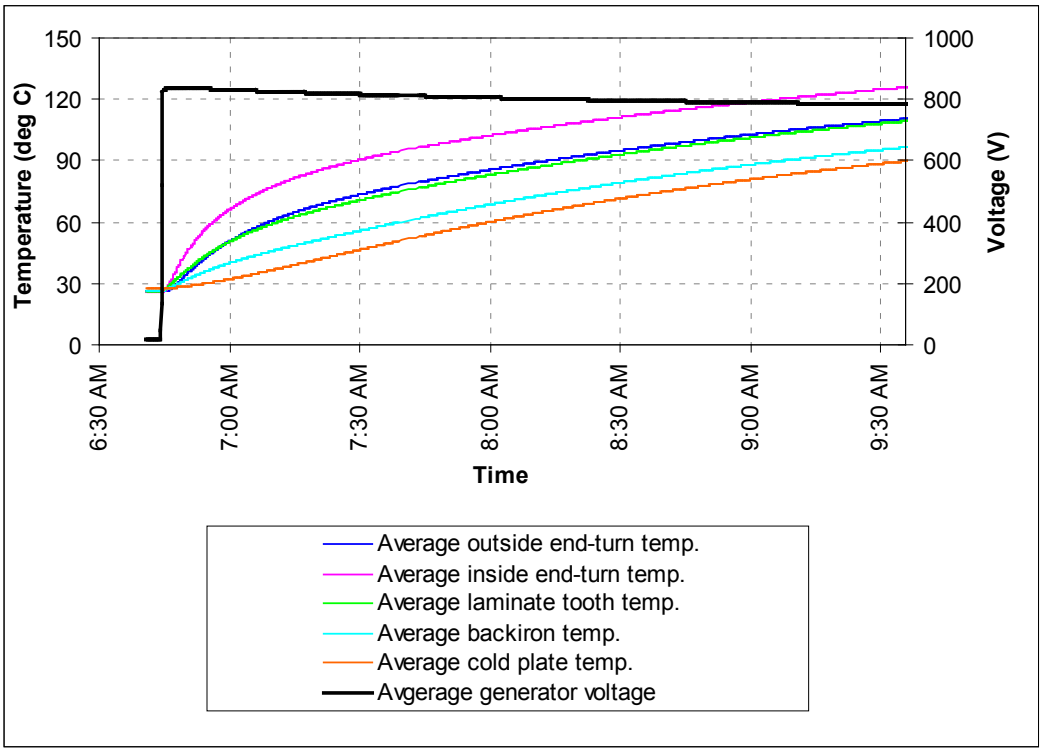

Figure 17. Stator temperatures and open-circuit generator voltage

Figure 18 shows the measured relationship between change in generator open-circuit voltage and change in stator temperature for the test run illustrated in Figure 17. The temperature change is relative to the ambient temperature, and the voltage change is relative to the voltage at the ambient temperature. The generator is operating at no load and without the coolant loop running. It therefore it seems reasonable that the magnet temperatures and stator temperatures would change at approximately the same rate. Based on Figure 18, the empirical temperature coefficient of the generator voltage is -0.11% per degree Celsius. Assuming that the change in temperature of the stator is approximately equal to the change in temperature of the magnets, the theoretical temperature coefficient of the generator voltage is confirmed.

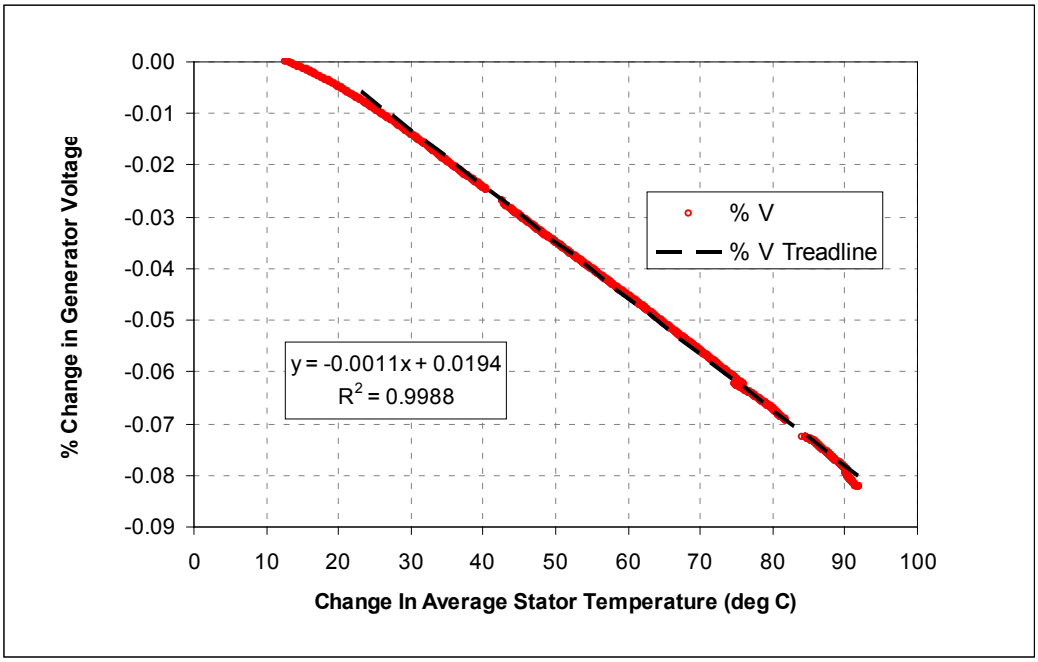

Figure 18. Generator voltage drop with temperature

For a subset of the data points in Figure 13 and Figure 14, the open-circuit voltage of the generator was checked immediately after the operating data was collected. The open-circuit voltage then was used to estimate the reduction in generator voltage caused by increased magnet temperature. The design voltage and current values did not take into account the effect of elevated magnet temperature. Figure 19 and Figure 20 contain the subset of current and voltage data points for which the open-circuit voltage was checked immediately after the test run. Figure 19 and Figure 20 also contain adjusted versions of measured current and voltage values. The measured current and voltage values have been adjusted to compensate for the effects of power factor and temperature.

The adjustment of the voltage and current was performed based on the following set of assumptions.

- The design calculations assumed the generator would operate at unity power factor. During testing, the generator operated at a power factor of 0.93 to 0.96, lagging. This resulted in an increase in current of 4% to 7%.

- The voltage and current design calculations assumed the generator voltage would be independent of temperature. Test data confirmed the theoretical temperature coefficient of the magnets and demonstrated that elevated magnet temperatures can significantly reduce the induced EMF of the generator. The decrease in voltage required the current to be increased to maintain the desired power.
- The elevated current resulting from the lagging power factor and reduced EMF caused increased conduction losses. The increased losses resulted in increased generator temperatures and, consequently, increased magnet temperatures. This caused further reduction in the generator voltage.

The relationship between current, voltage, and magnet temperature forms a positive-feedback system. Adjusting the current and voltage values to account for the lagging power factor and thermal effects decreases the discrepancy between the design and measured values; however, there still is some divergence between the design and measured values at greater power levels.

One of the causes of this remaining divergence is that the elevated current levels increase the voltage drop across the impedance of the stator circuit; this results in reduced voltage at the generator terminals. The decreased voltage requires more current to maintain a given power level which, in turn, increases the voltage drop in the stator impedance. Similar to the thermal effects on the magnets, this forms a positive-feedback system which exacerbates the discrepancy between design values and measured values. The increased voltage drop across the stator impedance due to elevated current is estimated to affect the magnitude of the current and voltage by up to 1%.

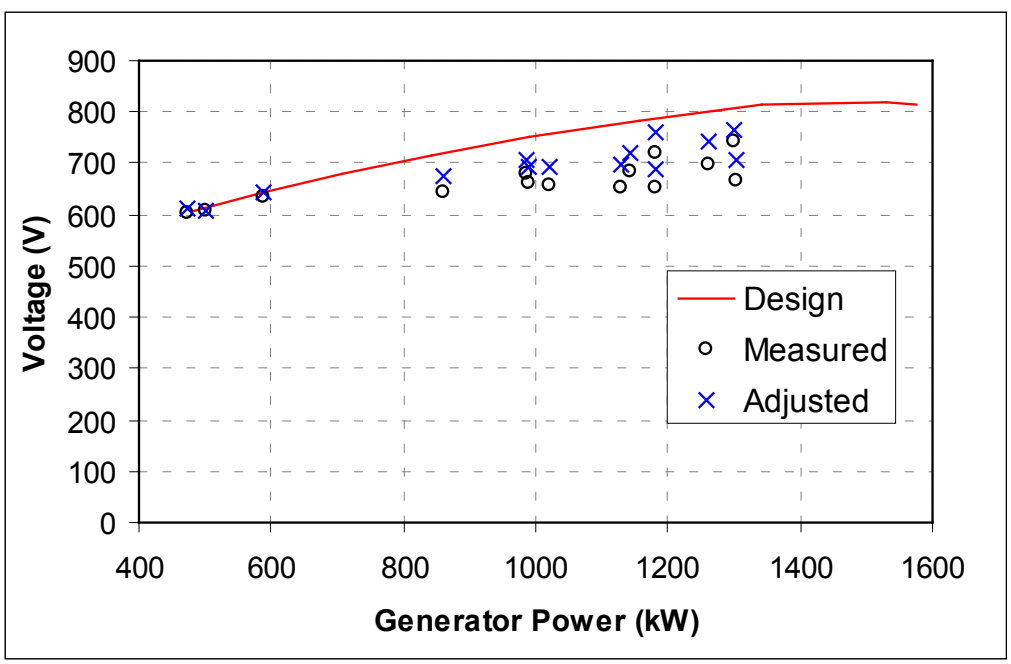

Figure 19. Generator voltage versus generator power

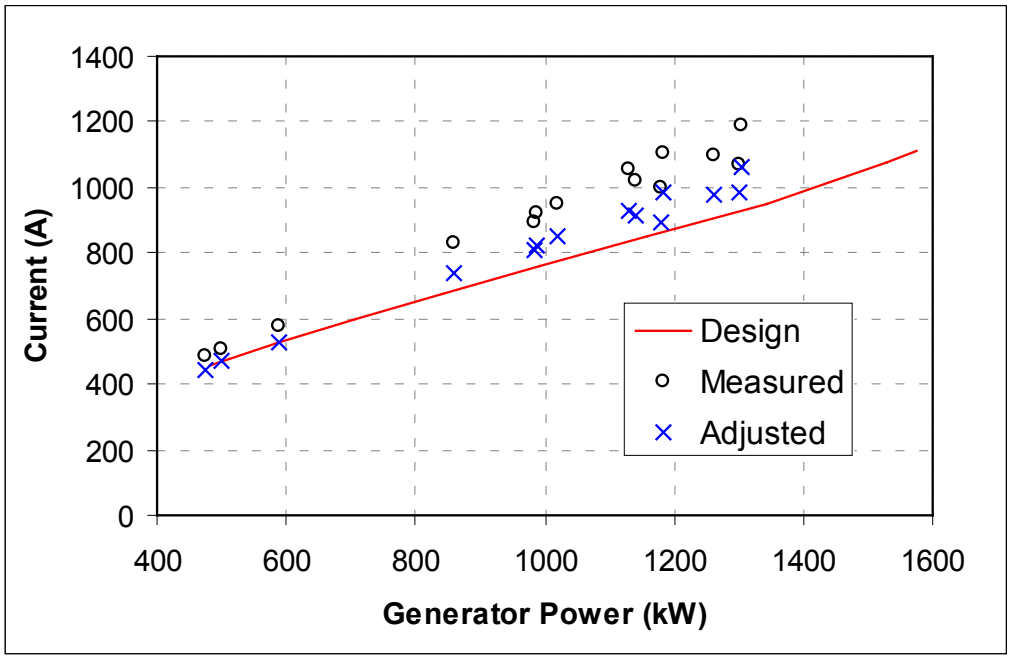

Figure 20. Generator current versus generator power

5.1.1.2 Waveforms

The current waveforms of one quadrant of the generator at one third rated power and rated power are shown in Figure 21 and Figure 22. The nominal rotational speed at one third rated power is 133 rpm and the nominal rotational speed at rated power is 191 rpm, as listed in the test matrix in Table 10. At one third rated power, the prominence of the fifth harmonic is evident in the double hump of the current waveforms. As the power increases, the magnitude of the fifth harmonic—as well as the other higher-order harmonics—decreases and the current waveforms become more sinusoidal.

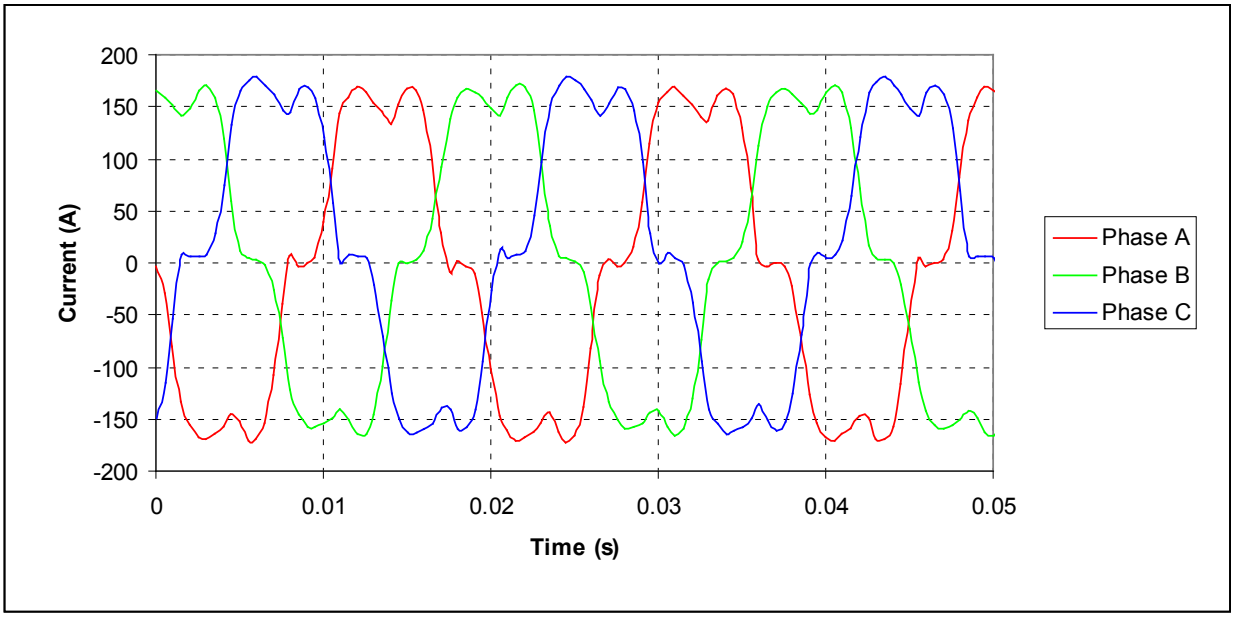

Figure 21. Generator current waveforms at one third rated power

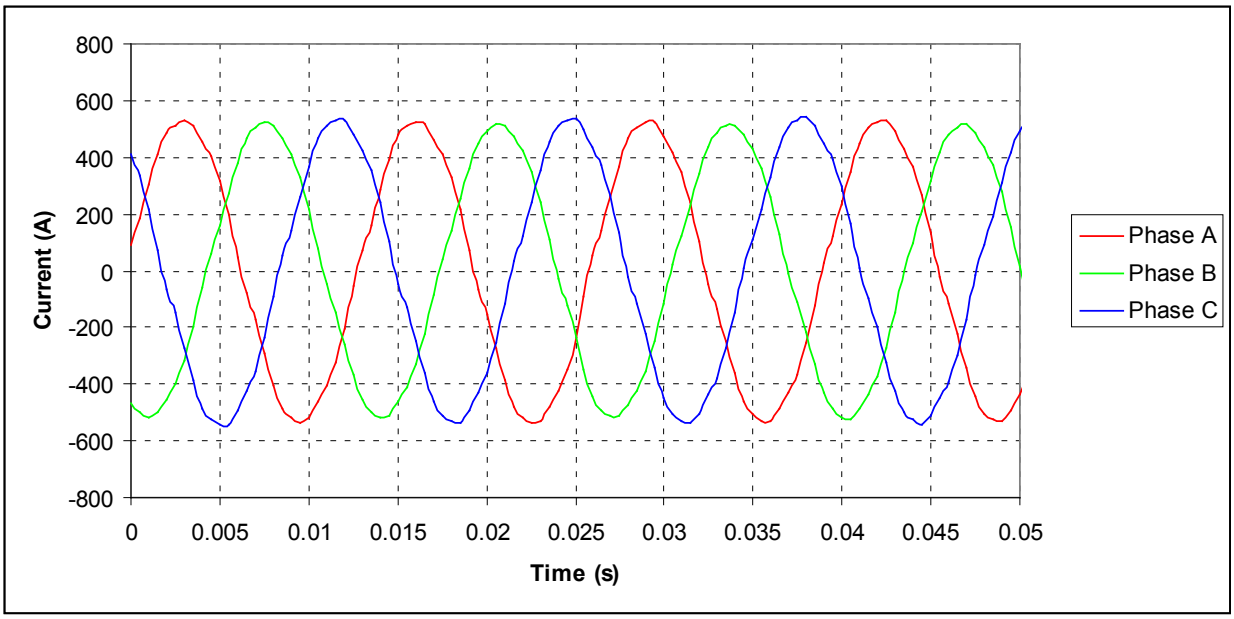

Figure 22. Generator current waveforms at rated power

Although the generator current waveforms become more sinusoidal as the load increases, the voltage waveforms become increasingly distorted as generator power increases. The voltage waveforms at one third rated power and rated power, in Figure 23 and Figure 24, respectively, show large fifth and seventh harmonics. The influence of the higher-order harmonics increases with load.

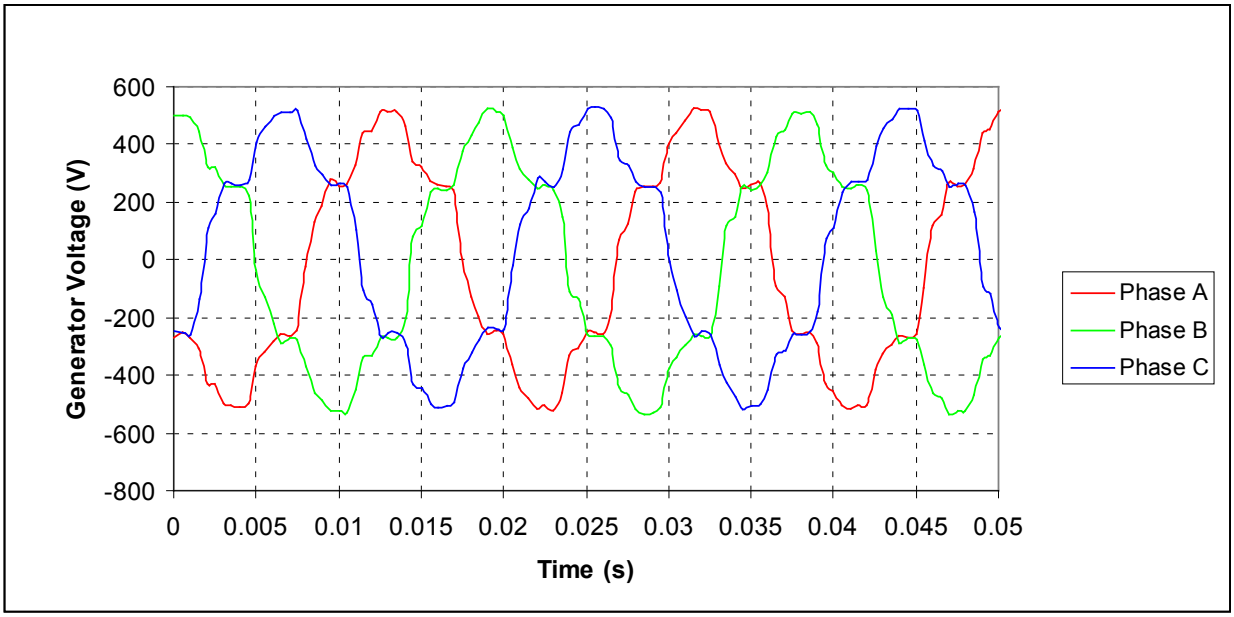

Figure 23. Generator voltage waveforms at one third rated power

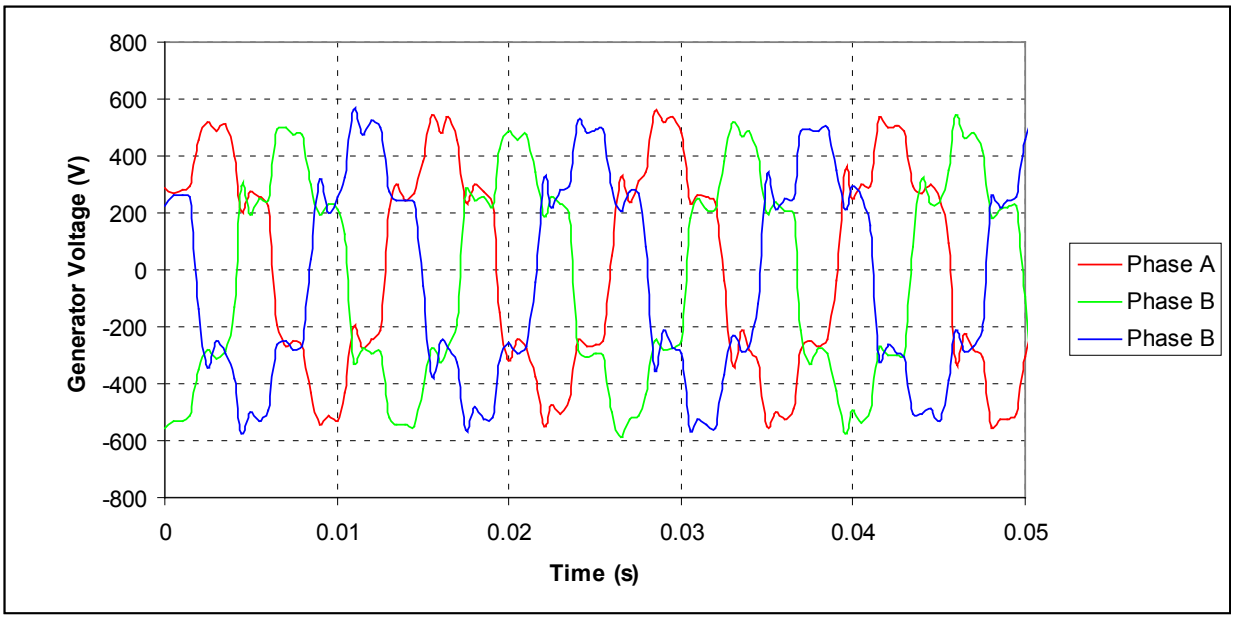

Figure 24. Generator voltage waveforms at rated power

5.1.2 Harmonics

Figure 25, Figure 26, Figure 27, and Figure 28 contain the power spectral density (PSD) of the generator current and voltage at one third rated power and rated power. The frequency axes of these plots are normalized by the fundamental electrical frequency at the generator. For example, one corresponds with the fundamental frequency, two corresponds with the second harmonic, and three corresponds with the third harmonic. The fundamental electrical frequency is 52.5 Hz at one third rated power and 76.0 Hz at rated power. The current PSD shows a significant reduction in the fifth harmonic and moderate reductions in the eleventh and thirteenth harmonics

as the generator power is increased. The voltage PSD shows an increase in the fifth, seventh, eleventh, and thirteenth harmonics.

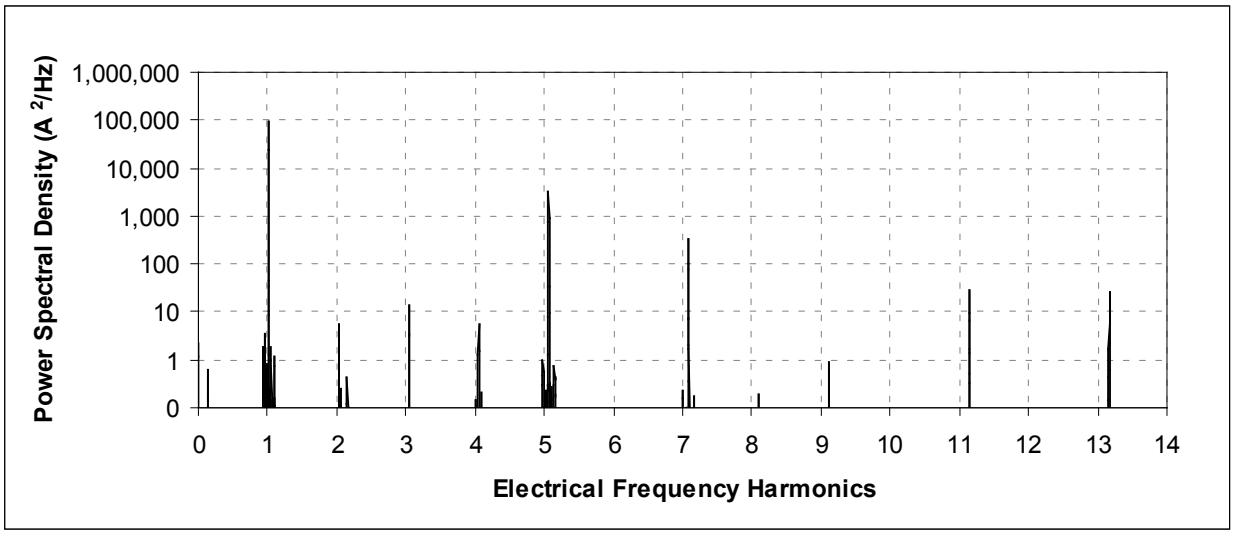

Figure 25. Generator current power spectral density at one third rated power

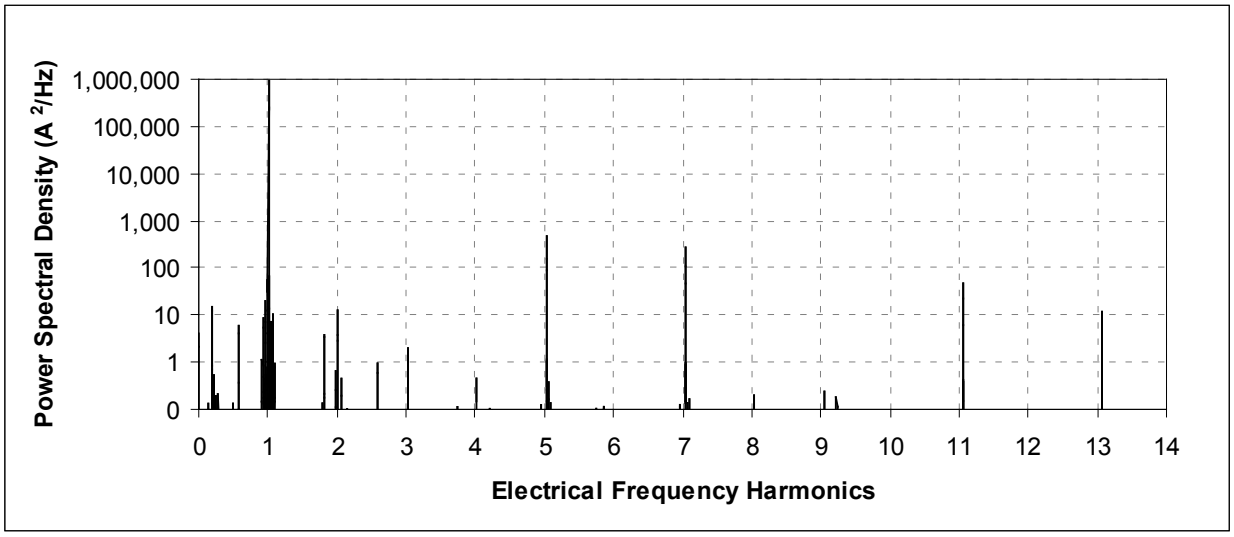

Figure 26. Generator current power spectral density at rated power

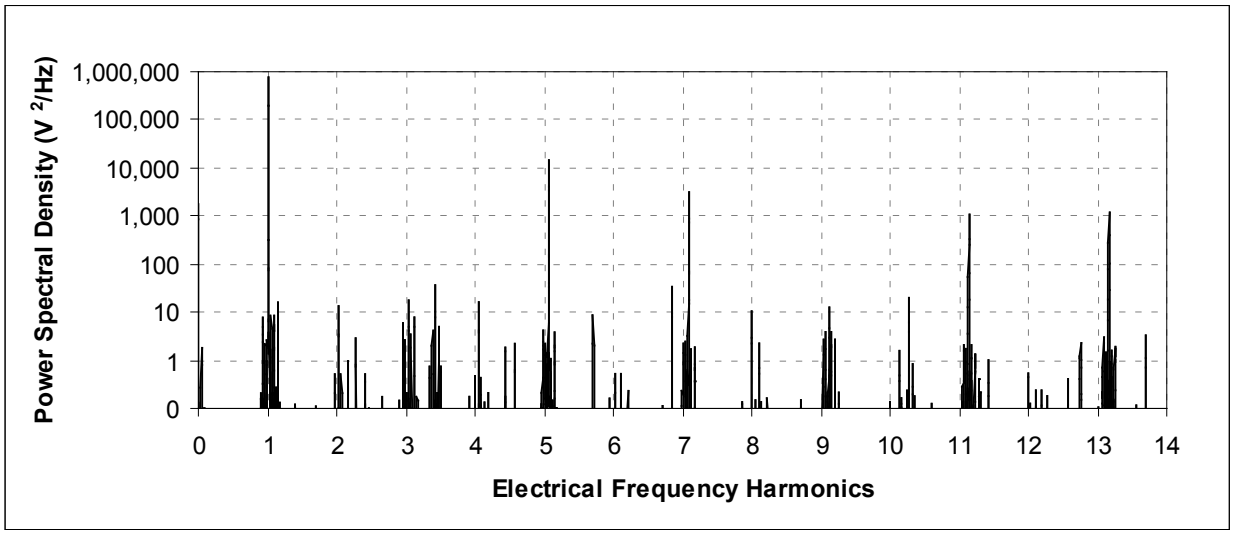

Figure 27. Generator voltage power spectral density at one third rated power

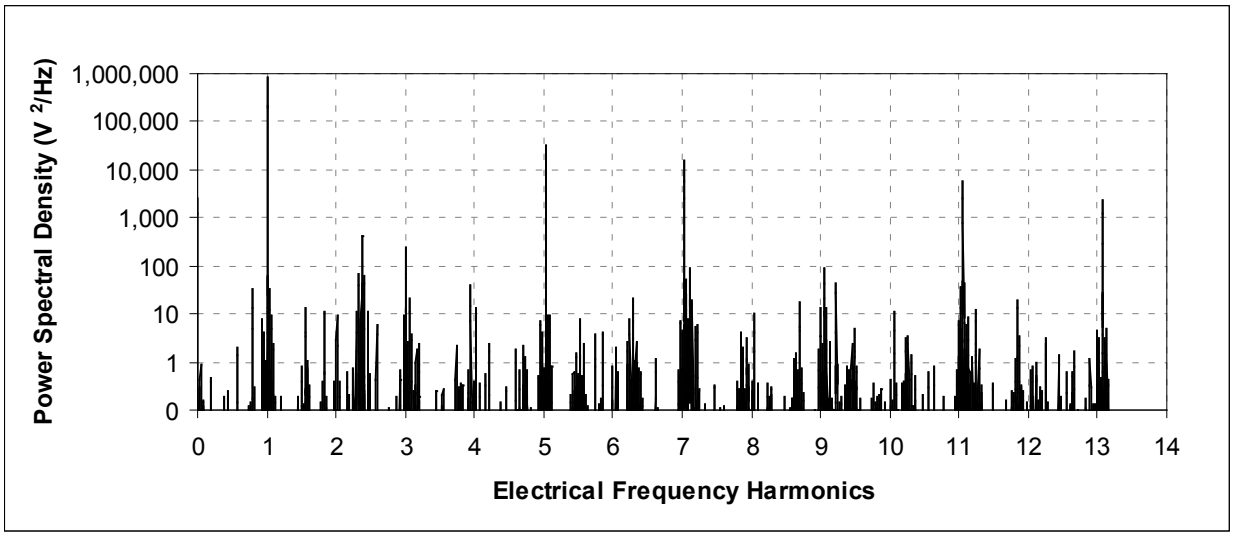

Figure 28. Generator voltage power spectral density at rated power

The total harmonic distortion (THD) of the generator current and voltage is plotted against generator power in Figure 29. The THD and PSD results indicate that increased load smoothes the current waveforms and distorts the voltage waveforms. These results are consistent with expectations for a permanent magnet generator with a passive rectifier.

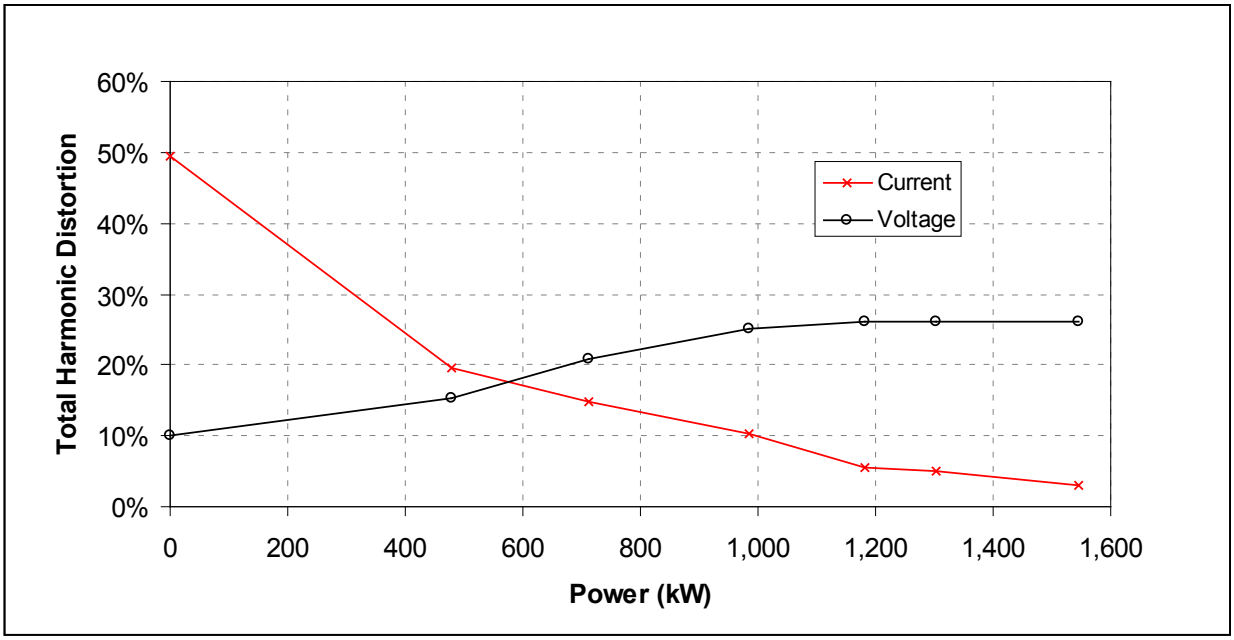

Figure 29. Total harmonic distortion of generator voltage and current

5.1.2.1 Cogging Torque

The magnetic cogging torque of the generator was measured by DRS Electric Power Technologies with the rotor in place and the cover removed, using the test setup shown in Figure 30. The torque measurement arm used a turnbuckle to rotate the rotor and a load cell measured the force at approximately every one eighth of a degree. The rotational position was measured using a scale on the rotor, as shown in Figure 31.

Figure 30. Cogging torque measurement test setup (Photo credit: Terry Lettenmaier, Global Energy Concepts, LLC)

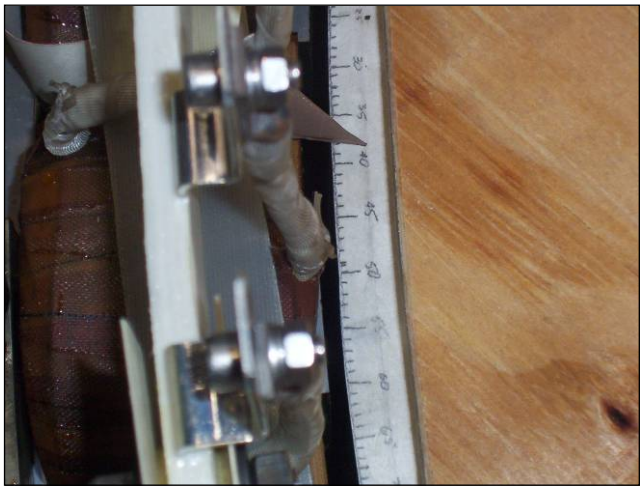

Figure 31. Rotation scale with tics at 2-mm intervals (Photo credit: Terry Lettenmaier, Global Energy Concepts, LLC)

The torque measurement arm was attached to the mounting flange of the generator housing. This allowed the torque measurement arm to apply tangential forces to the rotor. The test setup took advantage of the symmetry of the housing, enabling the measurement arm to be mounted on either side of the housing, and increasing the effective measurement to a 52º mechanical sweep. The torque was measured as the turnbuckle was expanded and contracted, so both clockwise (CW) and counterclockwise (CCW) data are included.

The torque measurements were calibrated to the position of a magnet with respect to the teeth of the stator. The initial position of the rotor was such that every other magnet was in D-axis alignment with every third stator tooth. Figure 32 contains the static cogging torque measurement results. In the Generator Factory Acceptance Test Report, DRS indicated the cogging torque period is 15º.

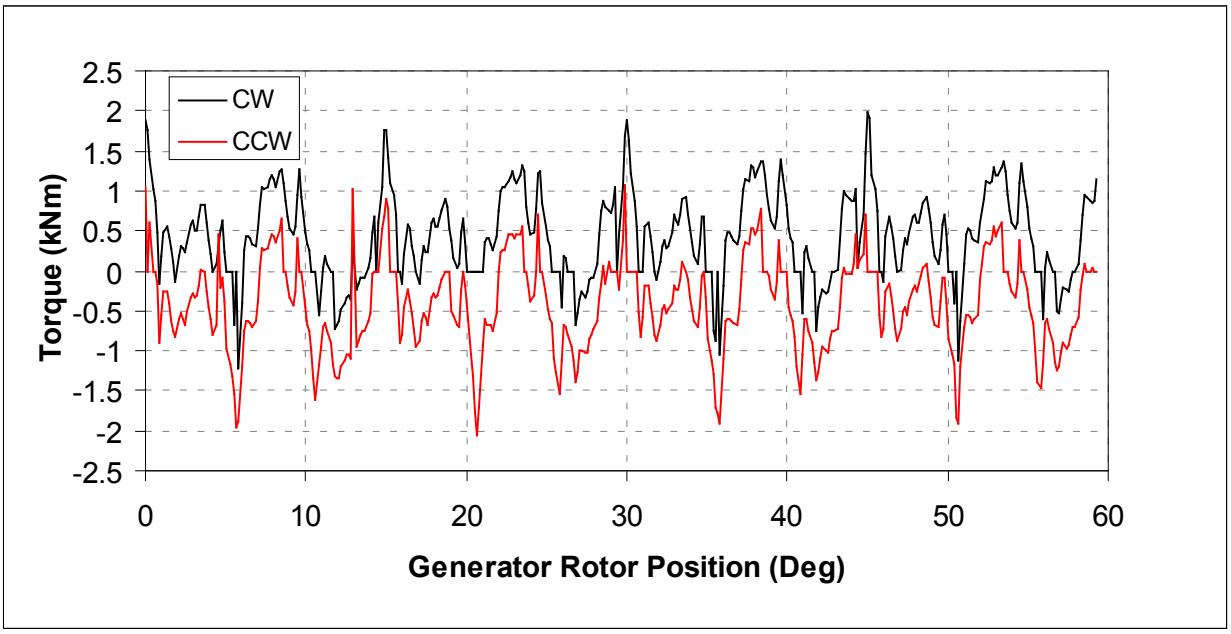

Figure 32. Static cogging torque

Figure 33 contains a frequency domain plot of the generator no-load torque with the generator speed at 133 rpm and at 169 rpm. The cogging torque periodicity indicated by DRS results in a cogging torque frequency of 53.2 Hz for the 133-rpm test run and 67.6 Hz for the 169-rpm test run. These frequencies correspond with the fundamental electrical frequency of the generator.

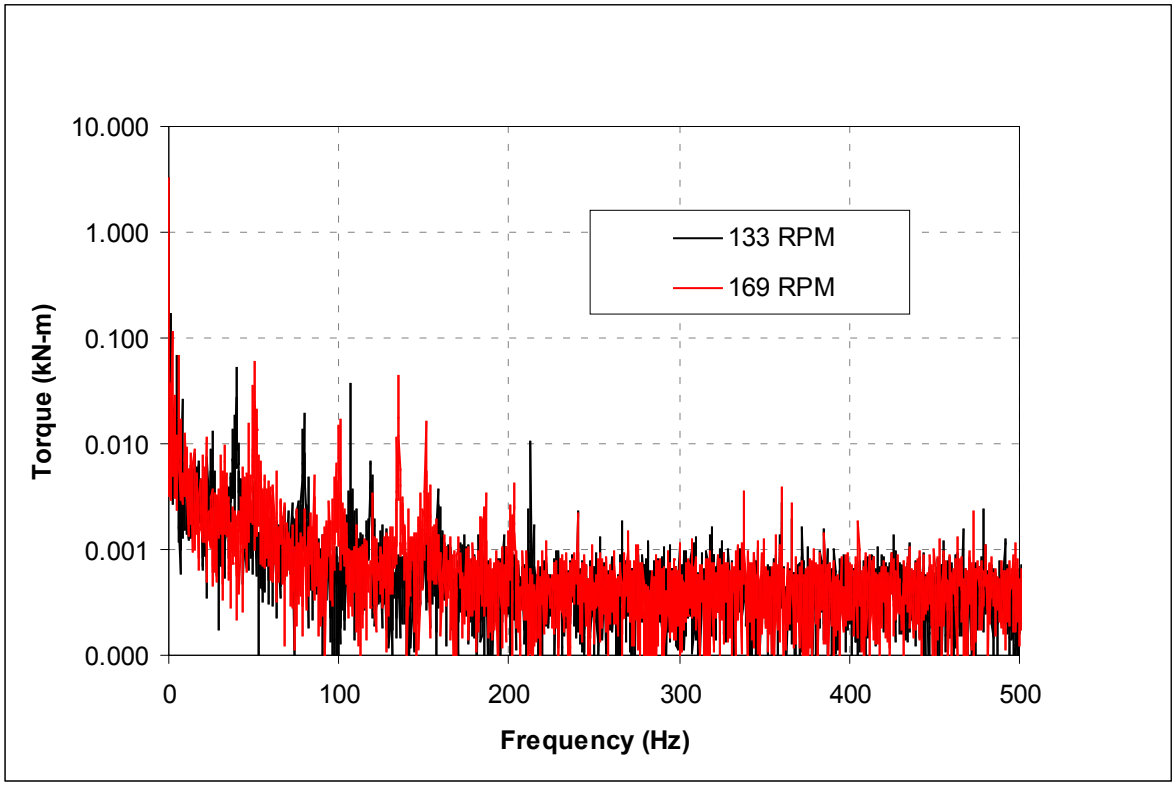

Figure 33. Generator no-load torque

5.1.2.2 Current Balance

Figure 34 shows the current imbalance between generator quadrants for a subset of the test data. The current imbalance between generator quadrants is relatively low and does not appear to be a function of load. The current imbalance between the four quadrants varies from 0.8% to 1.3% indicating that the core and windings are relatively uniform. The results in Figure 34 are based on approximately 30,000 10-second records.

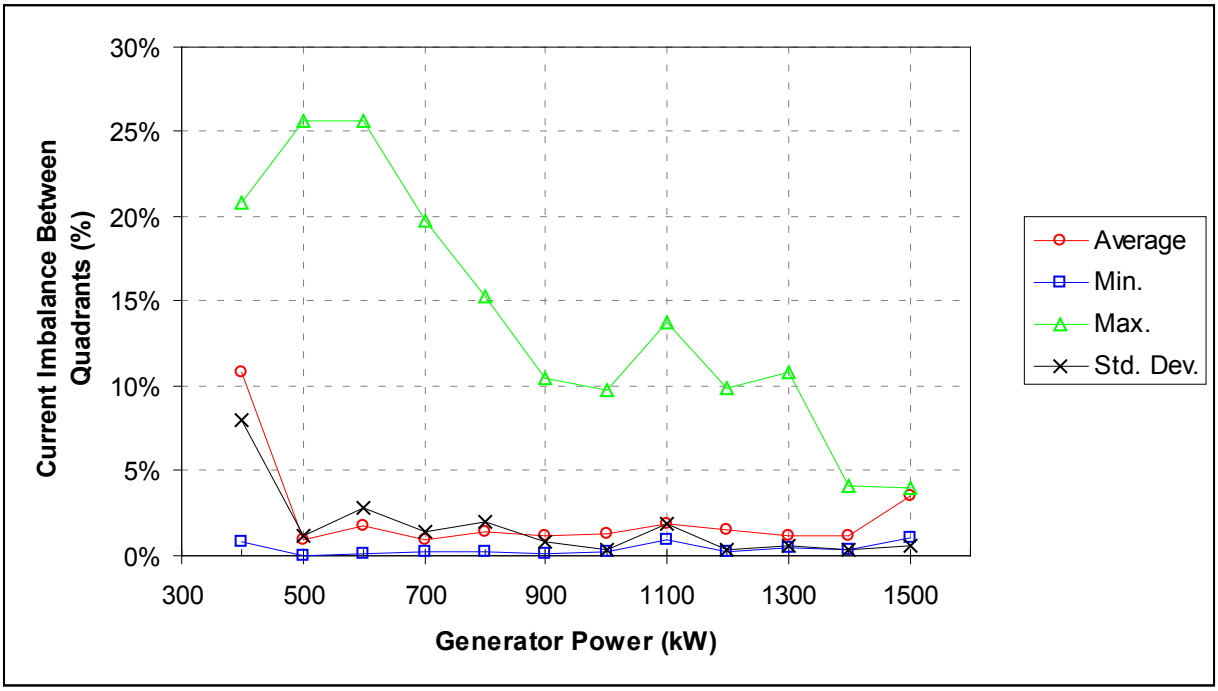

Figure 34. Generator current imbalance

5.1.2.3 Power Electronics

Figure 35 contains the average power factor of the inverters. The average power factor presented in Figure 35 is based on a total of 83 hours of data during power production. The power factor of the inverters is close to unity when the output power is below rated; however, the power factor drops below 0.99 at rated power.

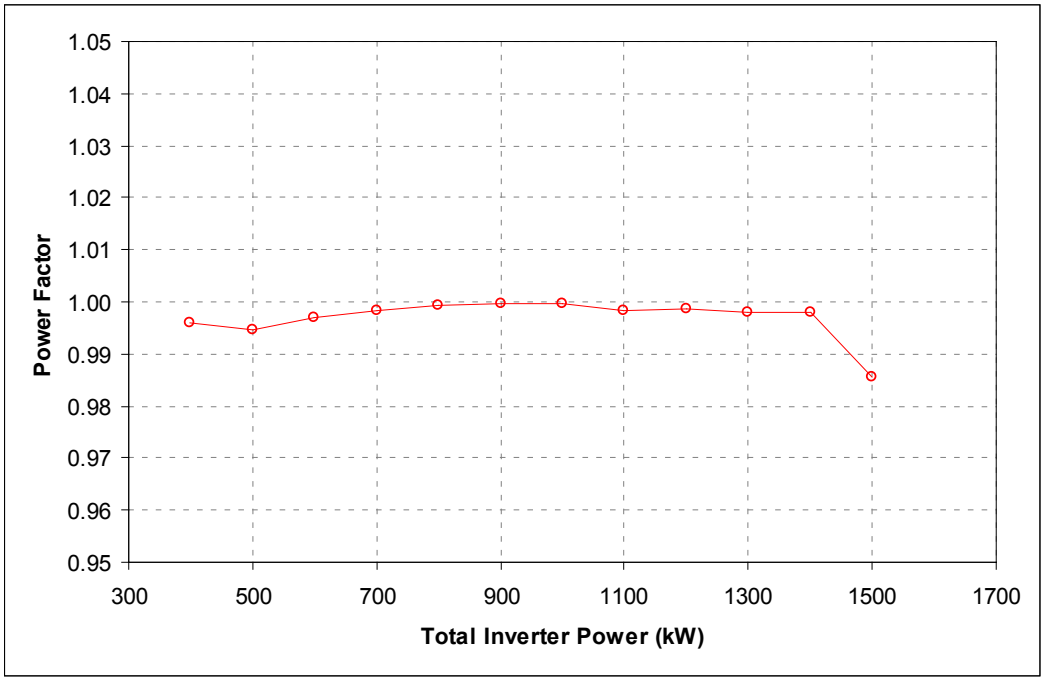

Figure 35. Inverter power factor

5.1.3 Gearbox Characterization

5.1.3.1 Ring Gear Tooth Load Distribution

The test article planetary stage gearbox includes a unique double-helical gearing arrangement that inherently centers the planets in the ring gear and avoids introducing any thrust load into the planets. The sun gear, in turn, "floats" between the three planet gears and does not require any thrust reaction.

The double-helical ring gear was challenging to manufacture, but the accuracy of the gearing was excellent in the end. The ring gear teeth were designed with lead correction to avoid contact at the ends of the teeth. Each tooth was modified to have a slight crown, so that at low load the contact period with the mating tooth on the planet gear would be short, and would increase gradually as the load increases. To verify the lead correction on the ring gear teeth, strain gages were bonded to the root of selected teeth at four positions along the tooth from one side to the other. Three azimuthal locations on the ring gear were instrumented at 120° apart, and were designated as X, Y, and Z. Position X is 180° from top dead center (TDC). Position Y is 300° clockwise from top dead center when looking at the rotor side of the gearbox. Position Z is 60° clockwise from TDC when looking at the rotor side of the gearbox. For each location, the upwind half of the double-helical gear is designated as A and the downwind half as B. Note that the four strain gages at each location were configured into one bridge, and were staggered over 11 teeth so that only one gage in the bridge would be loaded at any one time. Figure 36 shows a roll-out of the strain gage installation.

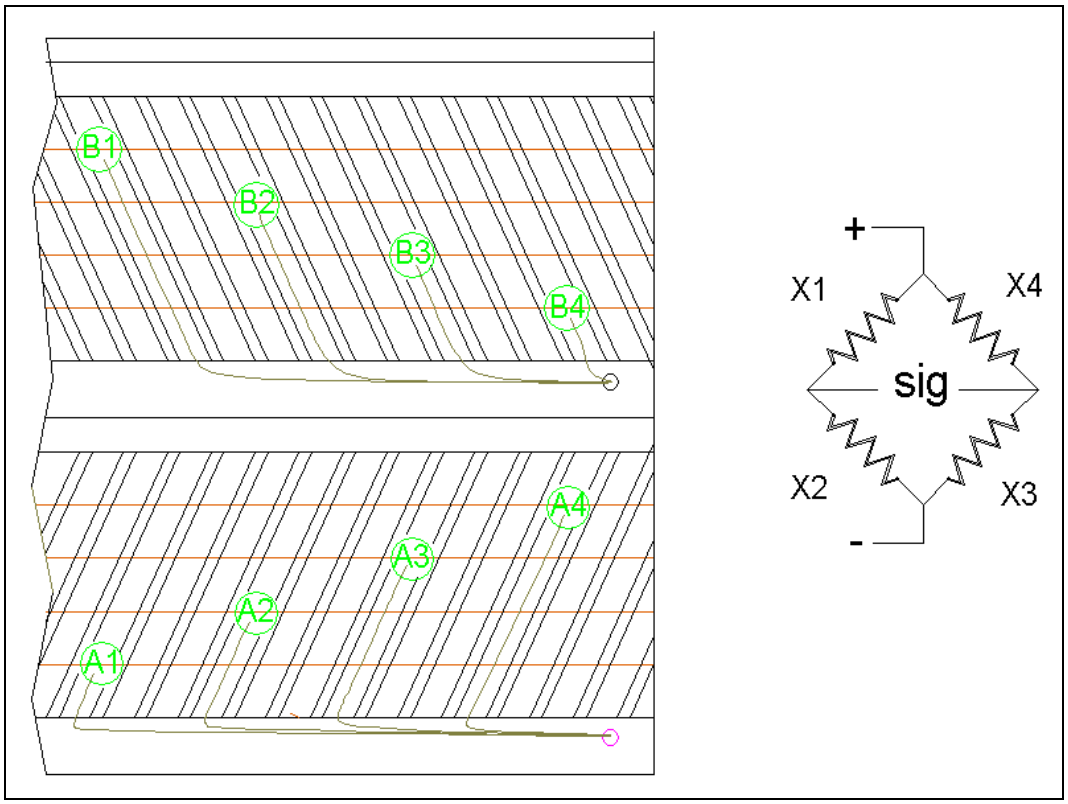

Figure 36. Ring gear strain gage configuration

Figure 37, Figure 38, and Figure 39 show typical signals from each of the strain gage bridges during operation at 1,104 kW (approximately two thirds full load). Note the characteristic humps that occur as each gage in the bridge is successively loaded.

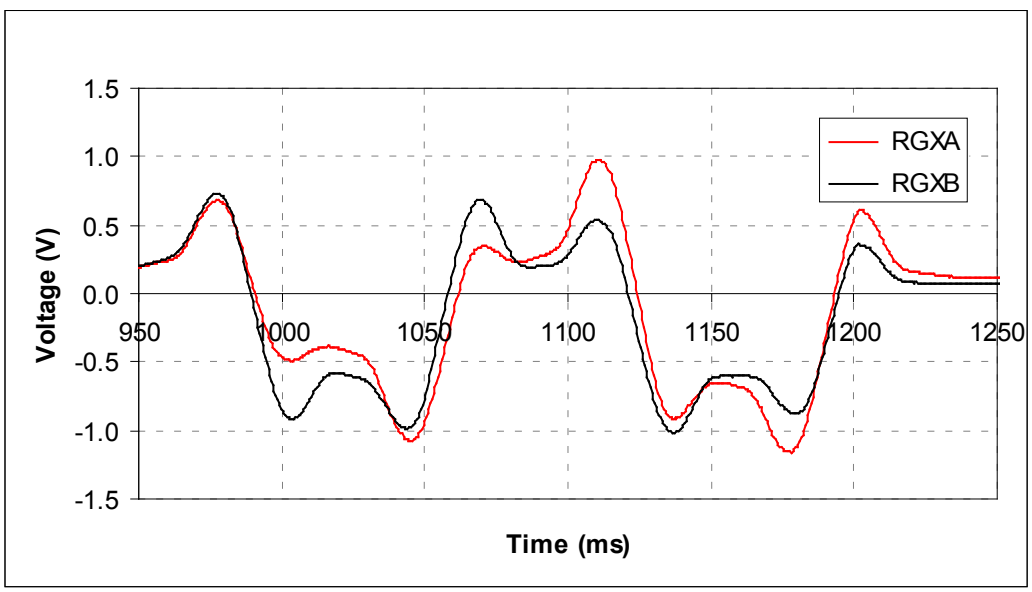

Figure 37. Ring gear strain gages at X position

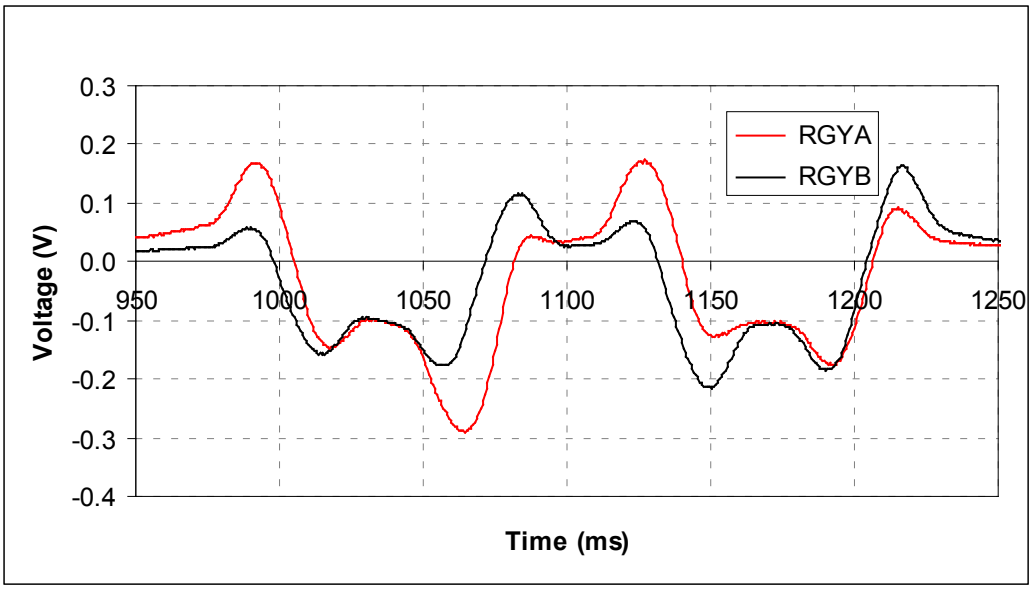

Figure 38. Ring gear strain gages at Y position

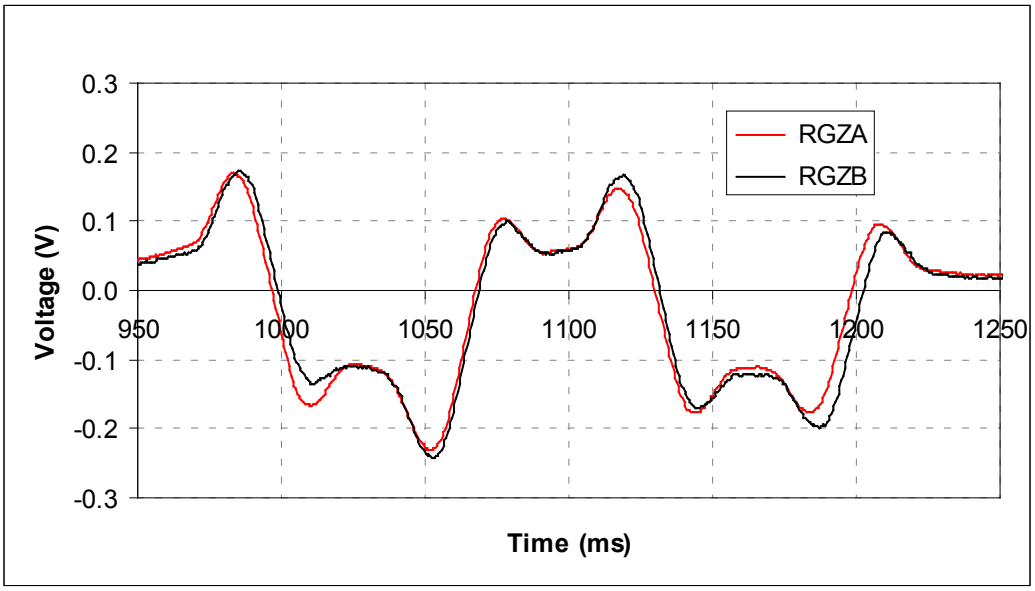

Figure 39. Ring gear strain gages at Z position

Figure 40 shows how the peaks in the signal can be interpreted to derive the relative load at each gage location. This technique was applied to the data from four load stages to investigate how the relative strain at each gage changes with increase in load.

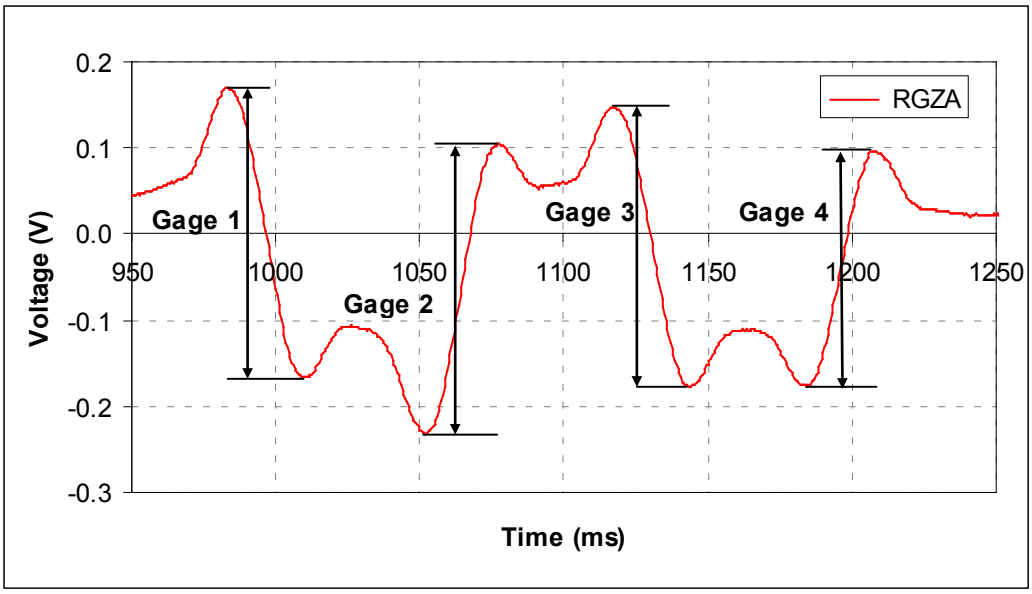

Figure 40. Measuring change in strain level

Figure 41 is plot of the tooth load distribution for each location along the teeth at the X, Y, and Z positions during operation near rated power.

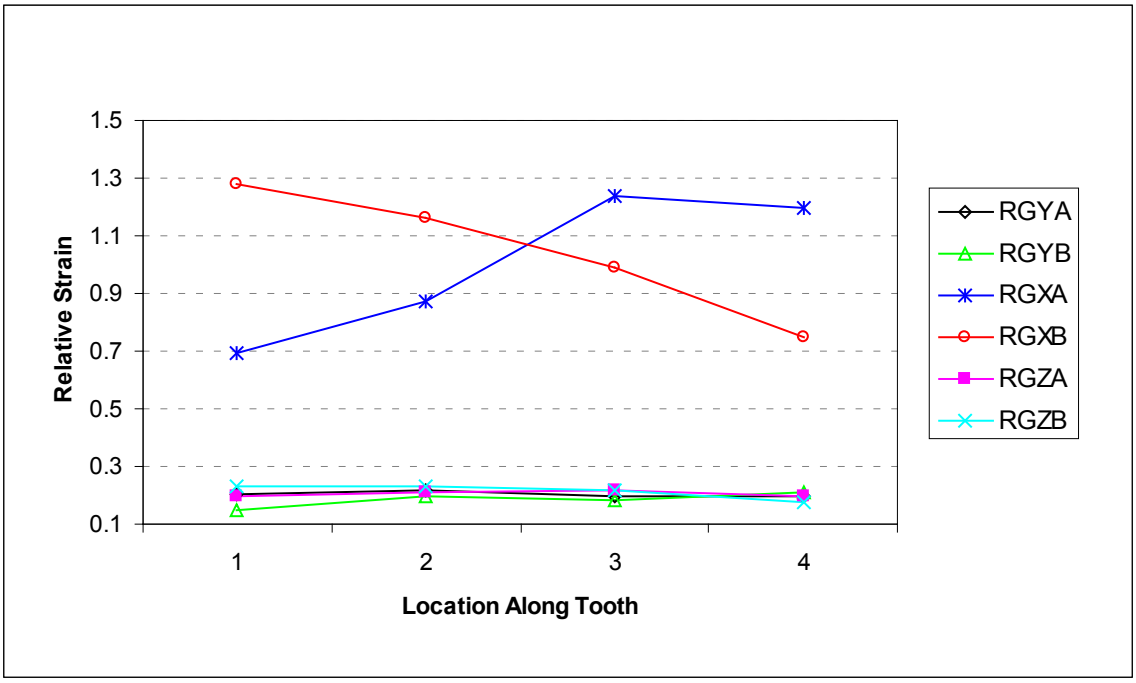

Figure 41. Tooth load distribution at 1,448 kW

The load distributions across the teeth are not uniform. The potential causes for these differences in strain levels include the following.

- Helical cut of the gears: The expected loading distribution, as designed, is not perfectly uniform.

- Parallel alignment of planet gears: The annulus gear, due to its manufacturing processes, has much greater eccentricity error. The right and left helices are finished separately, subject to limitations of relocation after disturbing the work piece between finishing the two helix hands. This non-concentric location of pitch cylinders causes mating gears to relocate their apexes until helical thrust forces are equalized. Due to their spherical bearing mounting, this will be automatic for the planets. This displacement of the apex center at the annulus gear, in relation to the sun pinion apex, creates a slope in the planet axis. Not all planets have the same slope, because they are engaged at different places in the apex displacement pattern. Repeated test runs at various loads would quantify the repeatability of the strain measurements to help isolate planet gear self-alignment versus instrumentation or manufacturing errors.
- Axial position of the sun gear: The data in Figure 53 show changes in sun gear displacement as load changes, corresponding to load changes in the ring gear due to realignment of the planet gears.
- Input shaft alignment: The load distribution shown in Figure 41 shows the relative strain at position X (bottom dead center) is approximately three to six times greater than at positions Y and Z. This indicates the carrier has a downward vertical loading component. This simply might be self-weight of the carrier and planet gears. It also could be due to uneven input-shaft loading caused by an alignment error. Vibration data from accelerometers on the main bearings does reveal an elevated main shaft once-per-revolution (1P) signal, but the accelerometers are mounted horizontally and are integrated circuit piezoelectric (ICP) accelerometers, which cannot reliably measure magnitude at frequencies below 1 Hz.
- Instrumentation errors: These could include calibration, scaling, and other errors. These types of instrumentation errors were not noted during or after the testing; additionally, in accordance with the test plan (document number N600006 R7), the ring gear strain measurements are relative measurements and are not calibrated to a particular load.
- Strain gage placement: These effects could be studied using finite-element method models to determine whether they are significant. Placement issues can be related to the location and orientation of the strain gages. Location of the strain gages along the length of the valley between teeth is expected to have minimal effect. Location errors in the transverse direction (perpendicular to the valley) could be significant due to the asymmetrical cross-sectional shape of the tooth, but tip clearances of the planet gear tooth tip to the ring gear root preclude much alignment error before the strain gage and wiring would interfere with the mesh. Angular errors in gage placement also could be significant, but these were not studied.

Figure 42 and Figure 43 show the measured load distribution for the gages at the Z location, derived by measuring the relative change in strain using the method depicted above. Note that, as the load increases from 573 kW to 1,448 kW, the line tends to level out. This indicates that the load is more evenly distributed across the tooth. This change in load distribution possibly is due to the helical cut of the gears. As the load increases, the gear teeth deflect and transfer the load more equally along the tooth face.

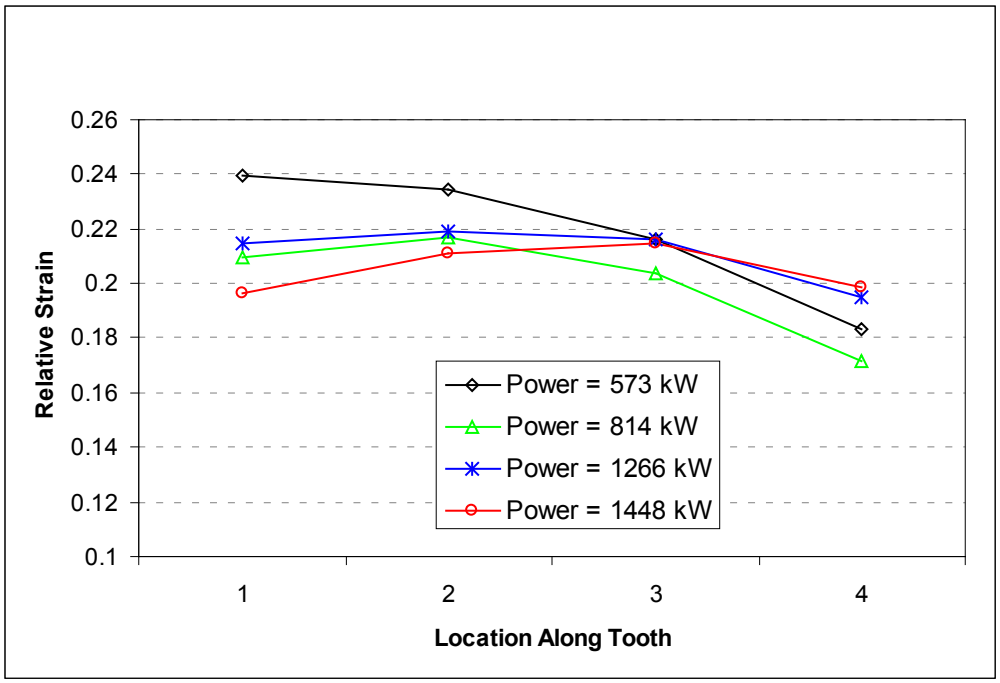

Figure 42. Tooth load distribution from the strain gauge bridge, RGZA

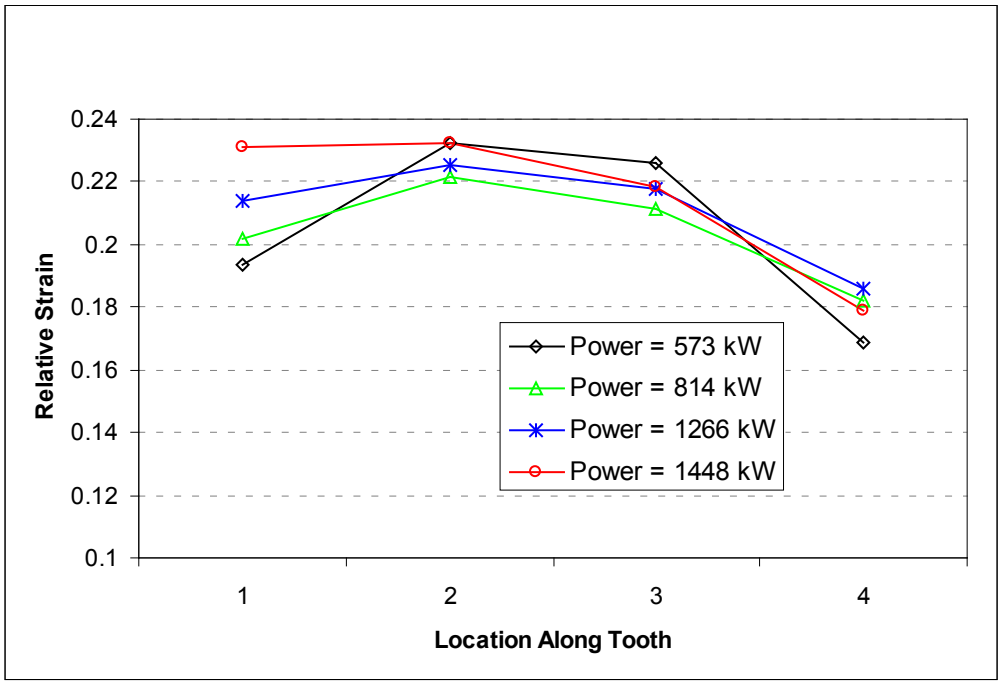

Figure 43. Tooth load distribution from the strain gauge bridge, RGZB

Figure 44 and Figure 45 show the measured load distribution for the gages at the Y location. The signals from the gages at the Y location show a more pronounced flattening out with load increase. The data also show some planet misalignment between the A and B meshes, which decreases with load as expected in the design. Figure 45 shows an undesirable load distribution

at low power, indicating the planets might not self-align as freely at lesser loads. The criticality of this condition on planet bearing roller skidding and gear-tooth loading should be investigated further. Longer runs at various power settings are necessary to determine the duration and magnitude of misalignment, and strain gage load calibration would be necessary to compare the tooth load with the design-load limits.

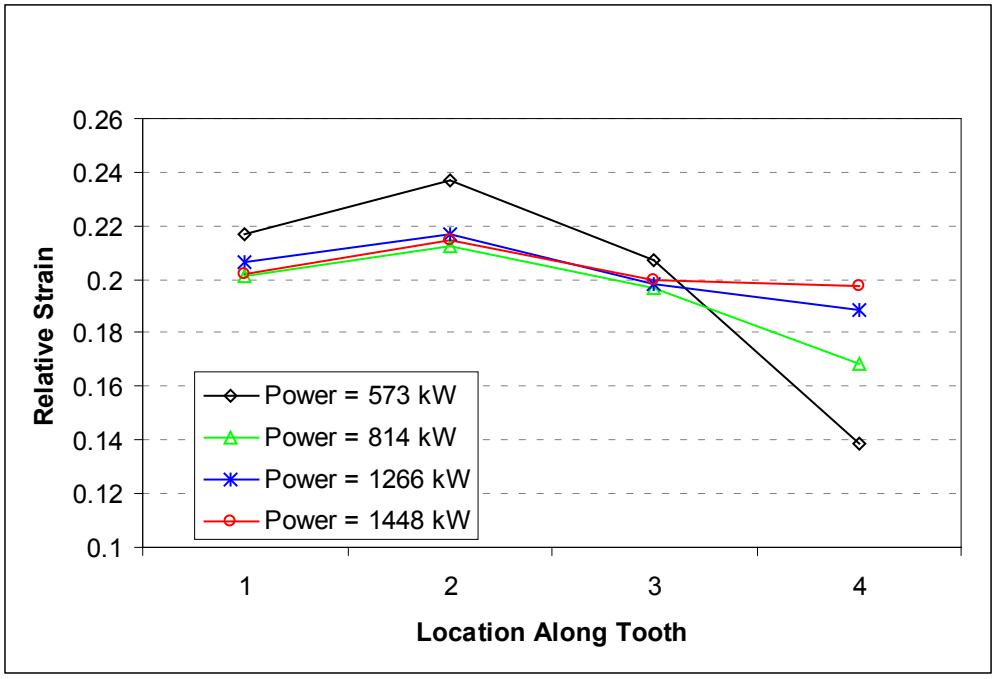

Figure 44. Tooth load distribution from the strain gauge bridge, RGYA

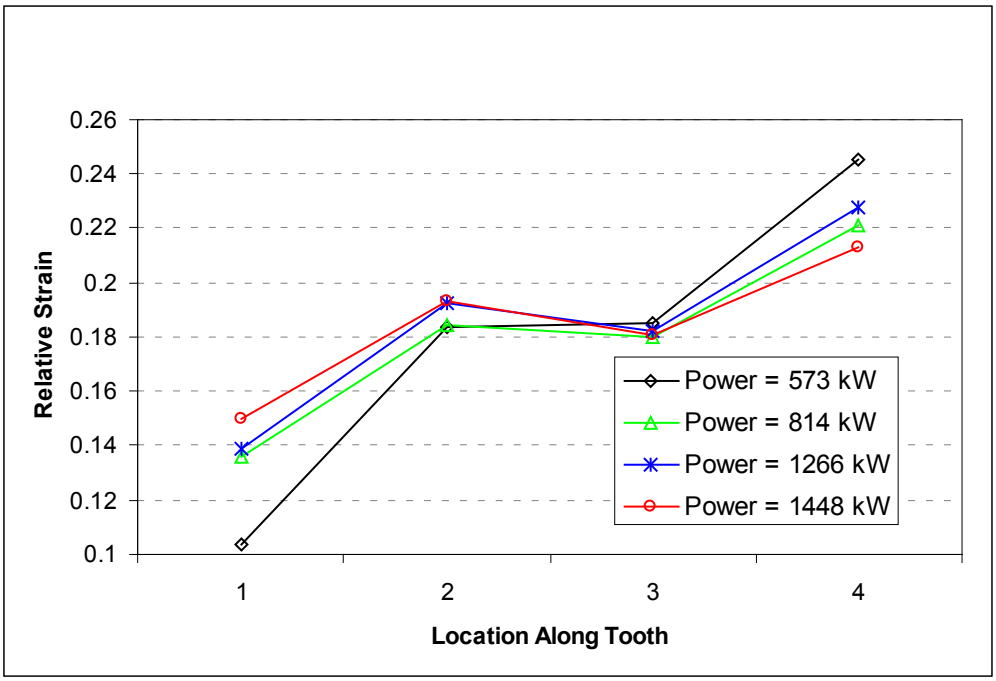

Figure 45. Tooth load distribution from the strain gauge bridge, RGYB

Figure 46 and Figure 47 show the measured load distribution for the gages at the X location. The relative strains at location X are several times greater than at locations Y and Z for each location along the tooth.

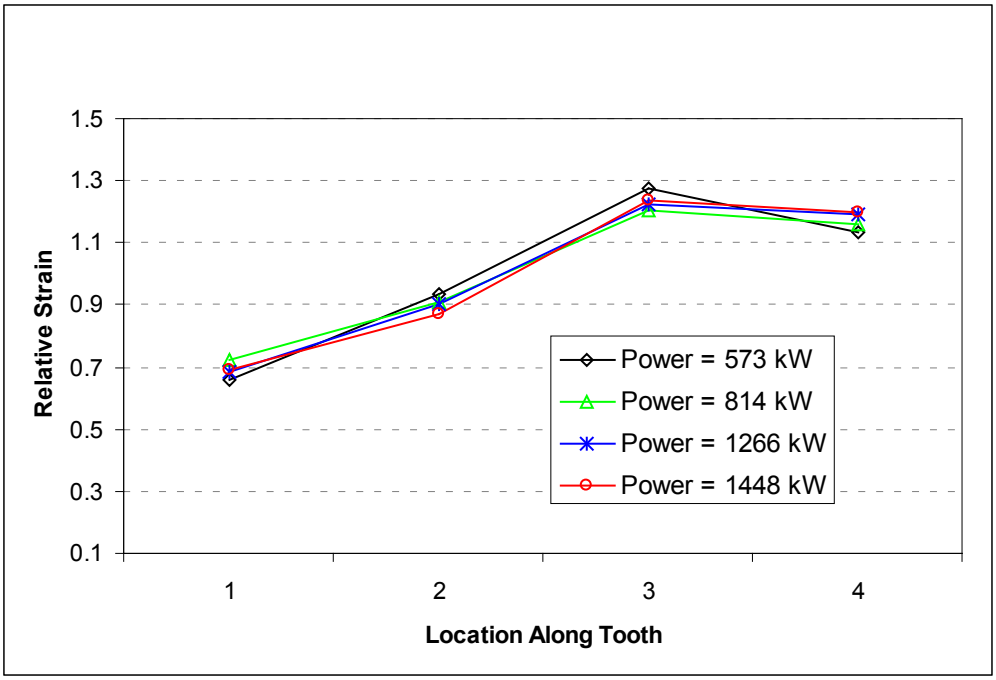

Figure 46. Tooth load distribution from the strain gauge bridge, RGXA

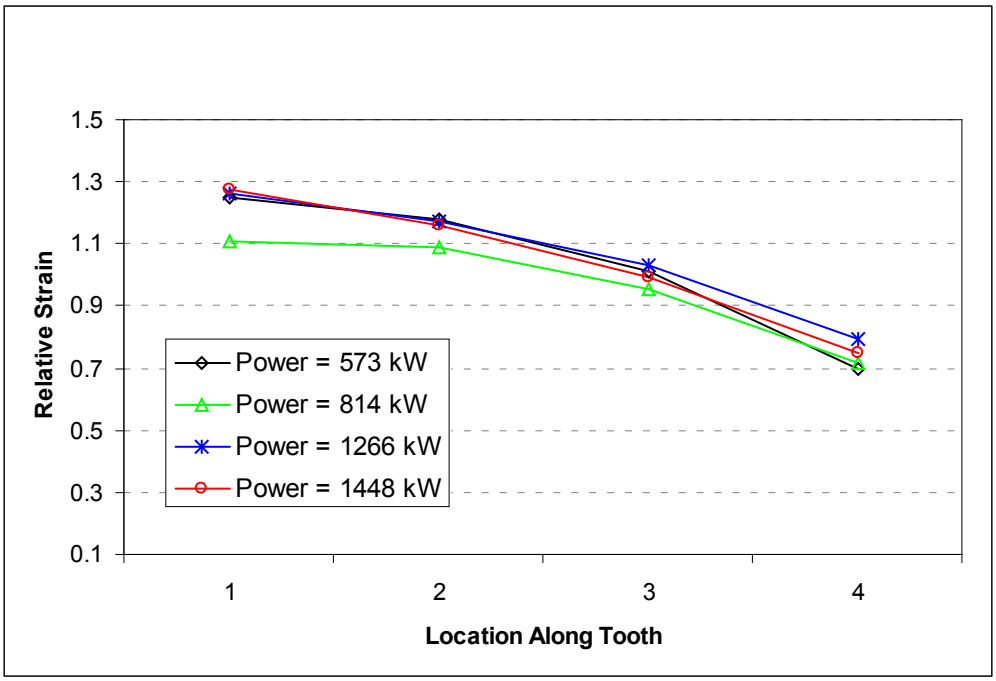

Figure 47. Tooth load distribution from the strain gauge bridge, RGXB

Although the general shape of the curves for location X exhibit good behavior and are similar in shape to those for the other locations, the gages at the X location show very little change in distribution across the length of the tooth as load increases. This could be due to the increased loading from self-weight or the alignment of the input shaft. The loading on the planet bearing rollers is distributed more evenly across the rollers (as described in Section 5.1.3.5), consequently there is much less flattening in relative strain from position 1 to 4 as load increases. The tooth loading due to sun pinion offset corresponds to the design documentation, and is shown in Figure 48.

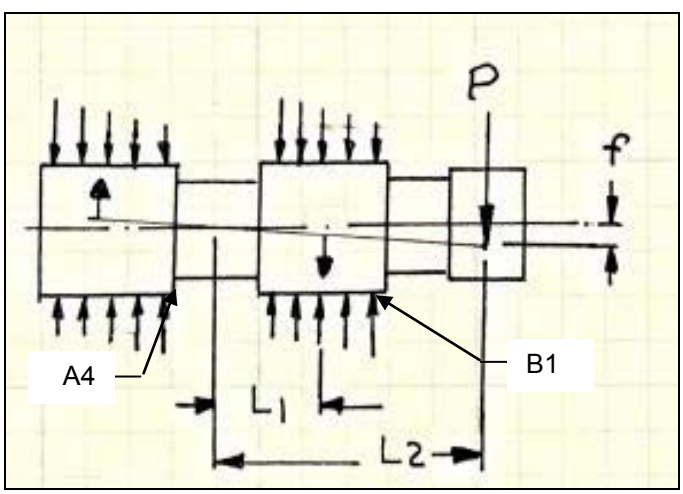

Figure 48. Tooth loading caused by pinion offset

5.1.3.2 Sun Gear and Torque Tube Motion

The gearbox arrangement includes a "floating" sun gear that is captured by the three planet gears on one end, and which transmits torque to the generator through a hollow torque tube that is fixed to the generator rotor as shown in Figure 49. The sun gear connects to the torque tube with a splined connection, so it can move a small amount axially. Additionally, the torque tube is connected to the generator rotor through a flexible diaphragm so that it can compensate for some axial misalignment. The intent of these features is to isolate the sun gear and the generator so that only torque is transmitted, and any misalignment of the various components will not be transferred into axial misalignment of the sun gear and planet mesh.

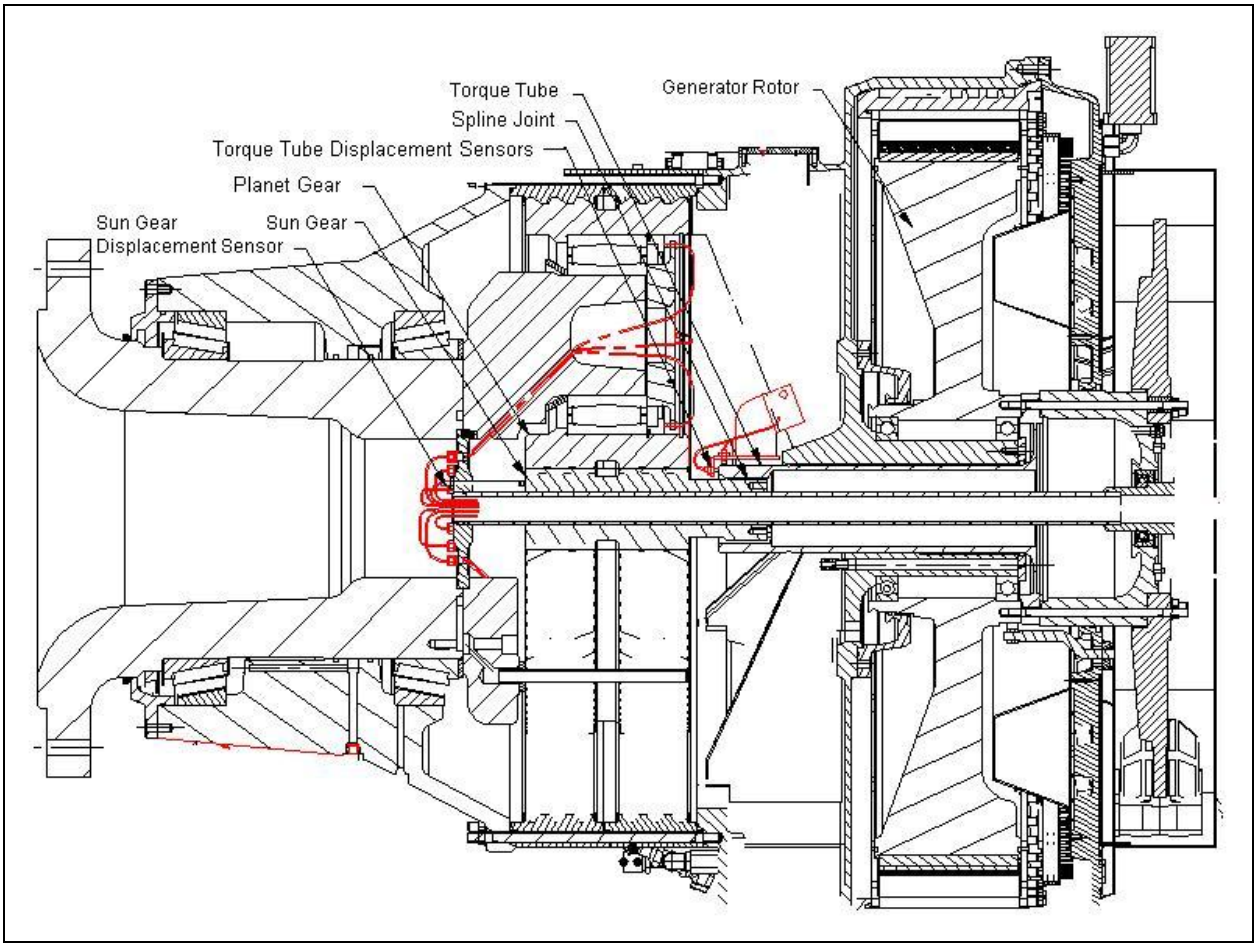

Figure 49. Test article cutaway

To verify the effectiveness of the splined connection between the sun gear and torque tube, proximity sensors were installed to measure the axial displacement of the sun gear and of the torque tube. Figure 50 shows the axial motion of the sun gear and of the torque tube when the generator output was 814 kW. The planet passage trace in Figure 50 indicates the periodicity of the planet gears. The frequency of the planet gear passage is three times the frequency of the carrier rotation. Each spike in the planet passage trace marks the passage of one of the planet gears past a fixed point on the ring gear. It is expected that because the sun gear is captured by the planet gears—which in turn follow the circumferential path of the ring gear apex—any variation in the ring gear apex due to manufacturing error or distortion will be reflected in the

sun gear axial motion. The traces show that the axial motion of the torque tube is on the order of 150 microns peak-to-peak. Even without the subtraction of sun pinion displacement (spline slip), as shown in Figure 50, this is well within the design parameters, which provide calculations for sun pinion displacements of up to 550 microns.

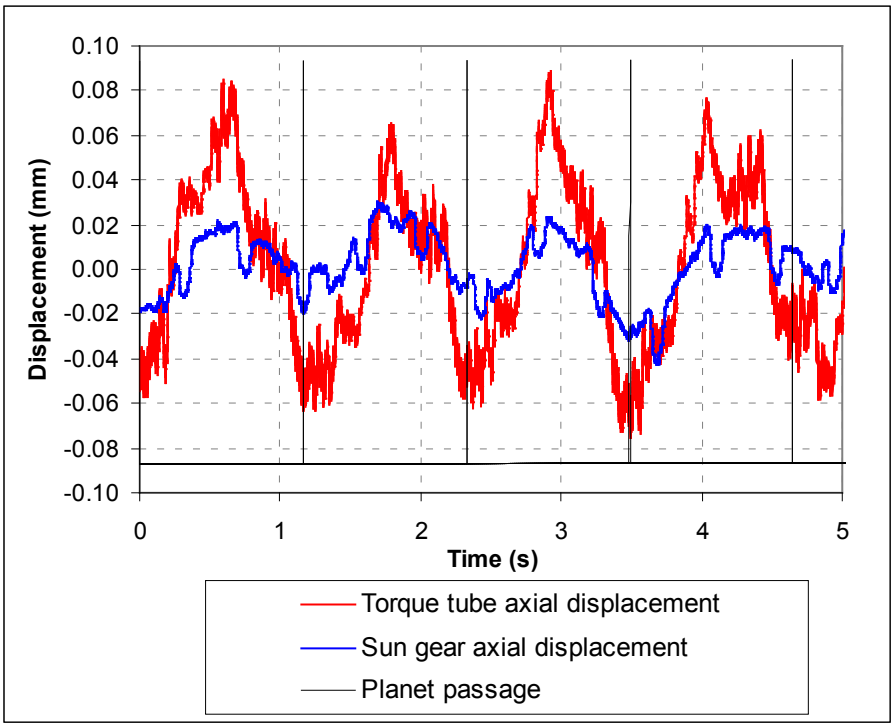

Figure 50. Sun gear and torque tube axial displacement

It also is interesting to evaluate the effectiveness of the spline connection in isolating the ring gear and the torque tube. Figure 51 shows the relative axial motion between the sun gear and the torque tube, again with the planet gear passage trace included. Note that the relative motion is almost equal to the sun pinion motion, indicating that the spline is not compensating for gear mesh thrust loading to nearly the extent that the flexible diaphragm of the torque tube compensates.

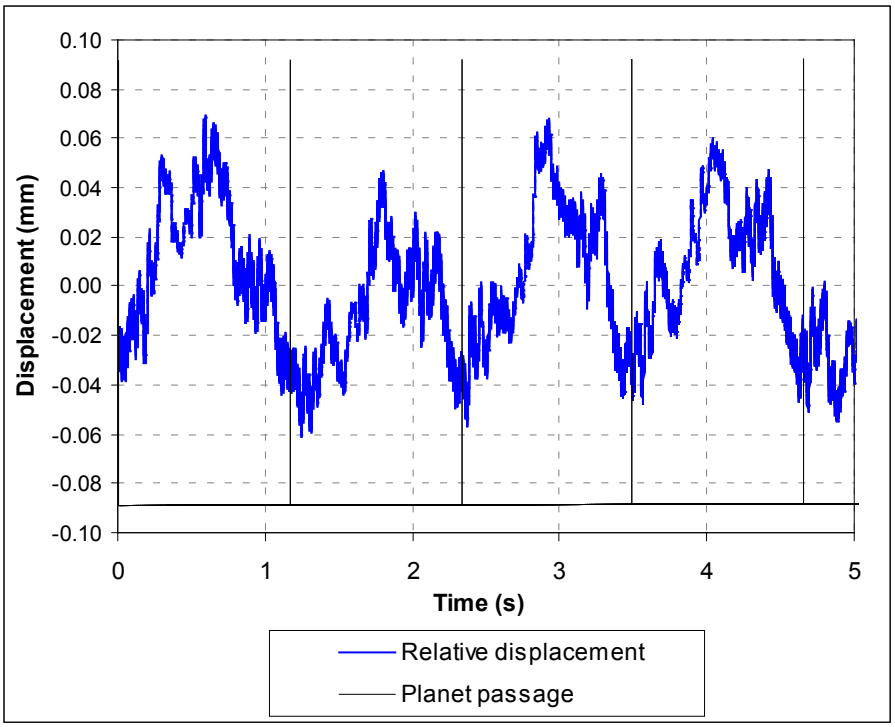

Figure 51. Relative sun gear and torque tube axial displacement

Lastly, a proximity sensor was installed to measure the radial motion of the torque tube. This measurement, shown in Figure 52, reflects the misalignment between the axis of the sun gear and the axis of the generator or ring gear. The frequency of the displacement identifies the pertinent misalignment. Superposed is the marker for the generator 1-per-revolution (generator revolution). Note that the range of motion is approximately 200 microns, which is greater than expected, but it could be a reasonable misalignment for the gearbox and generator housing which support these large parts.

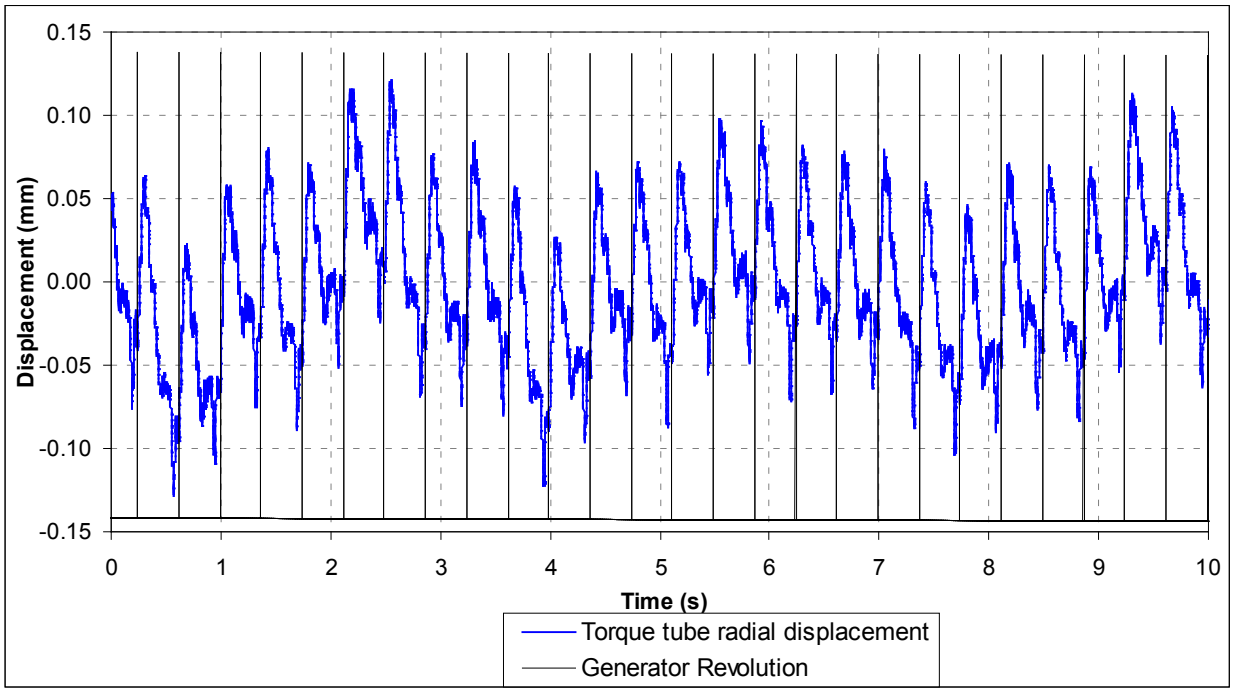

Figure 52. Torque tube radial displacements

Figure 53, Figure 54, Figure 55, and Figure 56 are plots of the mean, minimum, and maximum sun gear axial displacement; torque tube axial displacement; torque tube radial displacement; and relative axial displacement between the sun gear and the torque tube. Figure 55 shows that radial position does not change with load. This might further support other data that indicate an assembly alignment error.

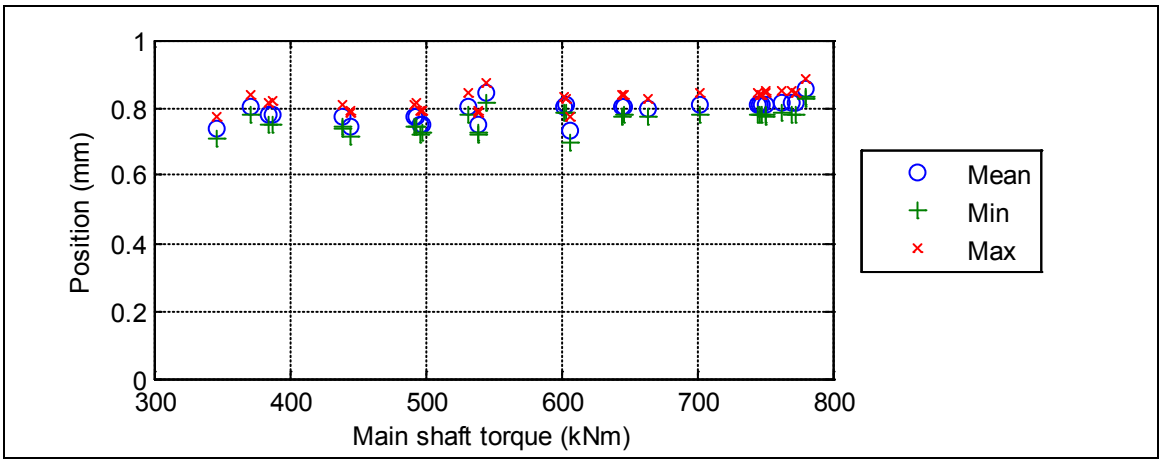

Figure 53. Sun gear axial position

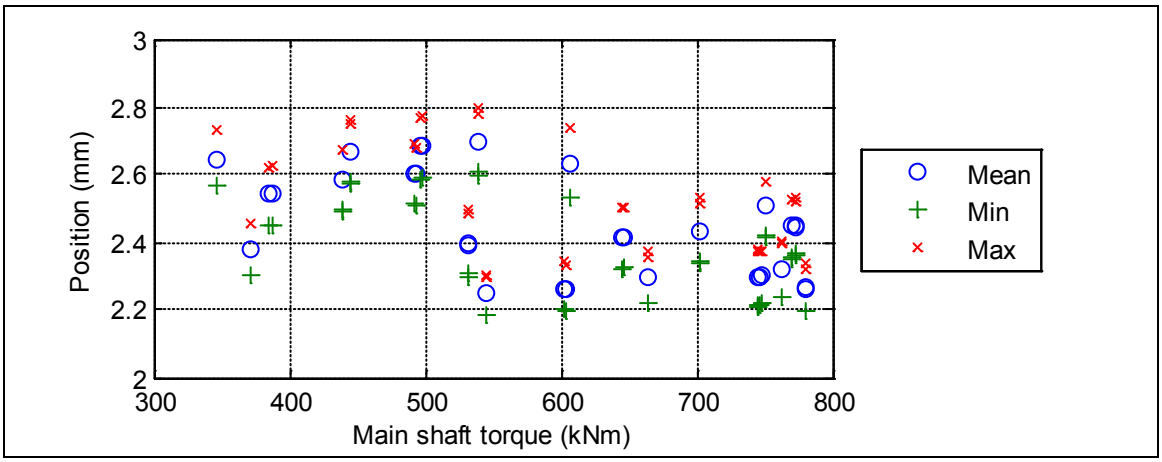

Figure 54. Torque tube axial position

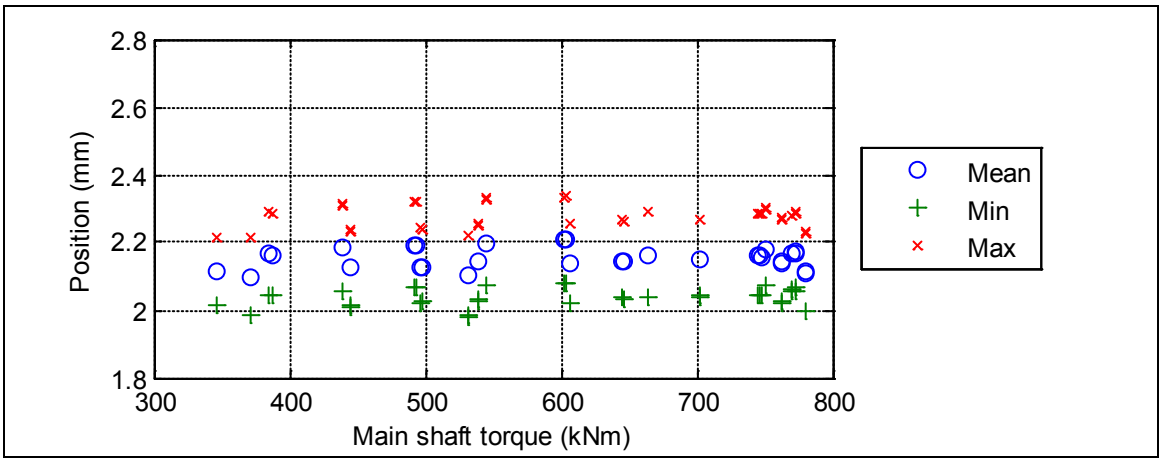

Figure 55. Torque tube radial position

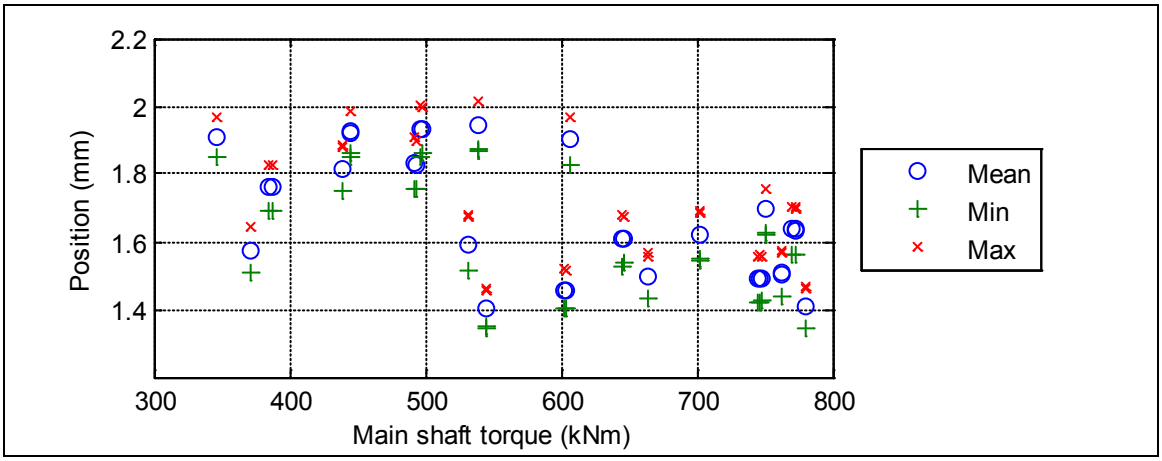

Figure 56. Relative axial displacement between sun gear and torque tube

Figure 57 is an overlay plot of the sun gear, torque tube, and relative sun gear–torque tube displacements. Although the position of the torque tube changes with load, the magnitude of displacement of the sun gear and torque tube is independent of load.

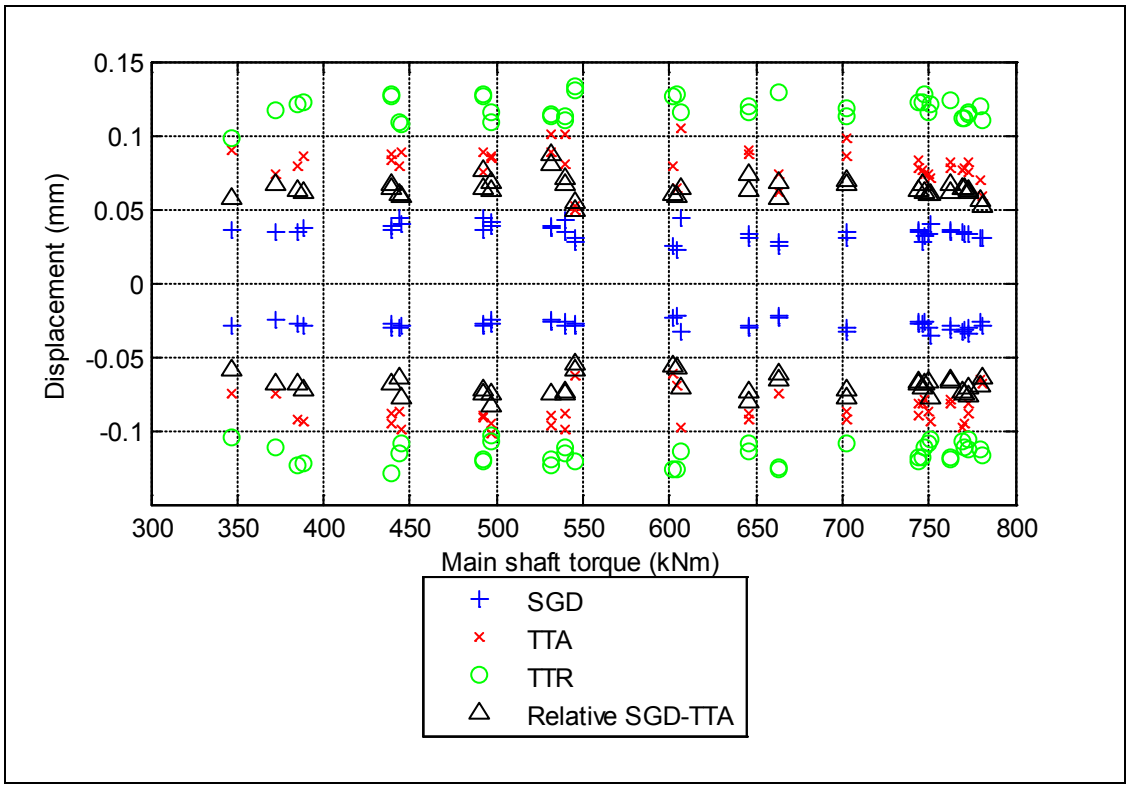

Figure 57. Sun gear and torque tube axial displacements

5.1.3.3 Planet Gear Instrumentation

Instrumentation was installed in the planetary section of the gearbox to measure various characteristics of the planet gear and bearing loading. Figure 58 shows the location of this instrumentation (discussed in more detail below). Figure 59 shows the instrumentation installed.

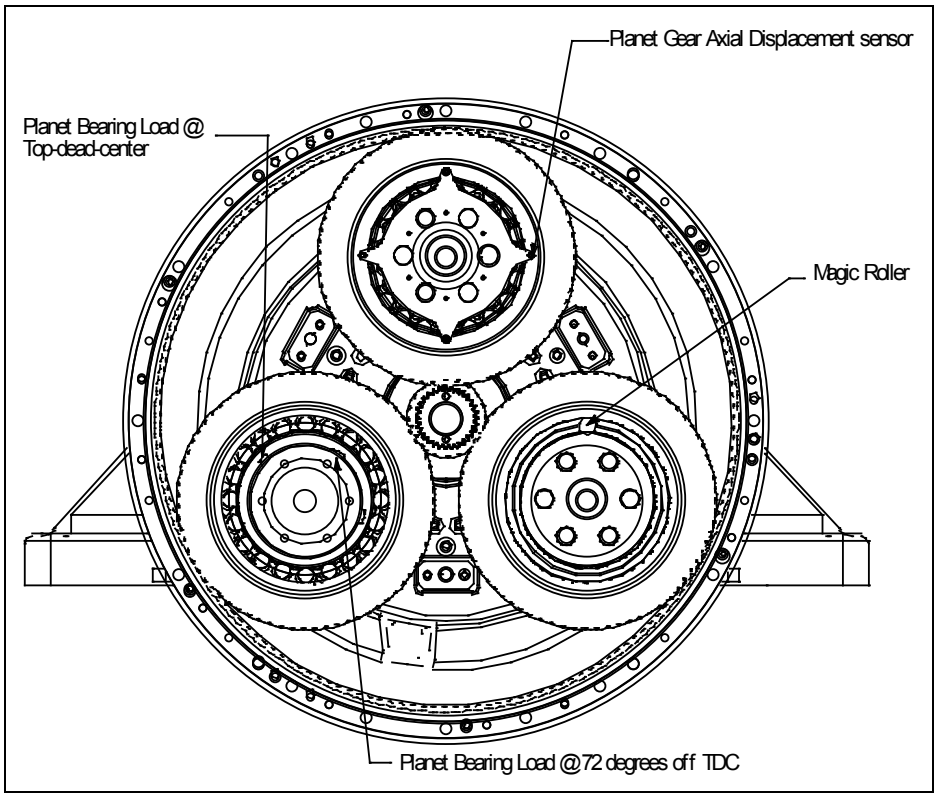

Figure 58. Planetary gear instrumentation location

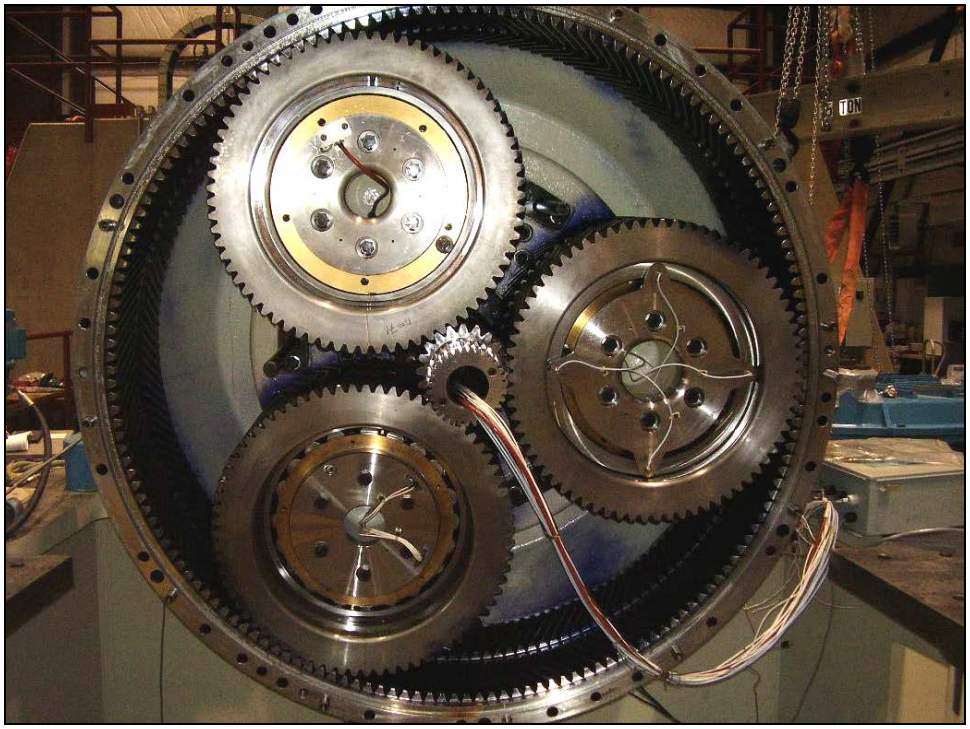

Figure 59. Planetary gear installed instrumentation.
(Photo credit: Chris Walford, DNV Renewables)

5.1.3.4 Planet Gear Alignment

As noted, the double-helical gearing arrangement is intended to capture the planet gears axially. Any axial motion of the planet gears is a reflection of the axial run-out of the ring gear apex. To measure this motion and detect axial deflection of one planet gear, proximity sensors were installed on the carrier at four different locations relative to the planet carrier—outboard, leading, lagging, and inboard. The inboard sensor was not functional and is excluded from the results. The input shaft does not impart thrust loads during this test, therefore the carrier can be assumed to be axially unloaded during testing, making it a suitable reference point for axial-deflection measurements relative to the housing.

Figure 60 shows a representative time series of the axial displacement from the sensor at the lagging position. Note that a very small component of the generator 1P motion is reflected in the planet motion (approximately 5 to 10 microns) through the torque tube and sun gear, but this is overwhelmed by the 1P of the carrier. The axial deflections of this planet are shown to vary by only approximately 25 microns. There appears to be relatively little ring gear axial variation as the planet travels around the ring gear perimeter, assuming that the carrier axis is aligned closely with the ring gear axis.

Figure 50, however, shows the sun gear axial deflections to vary approximately 150 microns due to planet passage. This is significantly greater than the axial variations of the single, instrumented planet as measured relative to the carrier. This is consistent with the design expectations for the floating sun pinion.

DNV did not perform additional testing to investigate the causes for these findings. The effects of generator alignment—or misalignment—relative to the ring gear, planets, and sun gear on tooth loading were not investigated. Misalignment between the generator and the gear box, however, could be the cause for some of the results.

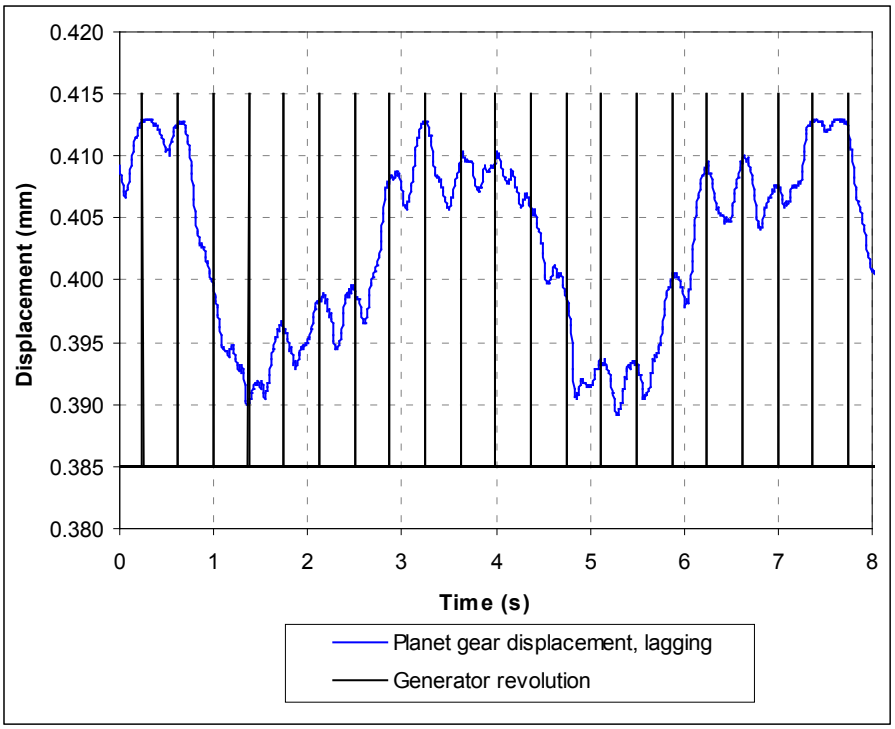

Figure 60. Planet gear axial displacement, lagging

The outboard, leading, and lagging axial position of the instrumented planet gear position is shown in Figure 61, Figure 62, and Figure 63 as a function of load. The inboard axial position is not presented because the inboard displacement sensor was not functional. For each of these locations, the axial deflection scatter about the mean value frequently was less than 30 microns, indicating low sensitivity in planet axial displacement to applied torque as measured at the carrier.

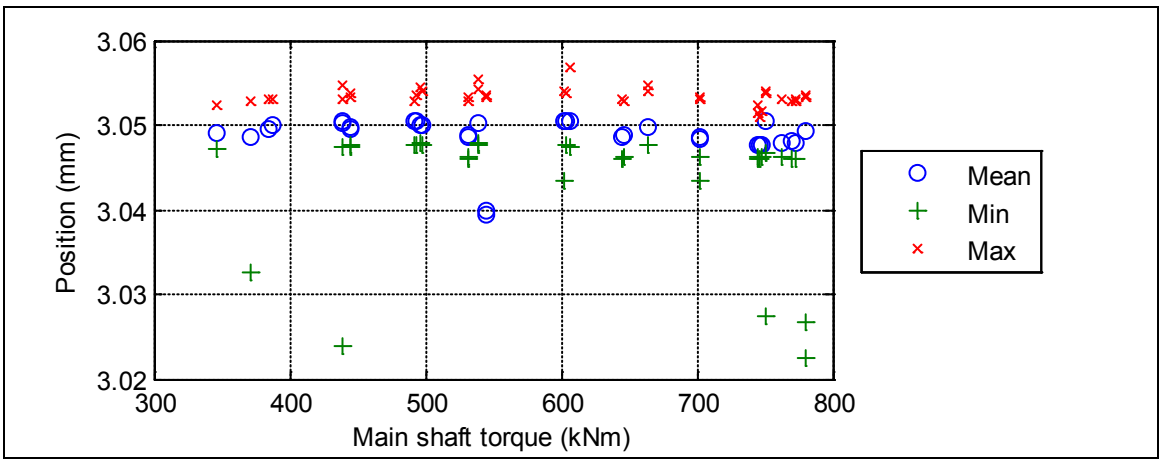

Figure 61. Planet gear axial displacement, outboard

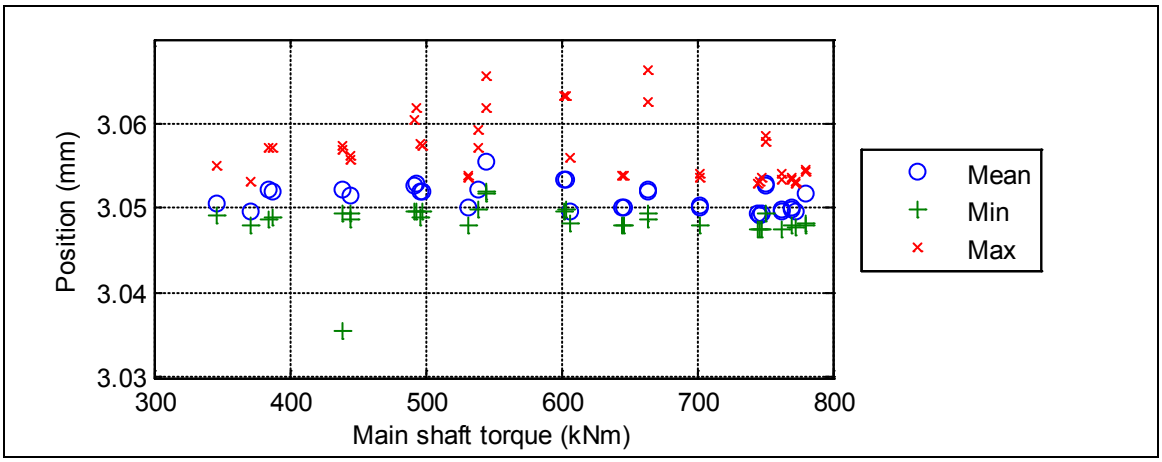

Figure 62. Planet gear axial displacement, leading

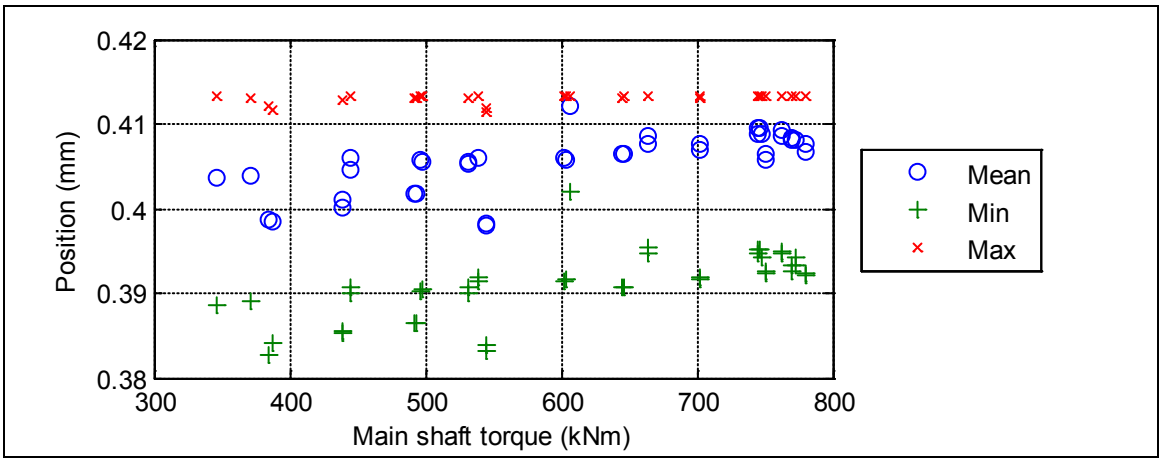

Figure 63. Planet gear axial displacement, lagging

5.1.3.5 Planet Bearing Load Distribution

The planet bearing load signals PBL1 through PBL8 derive from strain gages bonded to axial slots machined into the inner race of one of the planet CARB bearings. The strain gages react to the contact pressure from the roller load as the rollers pass over the slots. Figure 64 shows side and section views of the planet bearing. The orange outboard arrows indicate the load applied from the sun and ring gear during operation. The blue arrow indicates the reaction load in the bearing. The section view shows the unique "barrel" shape of the CARB rollers. This shape allows for some angular and axial misalignment between the inner and outer races of the bearing to accommodate inaccuracies and deflections in the planet carrier and gearing.

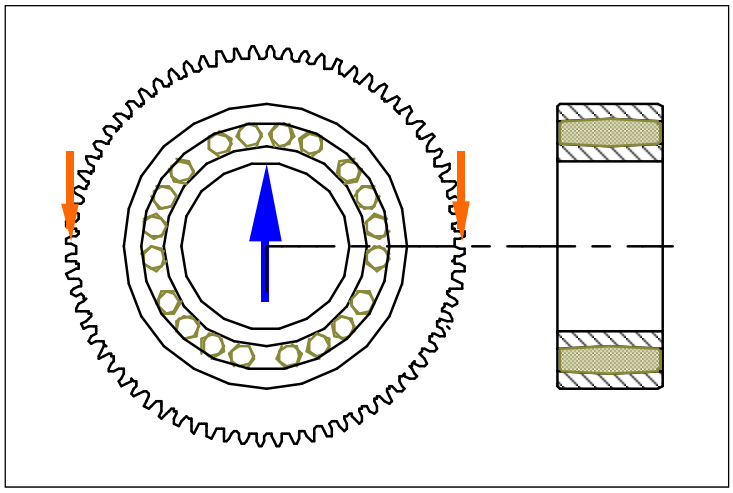

Figure 64. Planet bearing, side and section view

Figure 65 is a photograph of the instrumented planet bearing. The strain gage wires can be seen exiting the grooves in the bearing inner race (filled with black bonding compound).

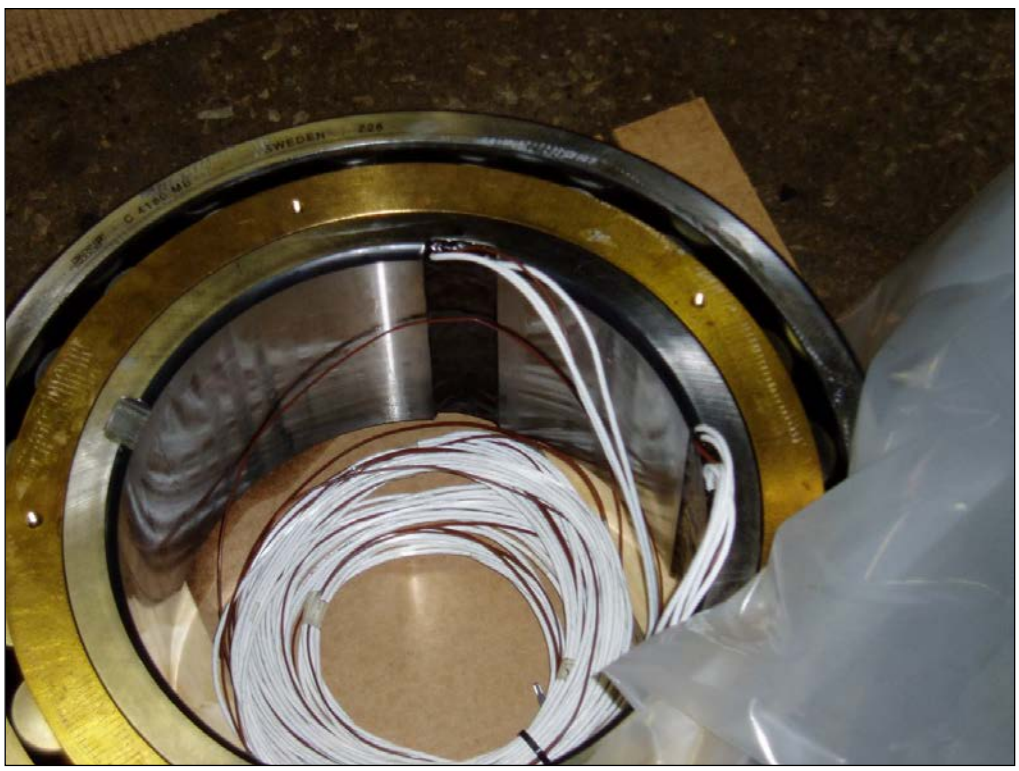

Figure 65. Instrumented planet bearing (Photo credit: Chris Walford, DNV Renewables Inc.)

Figure 66 shows a side view of the inner race of the planet bearing, and a "rollout" of the strain gage placement within each groove. There are eight strain gages; five in Slot A and three in Slot B. Slot A is oriented so that it is TDC relative to the reaction load in the bearing; this slot sees the greatest roller loads. Slot B is oriented 72° off from TDC. The roller loads at this slot location are much less than those found at Slot A. The reason for using two slots is to estimate the relative load at each azimuth location, and thus estimate the roller load distribution within the bearing.

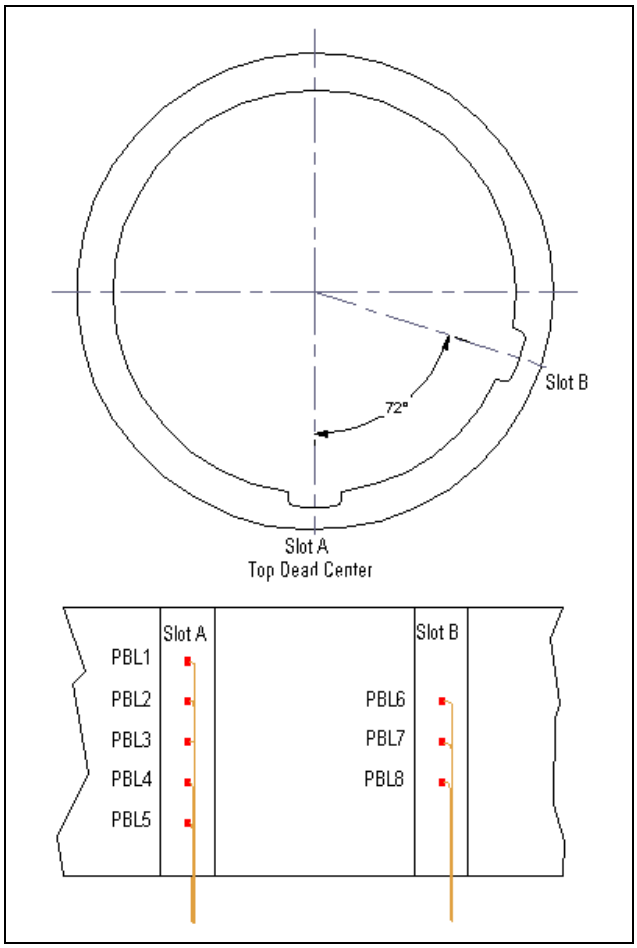

Figure 66. Planet bearing inner race, side view

Originally, the intent was to calibrate the planet bearing load signals to the applied load so that actual roller loads could be measured during operation. A calibration fixture was fabricated to enable measured loads to be applied to the instrumented bearing. Figure 67 shows the calibration fixture. The planet bearing inner race is mounted to an axle which is the same size as the planet carrier pin. This axle is mounted into roller bearings on either end so that it is free to rotate. The planet bearing outer race is mounted into a loading block that is fabricated to apply load at either side of the bearing (TDC +/- 90°) to simulate the actual loading of the planet as shown in Figure 64 (above).

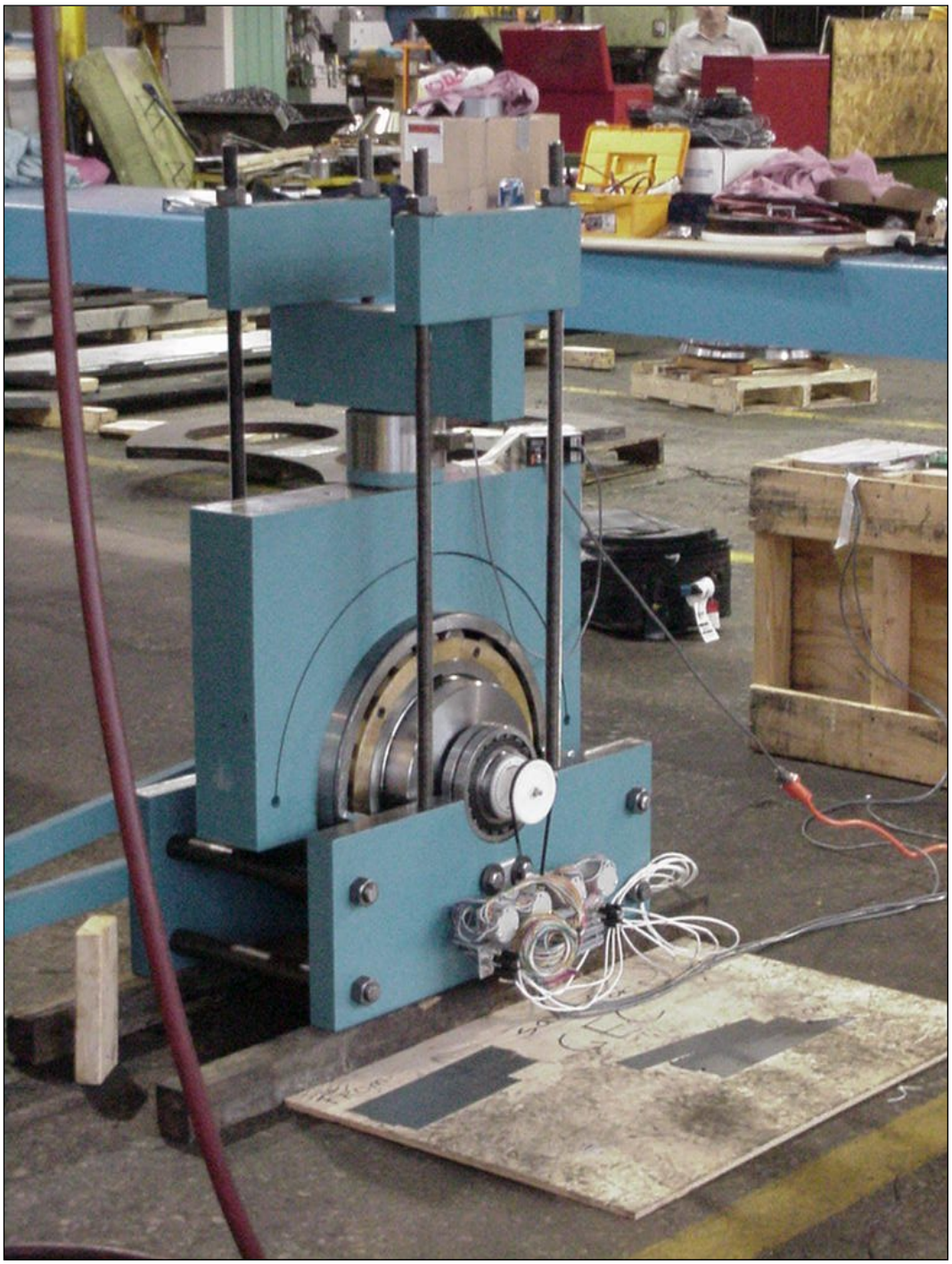

Figure 67. Bearing load calibration fixture (Photo credit: Chris Walford, DNV Renewables Inc.)

The load was applied at staged levels by tightening the threaded tie-rods and measuring at the load cell. While the load was applied, the inner race was rotated approximately 180° to move one roller through the TDC position. The orientation of the inner race was recorded with a rotary potentiometer. Figure 68 shows an example of the measurement taken from the center gage in Slot A (PBL3) for the series of applied loads. Note that, in general, the traces are symmetric, repeatable, and increasing approximately linearly with applied load.

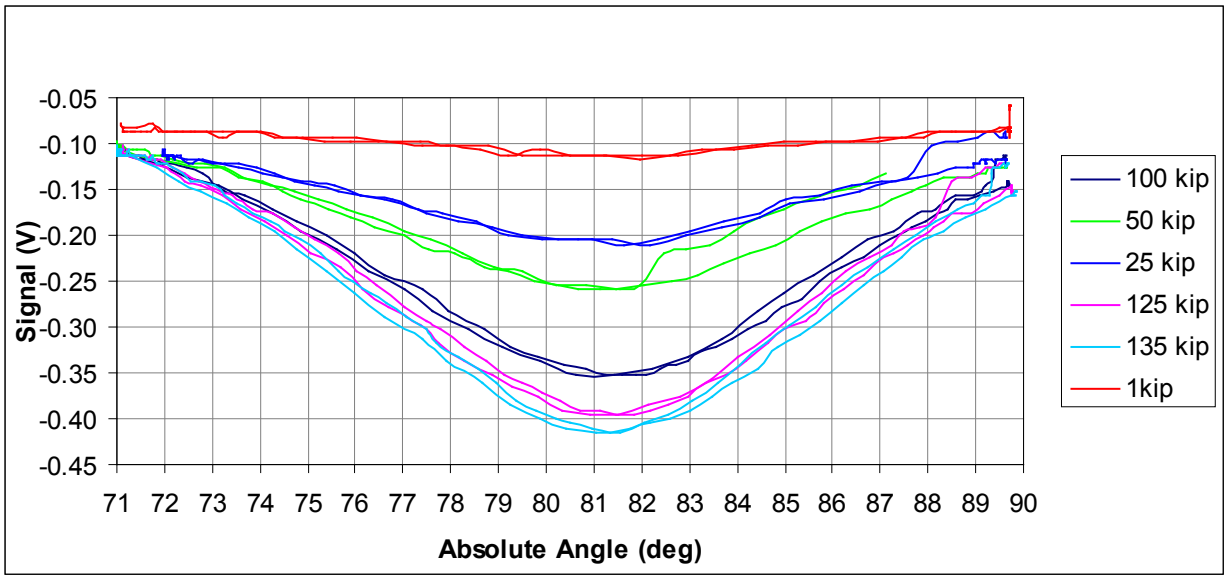

Figure 68. CARB bearing calibration, PBL3 (Slot A)

Note that the calibration procedure only measured the gage response for one roller. This was based on the assumption that because all the rollers would be identical, the response to any single roller would be the same. Unfortunately, upon review of the measurements recorded on the actual test article, it became obvious that this assumption was erroneous. Figure 69 shows a time series recorded with the drivetrain operating at 1,100 kW (approximately two thirds of rated power) for signal PBL2. This is the gage located near the center of Slot A at TDC. The time segment covers the passage of a complete roller set (20 rollers) over the slot. The amplitude is not calibrated to the load, but it has been normalized to the average signal value to remove the signal offset from the strain gage.

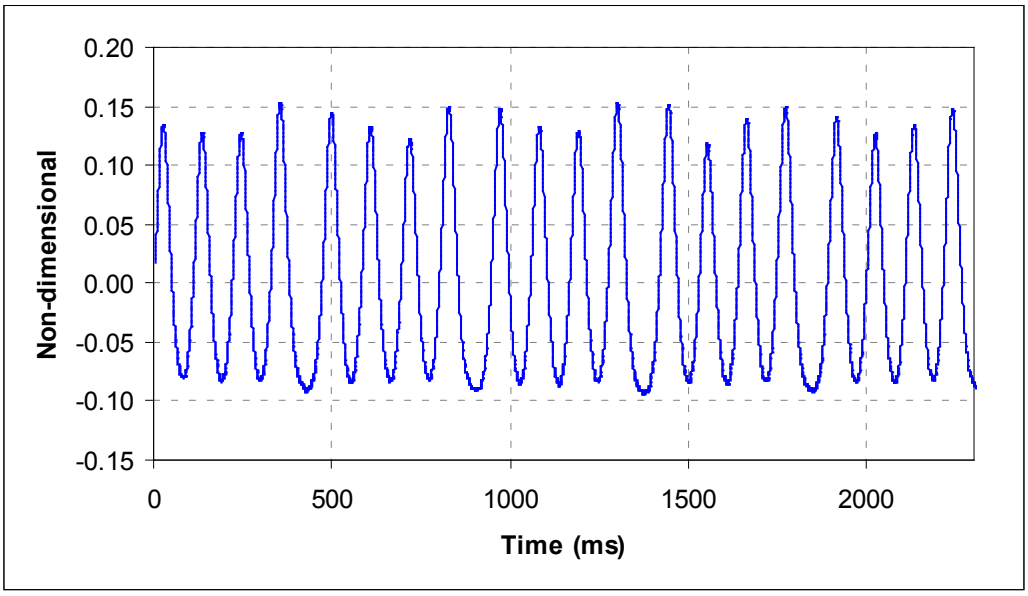

Figure 69. Planet bearing load (PBL2) at 1,100 kW

Note that the signal peaks occur in groups of four equally spaced intervals, repeated five times for the 20-roller cycle. This pattern is due the bearing cage having five structural supports that space the rollers into five groups, as depicted in Figure 65 and visible in Figure 67. As shown in Figure 69, the rollers adjacent to the gap receive greater loading (two adjacent tall peaks) than do the rollers in the middle of the grouping (two lower peaks). Also note that the amplitude varies from roller to roller, as shown in Figure 70 for the next sequential set of signals. This next set is nearly identical to the first set in that the general pattern is repeated but the magnitudes are different. This difference probably is due to slight variations in roller diameter or profile, although this has not been confirmed with physical measurements.

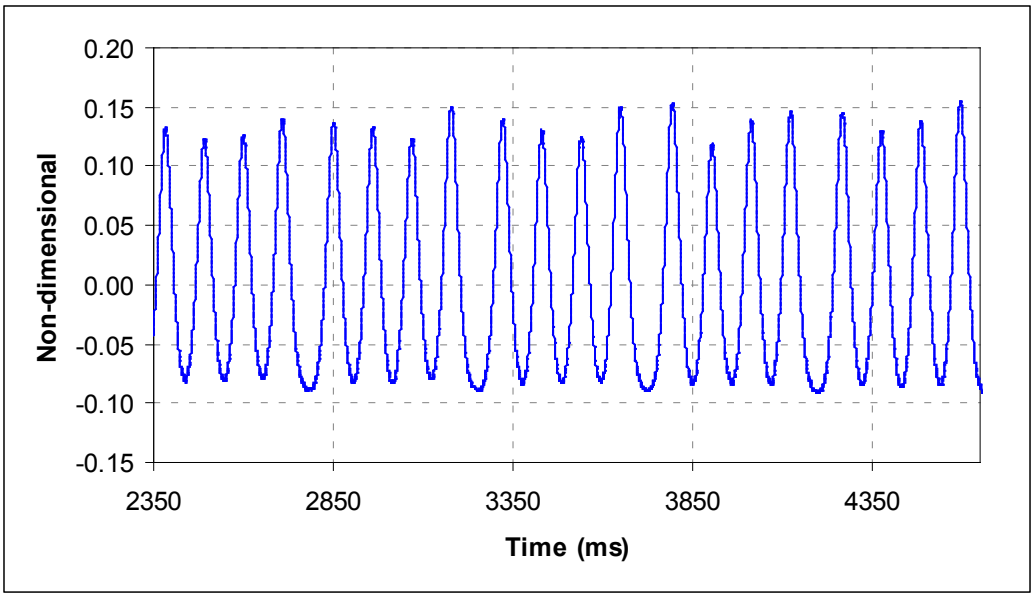

Figure 70. Planet bearing load (PBL2) at 1,100 kW

This variation in signal due to the asymmetrical bearing spacing rendered the calibration effort useless (at least for any degree of accuracy) because it is not possible to assign a specific roller to a specific signal in the sequence. Nevertheless, the data still reveal important information regarding the load distribution among the rollers—and the load distribution along any one roller—as the applied load changes. Figure 71 shows the change in average peak signal with drivetrain power level for the gages at Slot A (located at TDC). The signals for gages PBL1 and PBL5—each located at the outer edge of the slot—have been averaged to remove any offset due to axial misalignment of the inner and outer bearing races. The same rationale applies to PBL2 and PBL4, which are located on either side of the center of the slot. Note that the signals increase approximately linearly with applied load.

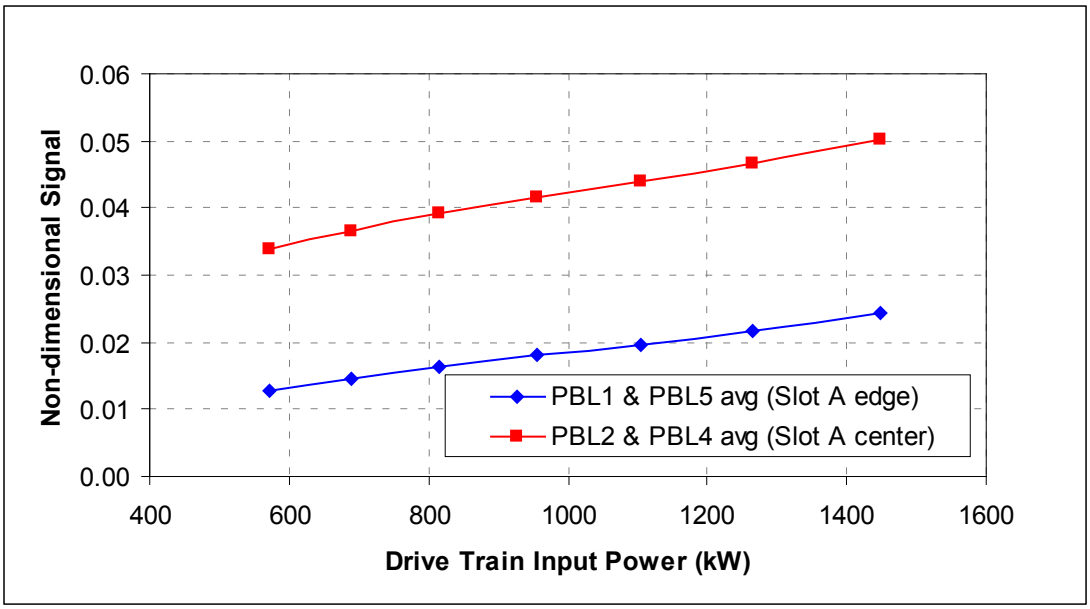

Figure 71. Planet bearing strain gage peak loads at slot A

Figure 72 shows the same data for the gages in Slot B, located at 72° off of TDC. The signals in this slot increase at a faster rate than the do signals in the TDC slot. This shows that the roller load zone spreads out over more rollers as the applied load increases. This phenomenon is seen clearly by examining the ratio of the signals at Slot B to the signals at Slot A, as shown in Figure 73. At the end of the load zone, the load that is borne by the rollers increases dramatically, from 27% to nearly 70% of that of the rollers located at TDC, which bear the greatest load.

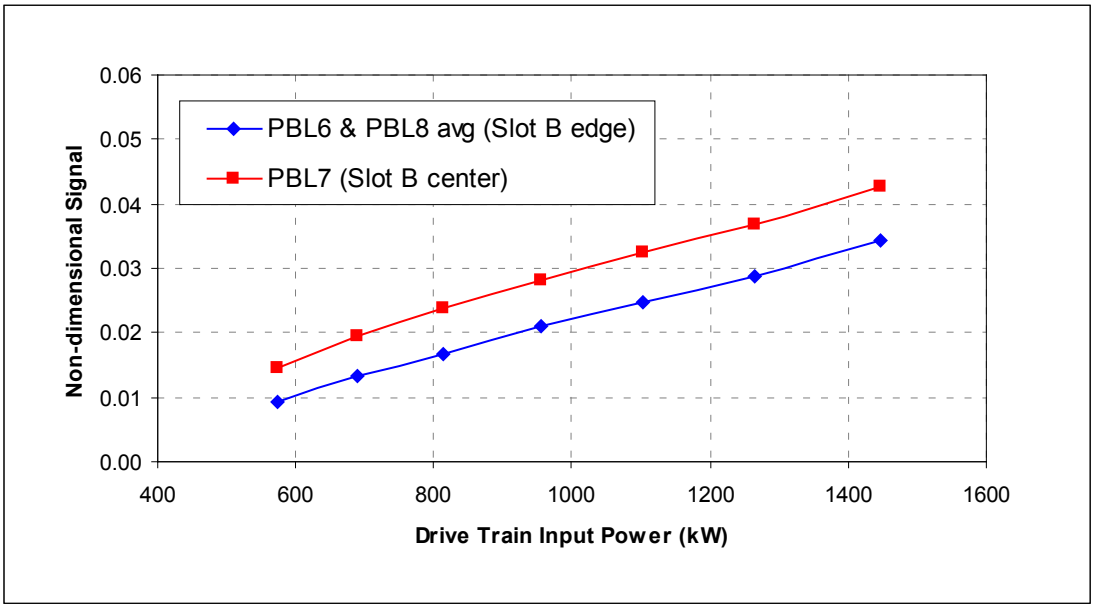

Figure 72. Planet bearing strain gage peak loads at slot B

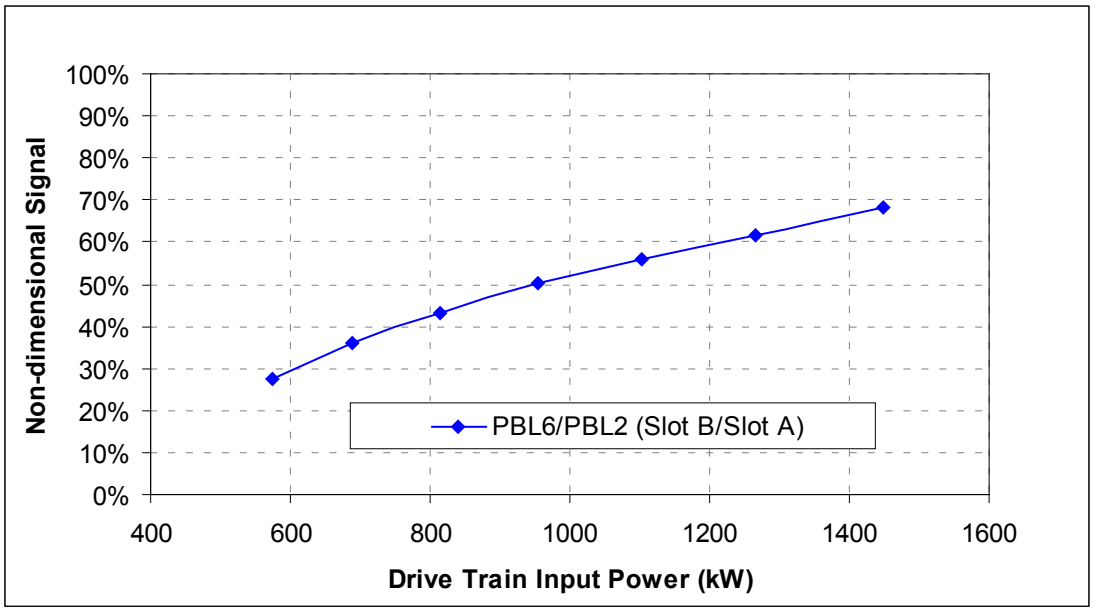

Figure 73. Planet bearing strain gage peak loads, ratio of slot B to slot A

The effect of the roller load zone "spreading out" over more rollers as applied load increases is expected for a roller bearing, but the unique loading of a planet gear greatly increases the effect. The unusual bearing load zone of a gear that is loaded by teeth 180° apart can be seen in Figure 74. The image on the left in Figure 74 shows the theoretical roller load distribution for a bearing that is loaded at one point, as with a parallel-shaft arrangement. The image on the left is derived from a finite-element analysis of the planet gear used in this test article (executed by SKF Industries, the manufacturer of the CARB bearing). The arrows show the relative magnitude of the load on each roller with each type of gear. Note that the load zone for the planet gear is distributed more uniformly and the maximum roller load is less than for the rigid gear. The red arrow indicates the measured relative roller load at a planet load of 516 kN (approx 1,450 kW input power), compared with the predicted roller load for a planet load of 600 kN.

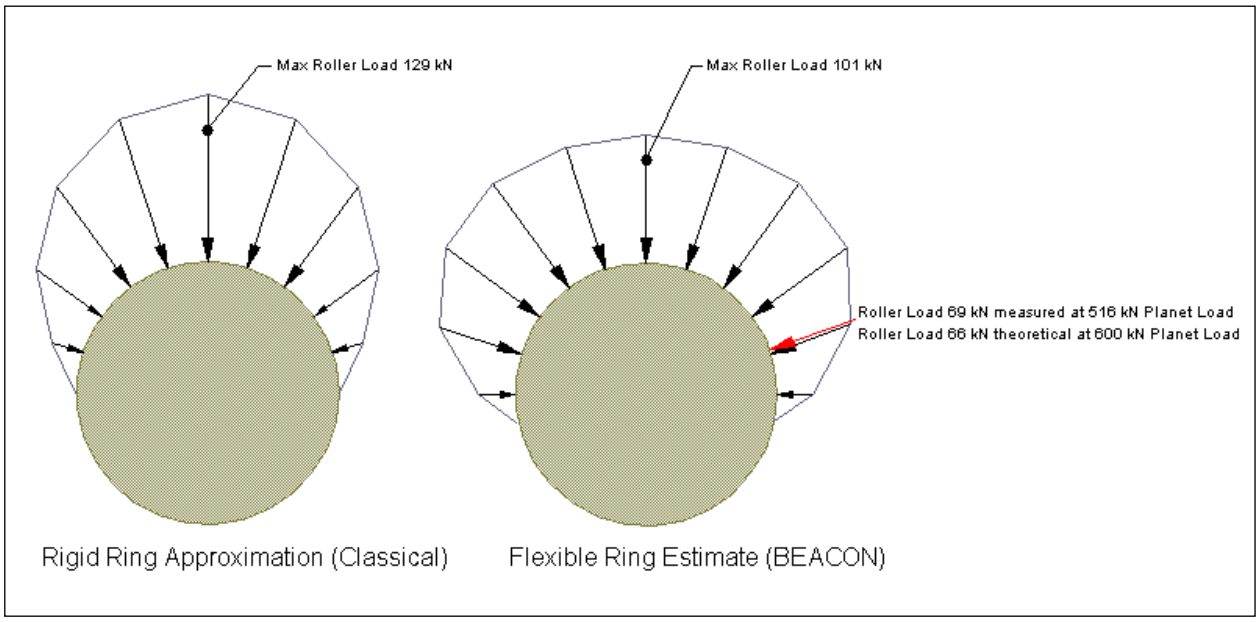

Figure 74. Roller load distribution

Another interesting finding from the planet bearing load data is an estimate of the pressure distribution along the length of the roller. The CARB roller is not a true cylinder; the pressure under very light loads therefore is localized under the middle of the roller. The pressure distribution of heavy loads was expected to spread out over the length of the roller. Figure 75 shows that effect, with the ratio of the signal at the gages toward the edges of the slots to the signals toward the center of the slots. For both Slot A and Slot B this ratio increases with load.

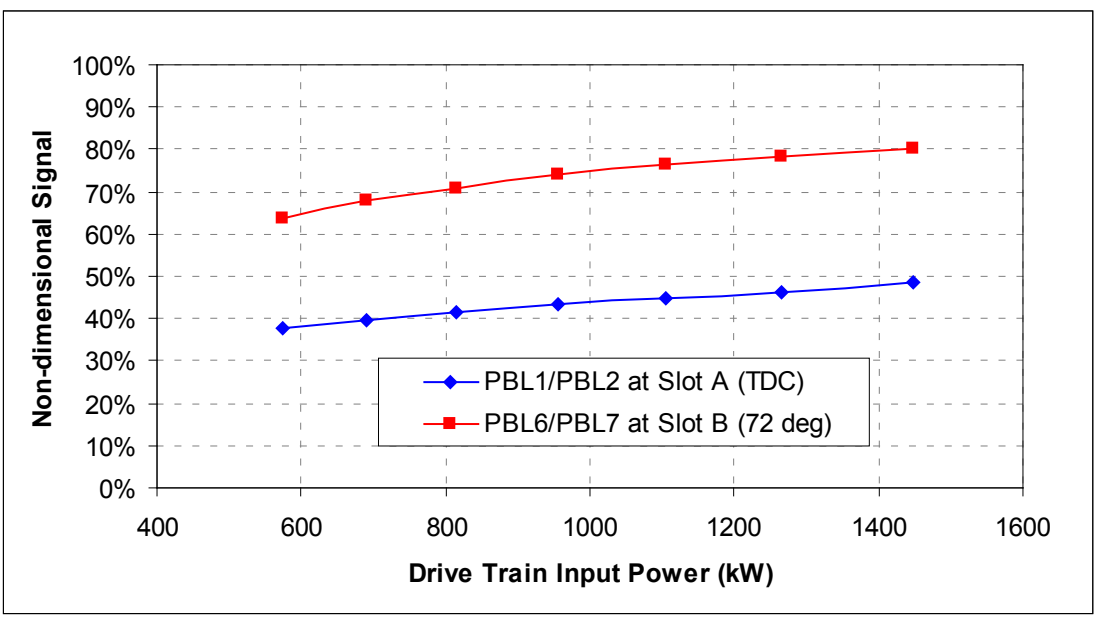

Figure 75. Planet bearing load distribution

5.1.3.6 Magic Roller

One of the planet bearings was instrumented by the manufacturer, SKF Group, using its proprietary "Magic Roller" sensor. Strain gages are installed inside one of the rollers. The gages react to roller load as the roller moves through the active load zone for the bearing. The signal from the gages is conditioned in the rotating frame and then transmitted to a stationary receiver. Figure 76 shows a typical signal from the Magic Roller. Note the periodic variation as the strain gages in the roller are loaded and unloaded at approximately 5 Hz. This signal is modulated by the roller moving through the load zone approximately every two seconds.

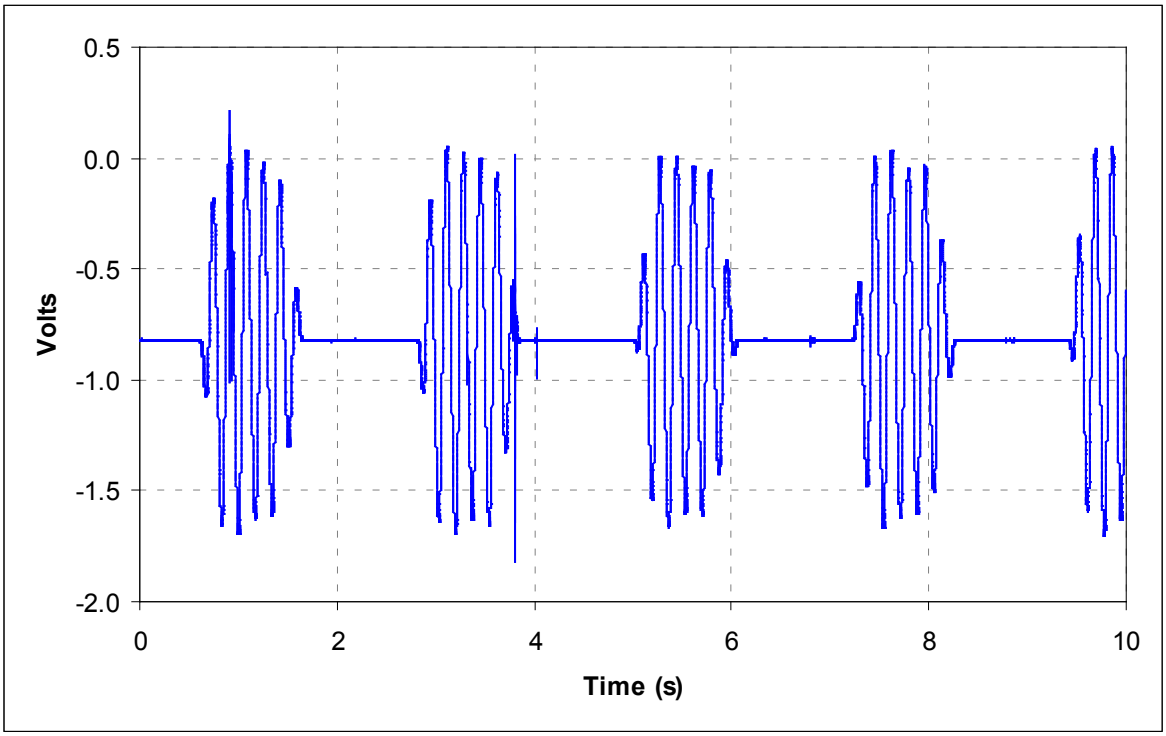

Figure 76. Magic Roller waveform (generator power = 1,457 kW)

The signal from the Magic Roller was processed by SKF to derive the bearing roller load zone for several operating points. Figure 76 shows the measured mean bearing load for operation at 1,457 kW, and 191 rpm. Due to a communication error, the calibration is off by a factor of 2.2. The correct value of 517 kN (235 · 2.2) compares well with the 519 kN theoretical load.[2]

[2] Torque = 1,457 kW · (60/2pi) / (191/9.3) rpm = 677.5 kN-m. With a center distance of 435 mm, the radial load for each planet is 677.2 kN-m / (3 · 0.435) = 519 kN.

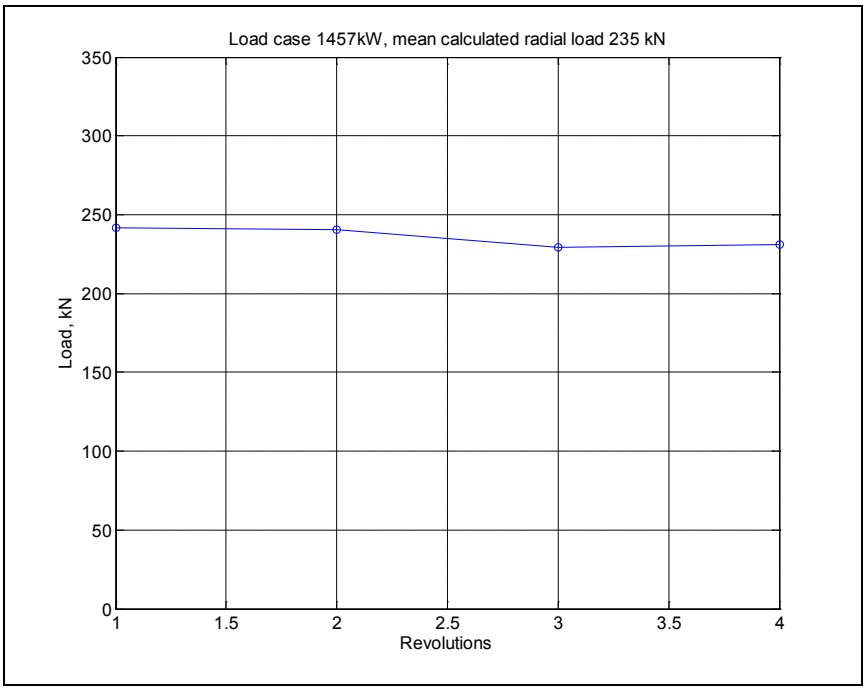

Figure 77. Magic Roller mean load (generator power = 1,457 kW)

Figure 78 shows the measured roller load zone for operation at 1,457 kW. Again, with the scaling corrected by the factor of 2.2, the maximum roller load is 99 kN (note that the SKF source data were not provided to modify charts). The shape of the roller load distribution, indicated by the red line, agrees well with the distribution predicted by finite element analysis in Figure 74 above.

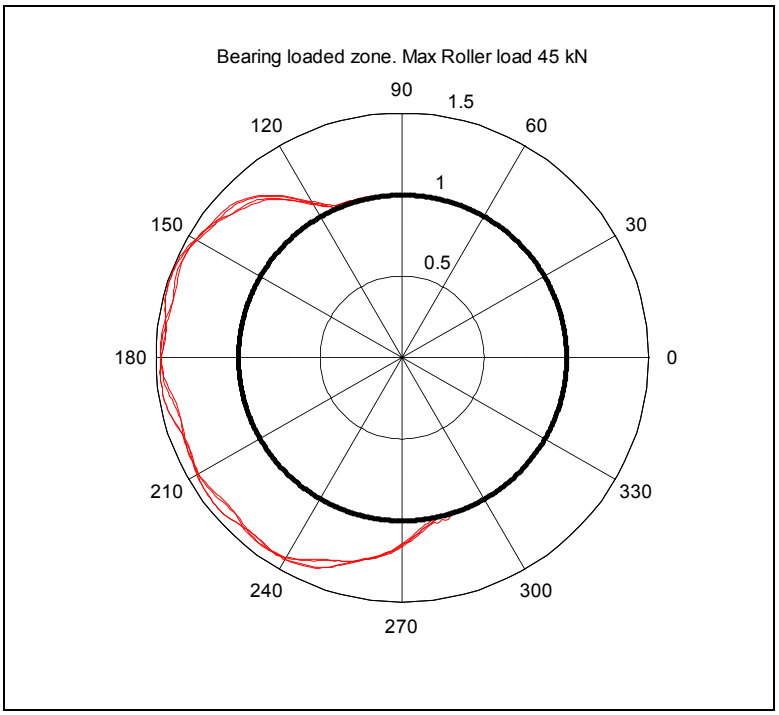

Figure 78. Magic Roller load zone (generator power = 1,457 kW)

5.1.3.7 Transient Response

The transient response of the drivetrain was tested by commanding step changes in power to the inverters while the dynamometer was operating in constant-speed mode. Figure 79 and Figure 80 show the torque response of the drivetrain when coupled to the dynamometer. A quantitative analysis of the transient response has not been performed because of the difficulty in separating the response of the drivetrain from the response of dynamometer.

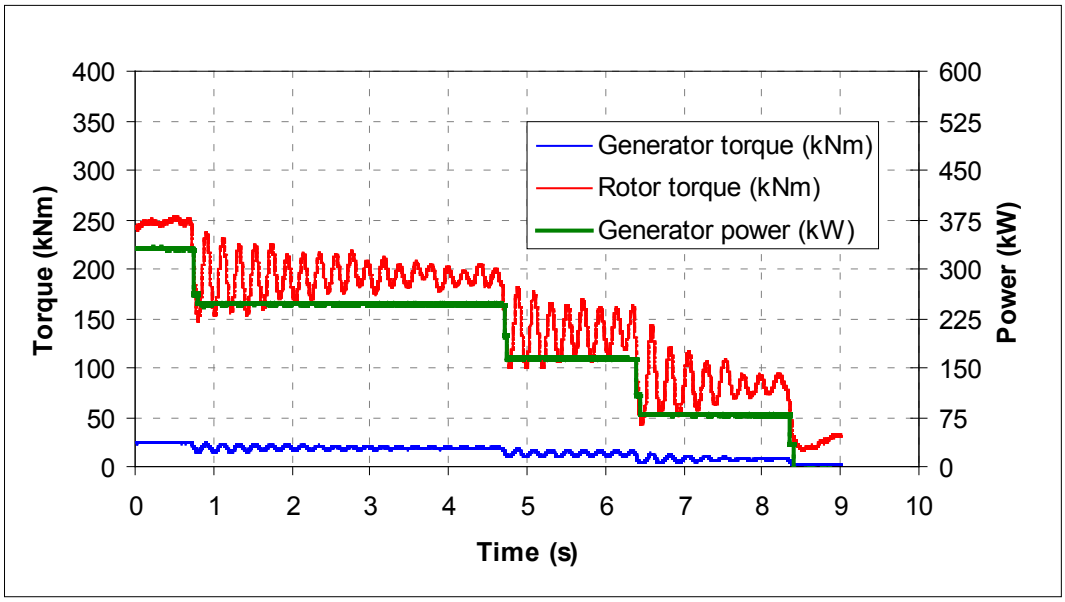

Figure 79. Torque response run #1 (rotor speed = 15.5 rpm)

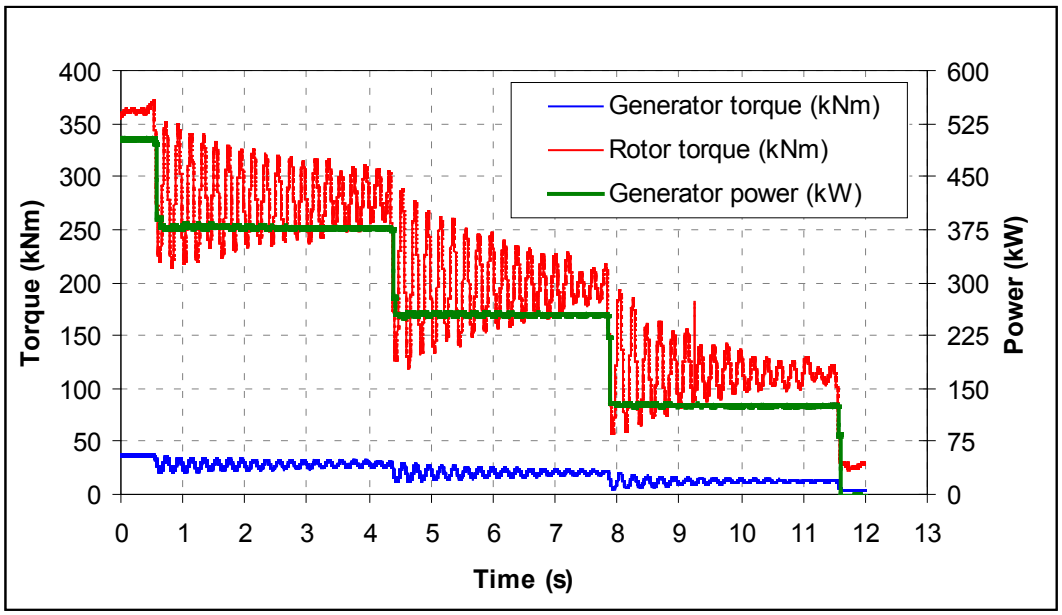

Figure 80. Torque response run #2 (rotor speed = 15.5 rpm)

5.2 Thermal Performance

5.2.1 Gearbox Fluid Cooling System

Throughout the testing of the drivetrain, the temperature of the gearbox lubricant remained significantly below the maximum allowable temperature of 80°C. For a majority of the duration of generator testing, the radiator fan of the gearbox fluid cooling system was never turned on. During the testing shown in Figure 81, the radiator fan was not turned on until approximately 1:30 p.m., when the lubrication temperature reached 59°C. This is the maximum temperature attained by the lubrication throughout all of the drivetrain testing. With the fan on, the lubrication temperature dropped sharply. Due to the great efficiency of the gearbox, the demand on the gearbox fluid cooling system was small. The heat loss in the gearbox was evacuated effectively by the cooling system. For the test run shown in Figure 81, the average lubrication supply pressure is 22.5 psi and average lube flow rate is 79.7 liters per minute.

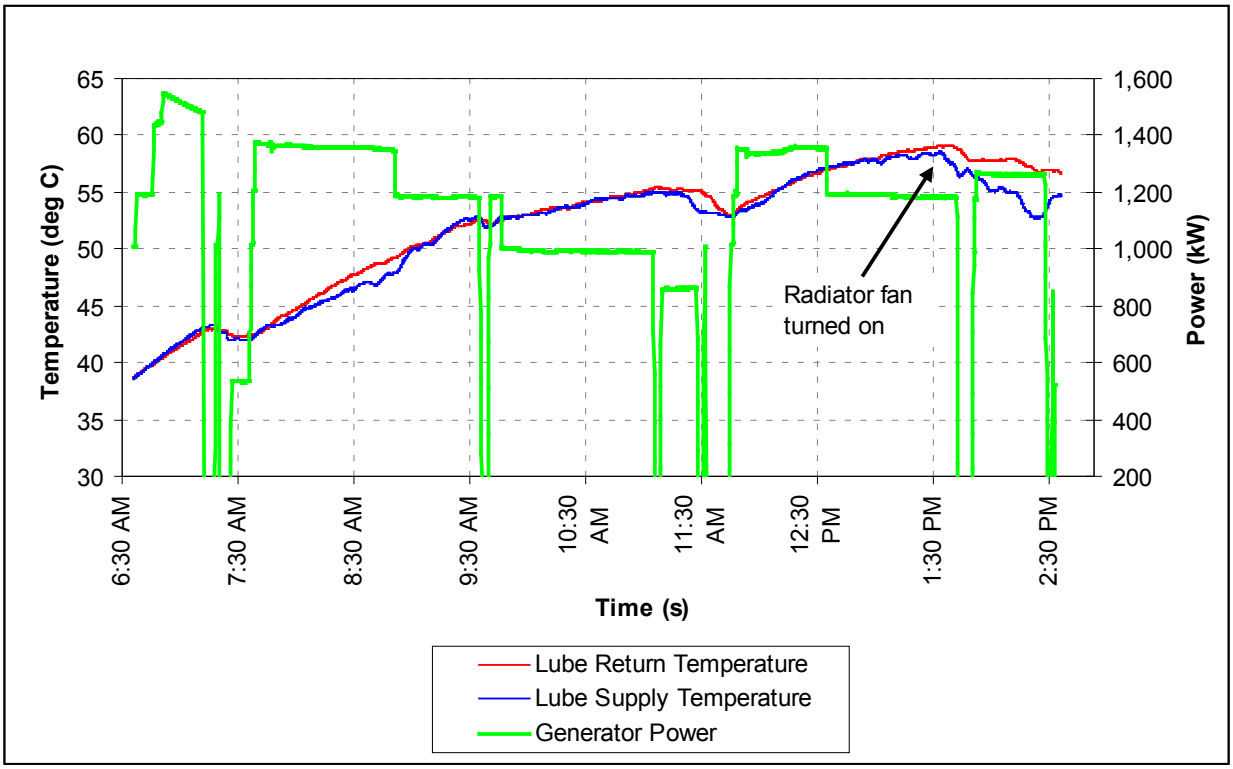

Figure 81. Gearbox lubrication system temperature

5.2.2 Generator Stator Fluid Cooling System

Although very few thermal performance data were gathered for the parallel winding configuration, enough data exist to compare the winding temperatures of the parallel configuration to those of the series configuration at two power levels. Figure 82 and Figure 83 compare the average winding temperatures at 600 kW and 700 kW, respectively, for the parallel and series winding configurations. The winding temperatures in Figure 82 and Figure 83 were measured at the outside of the winding end-turn for both the parallel and series winding configurations. Thermistors were used to measure winding temperature in the parallel configuration, and RTDs were used in the series configuration.

There is a significant difference between the temperatures of the parallel and series winding configurations. In the 600-kW test runs (Figure 82), the series winding and parallel winding temperatures are increasing slightly. The rate of change in temperature for both winding configurations is 0.03°C/min over the 45-minute set of data presented. The series winding temperature is more than 20°C hotter than the parallel winding temperature. Although the ambient interior temperature of the DTF is not available for both test runs, the ambient outside temperature for both test runs was near 30°C.

In the 700-kW test runs shown in Figure 83, the parallel winding temperature increases slightly and the series winding temperature decreases slightly. Both temperatures, however, appear to be approaching steady-state. The rate of change of the parallel winding temperature is 0.03°C/min and the rate of change of the series winding temperature is -0.02°C/min. It is unlikely that the 35°C gap between the winding temperatures would decrease by more than 5°C to 10°C. This leaves a discrepancy of at least 25°C to 30°C. As noted above, the ambient interior temperature of the DTF is unavailable; however, the ambient outside air temperature during the parallel winding test run was approximately 5°C hotter than during the series winding test run. It is likely that the winding temperature discrepancy in Figure 83 would be even greater if the ambient temperature was the same for both of the test runs. The cause of the great discrepancy between the temperatures of series and parallel windings is unknown. The magnitude of the discrepancy points to a design flaw in the series windings.

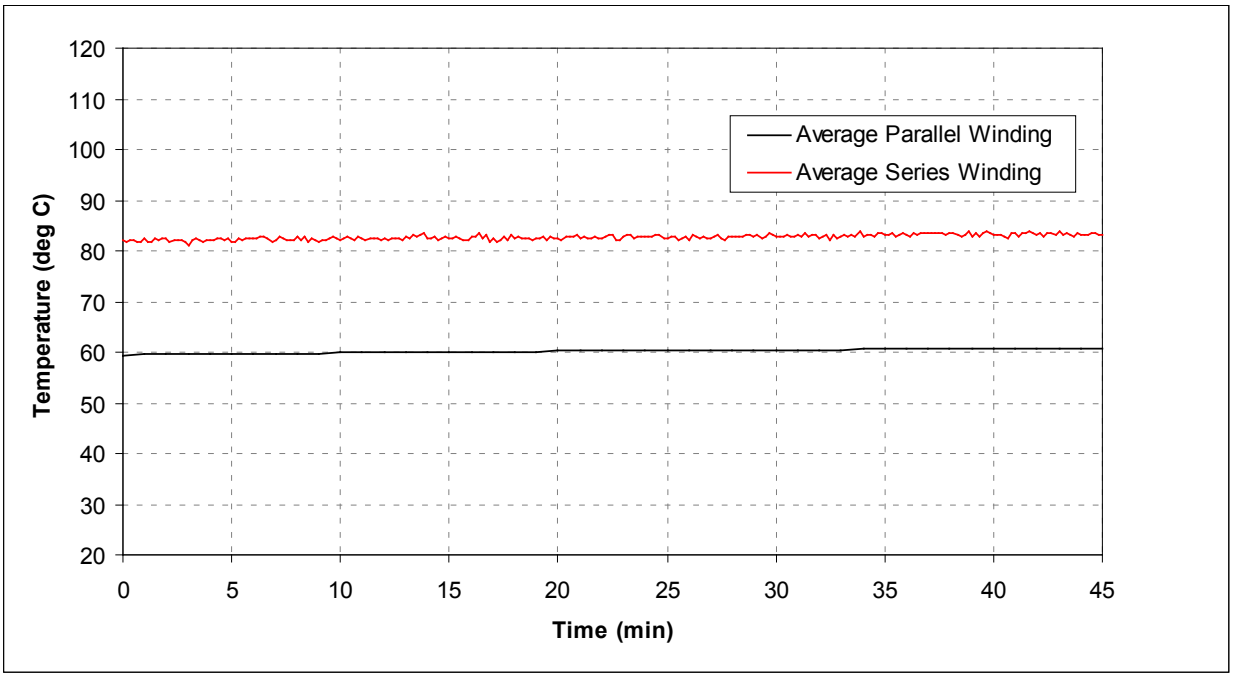

Figure 82. Winding temperature comparison at 600 kW

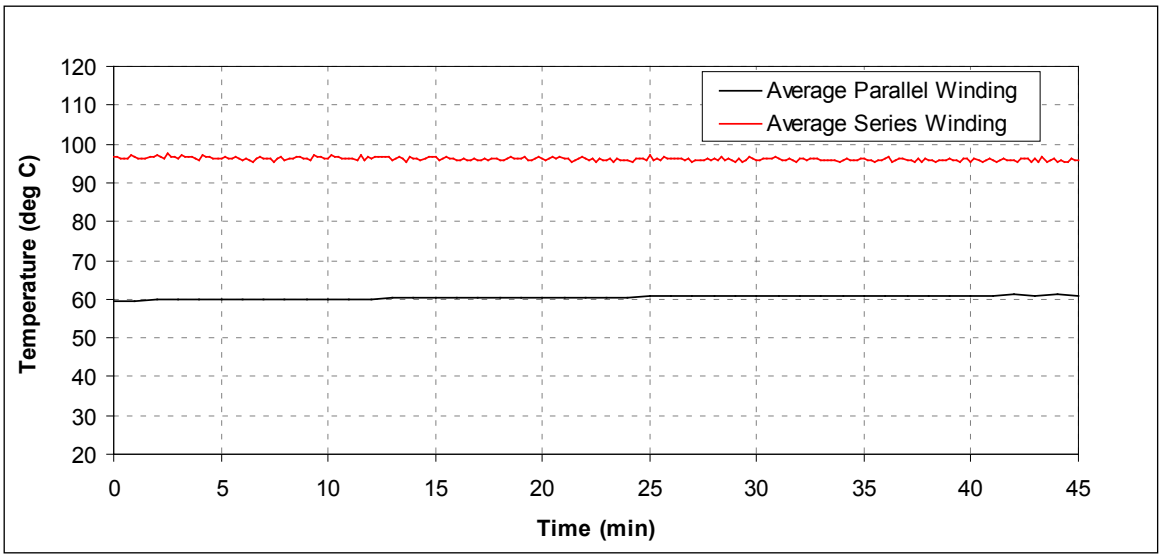

Figure 83. Winding temperature comparison at 700 kW

Although the drivetrain was able to operate at rated power for brief periods, 1.0 MW was the greatest power level at which the winding temperatures of the generator stabilized below the design limits. Figure 84 is a plot of the temperature of the inside of the winding end-turn, and the temperature of coolant supply and return. Throughout the testing of the drivetrain, the temperature inside the winding end-turn was significantly hotter than any of the other measured stator temperatures. At 1.0 MW, the winding temperatures stabilized at slightly less than the 165°C design limit, and the coolant temperatures stabilized well below the 100°C limit.

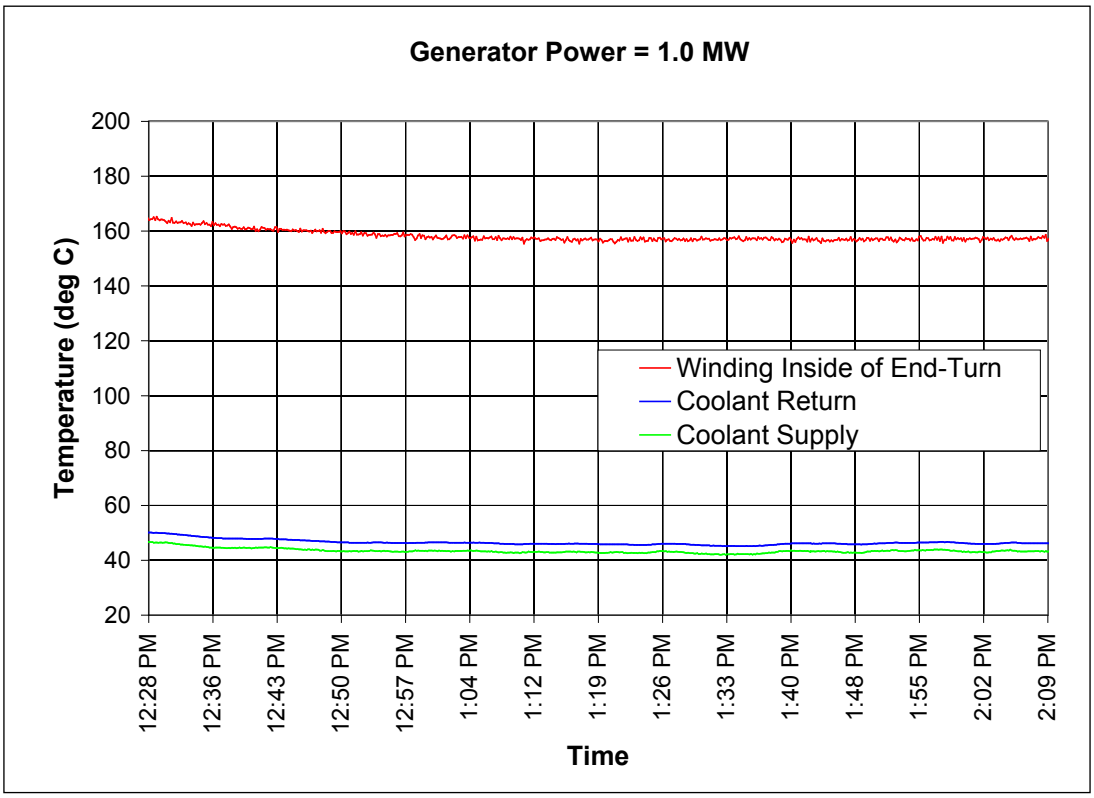

Figure 84. Temperature run at 1.0 MW

At 1.2 MW, the winding end-turn inside temperature exceeds the 165°C limit, as shown in Figure 85. Although the generator temperatures were beginning to stabilize in the test run shown in Figure 85, the test was halted to prevent damaging the windings and magnets. As shown in Figure 84, the coolant temperatures were hotter in the 1.0-MW test run than in the 1.2-MW test run, because the ambient temperature of the DTF was significantly greater. At 1.2 MW, the coolant temperatures still are significantly less than the design limits.

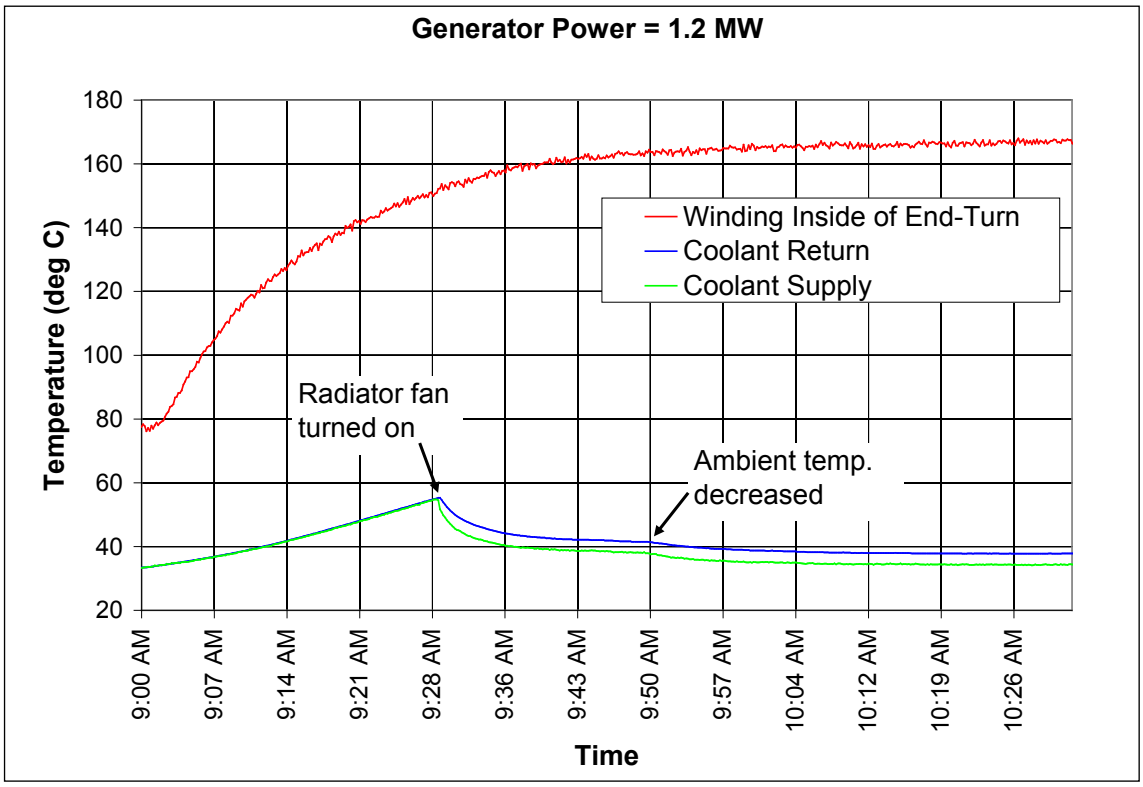

Figure 85. Temperature run at 1.2 MW

At rated power, the winding temperature exceeds the design limit within a few minutes. The rated power test run shown in Figure 86 was performed prior to the installation of RTDs at several locations on the stator. Only the outside of the winding end-turn temperature was measured during this rated power run. Based on experimentation, the outside of the end-turn typically was 20°C cooler than the inside of the end-turn. The windings therefore probably exceeded the design limit when the temperature outside of the end-turn reached approximately 145°C. Although the windings are significantly overheated at the end of this rated power run, the coolant temperatures are nearly 50°C less than the design limit.

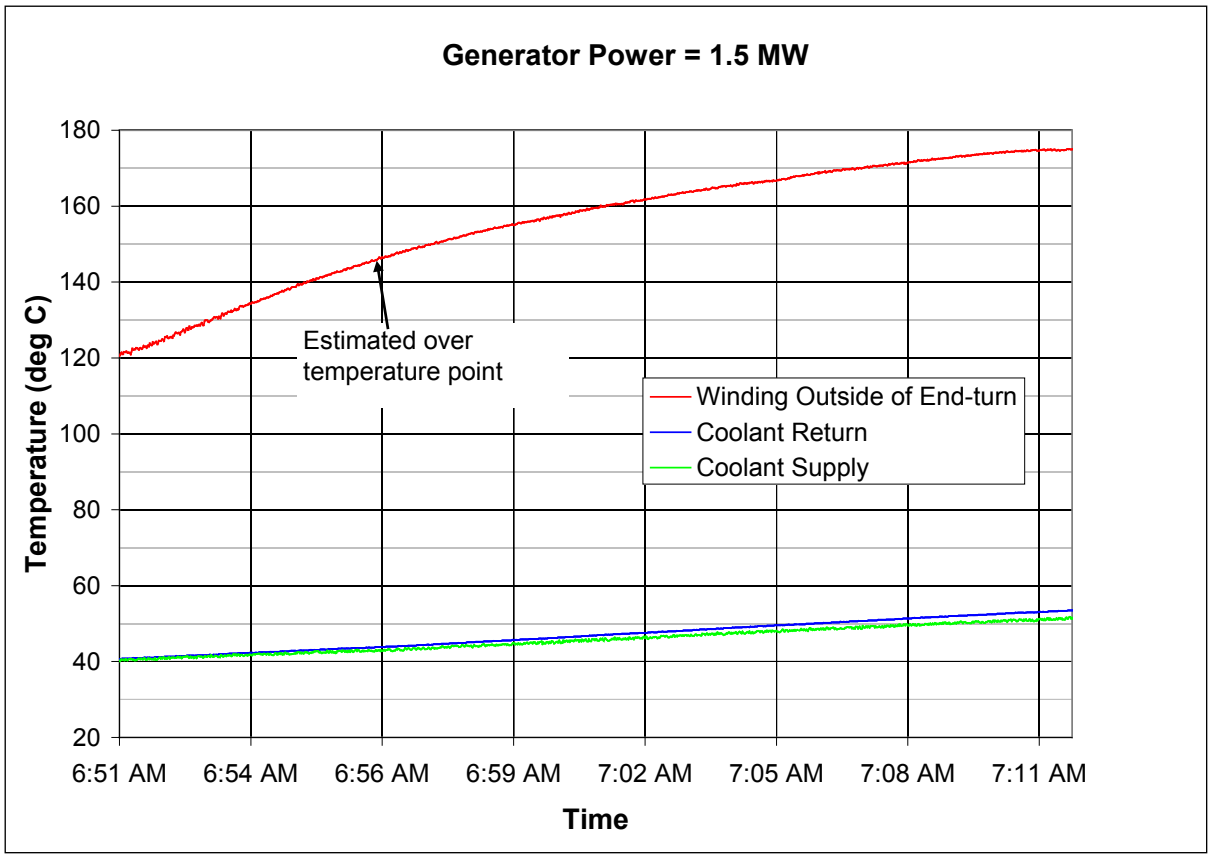

Figure 86. Temperature run at 1.5 MW

The primary impetus for measuring temperatures at several stator locations was to determine what caused the stator windings to overheat when the coolant temperatures were relatively low. The designed flow of heat from the stator windings to the coolant fluid (Glycol) is shown in Figure 87. The heat of the stator windings is conducted through the core and back iron to the cold plate and then from the cold plate to the Glycol. The maximum design temperature of the windings is 165°C at rated power. The designed temperature drop from the windings to the cold plate is 85°C, which results in a maximum cold plate temperature of 80°C. The sets of RTDs installed on the stator enabled verification of each of the temperature drops shown in Figure 87.

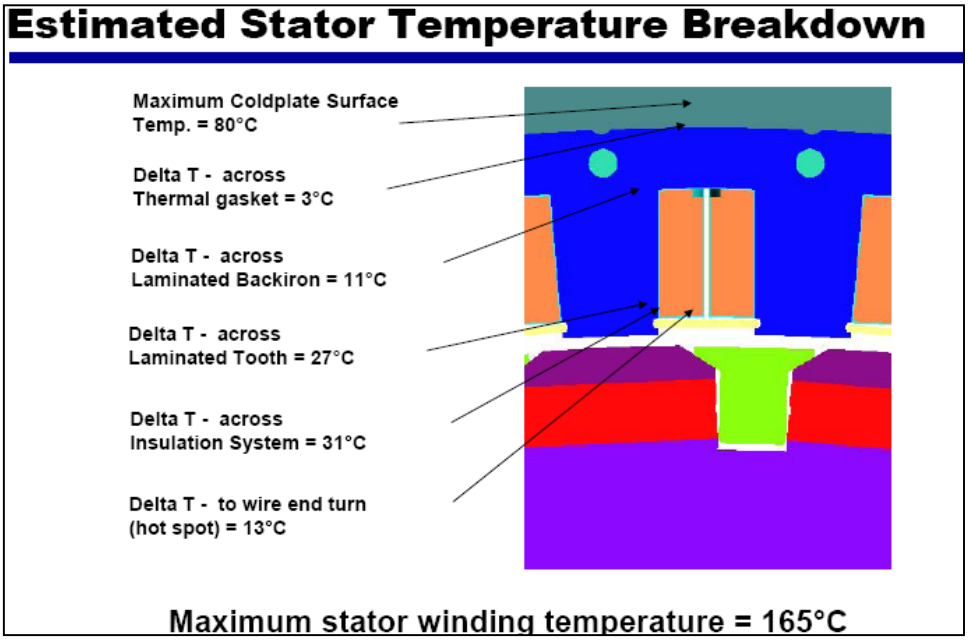

Figure 87. Design stator temperature breakdown

The greatest power level for which the drivetrain was able to reach thermal equilibrium was 1.0 MW. At levels greater than 1.0 MW, the winding and magnet temperatures approached or exceeded the design limits. The temperature data in Figure 88, Figure 89, Figure 90, and Figure 91 were gathered after thermal equilibrium was reached for a 1.0-MW test run. Figure 88 is a plot of the measured stator temperatures at 1.0 MW. The segment temperatures are relatively consistent, indicating an even thermal distribution around the stator.

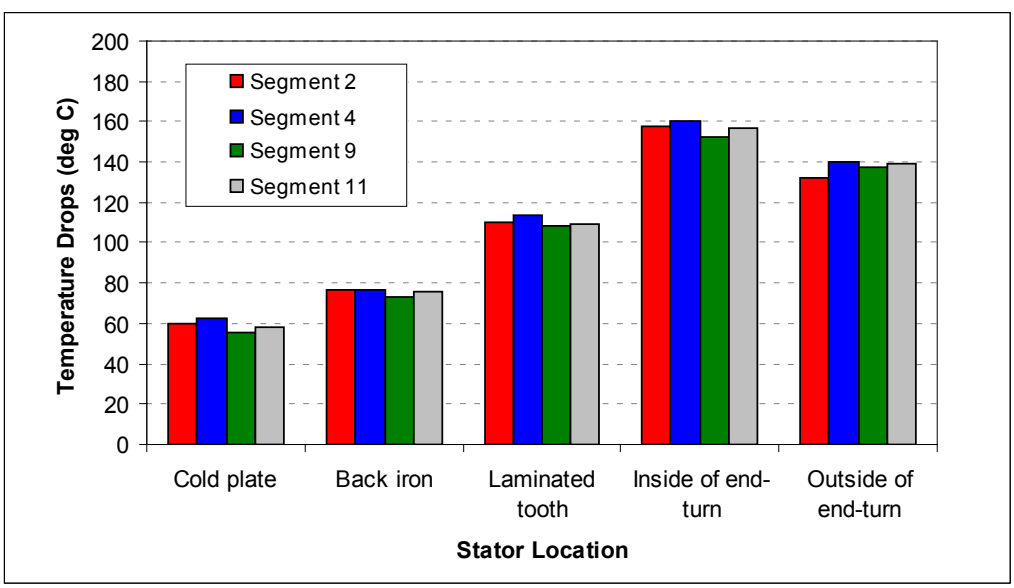

Figure 88. Stator temperature breakdown at 1.0 MW

Figure 89 is a plot of the measured stator temperatures at 1.0 MW averaged over the four segments, as well as the design stator temperatures at 1.5 MW. At 1.0 MW, the average temperature inside of the winding end-turn and the laminate tooth temperatures both were within 7°C of the rated-power design values. The conduction losses in the stator windings were proportional to the square of the current, therefore the conduction loss at 1.5 MW is approximately 225% of the loss at 1.0 MW. The 7°C margin between the measured design values at 1.0 MW and 1.5 MW is not sufficient to accommodate increased loss at 1.5 MW.

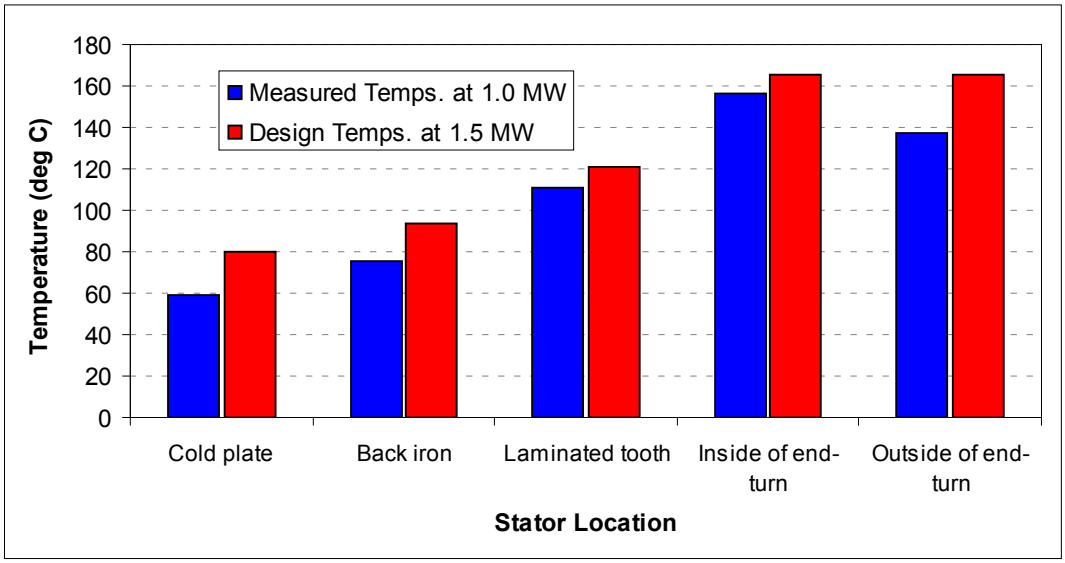

Figure 89. Stator temperature comparison

Figure 90 shows the measured temperature differentials between various elements of the stator. The temperature differentials are consistent across the four generator segments, indicating even heat flow from the windings to the coolant system.

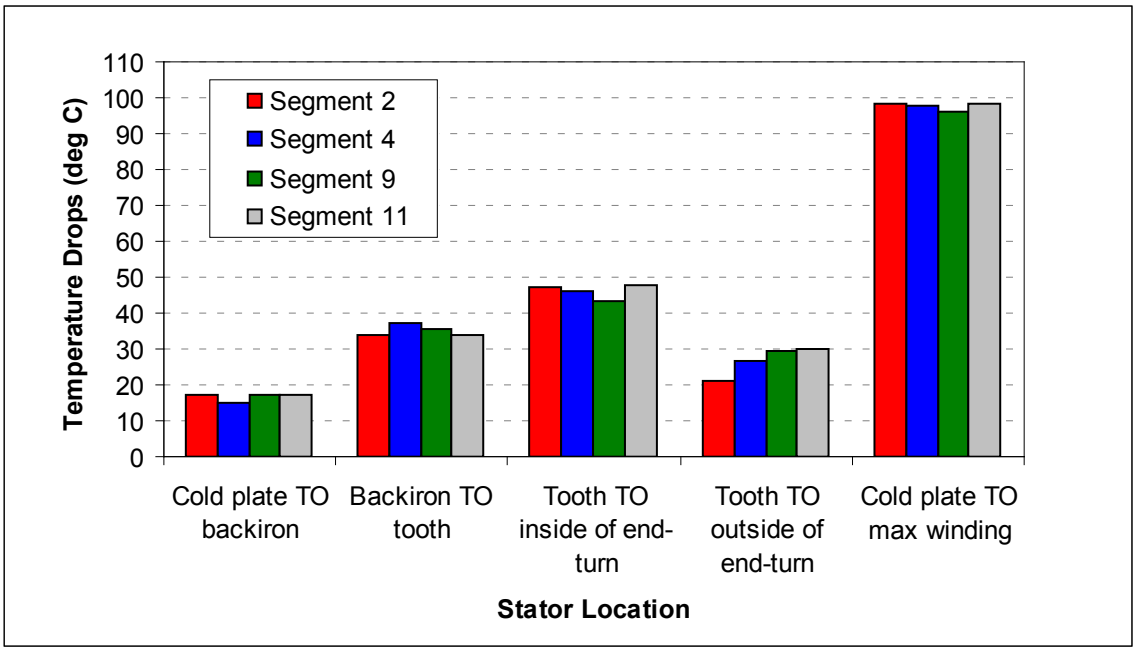

Figure 90. Stator temperature drops at 1.0 MW

Figure 91 contains the measured stator temperature differentials at 1.0 MW averaged over the four segments, as well as the design stator temperature differentials at 1.5 MW.

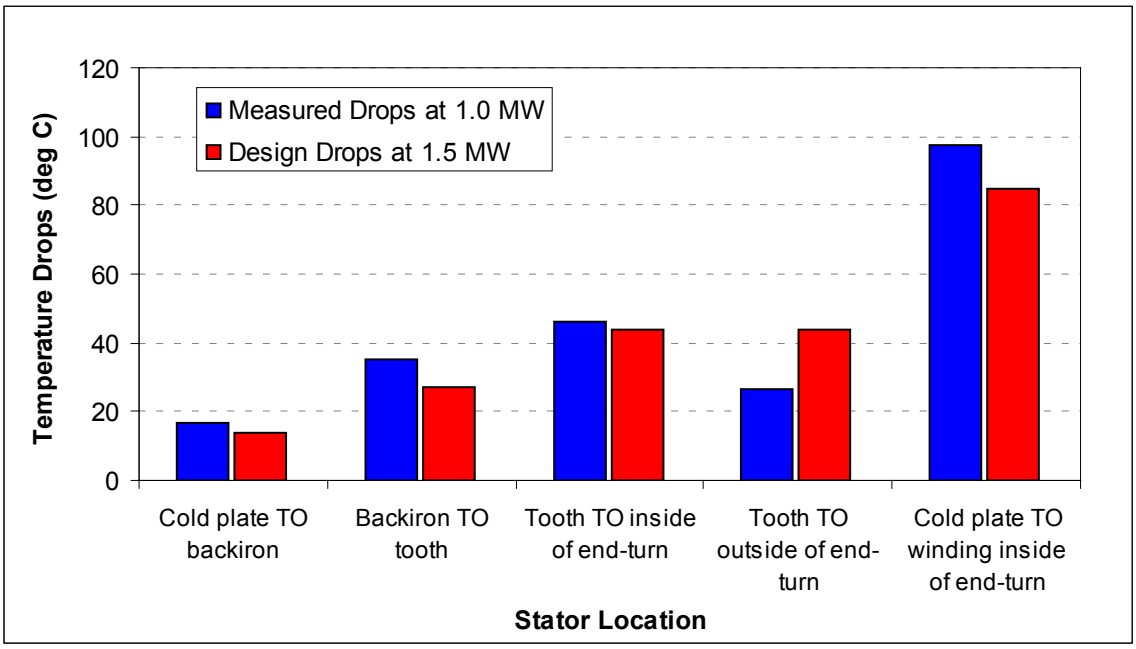

Figure 91. Stator temperature drop comparison

The two potential causes of the overheating of the generator when running at power levels greater than 1.0 MW are the greater than expected losses in the generator, and the greater than expected thermal resistance between the windings and the cold plate. The cold plate and generator coolant temperatures remained low throughout testing. It therefore is unlikely that the

elevated temperatures resulted from an undersized cooling system. The winding temperatures increased dramatically from the parallel winding configuration to the series winding configuration, therefore a greater than expected loss in the windings seems to be the most probable cause of the poor thermal performance.

5.2.3 Generator Rotor Air / Water Cooling System

As described, the temperature of the magnets was measured using temperature probes and thermal imaging, and calculated based on the open-circuit voltage of the generator. Figure 92 is a plot of the magnet temperature calculated based on the open-circuit voltage after select test runs. Thermal equilibrium was not reached in the test runs shown in Figure 92. Although the performance of the magnets is hindered by increased temperature, the degradation of the performance temporarily is less than the specific temperature threshold. The magnets suffer permanent degradation at temperatures that are greater than 100°C to 110°C. During testing the magnet temperatures approached this temperature limit. The most likely cause of the high magnet temperatures was the high winding temperatures.

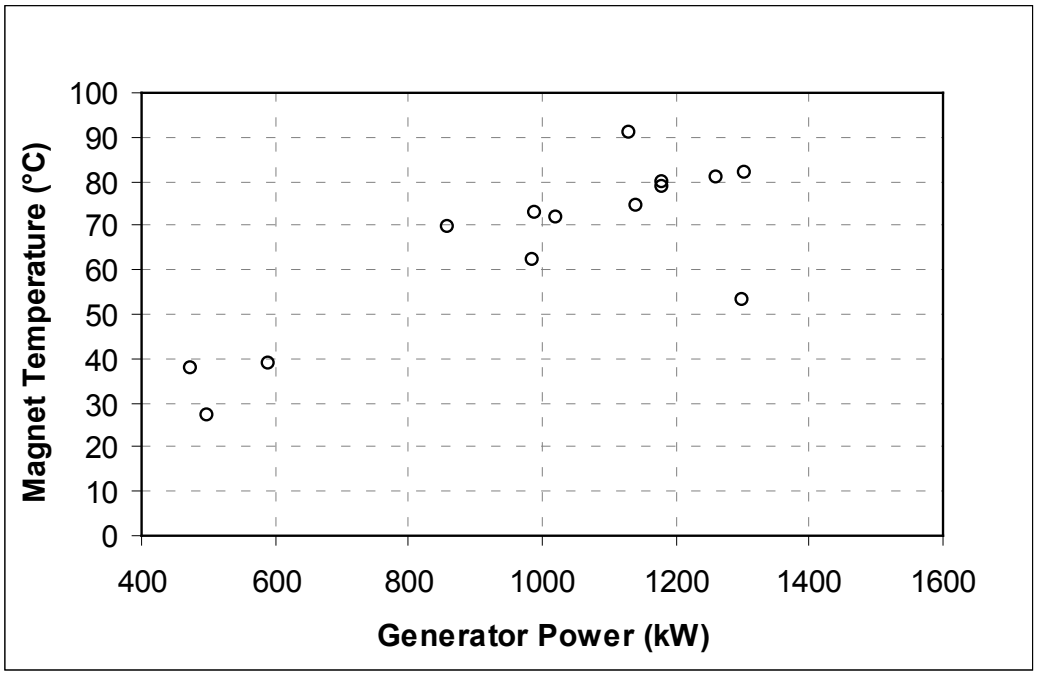

Figure 92. Magnet temperature

5.3 Efficiency

The efficiency of the drivetrain was measured using both the input-output method and the calorimetric method. The efficiency plots in this section show the efficiency predicted during the design and the efficiency measured during testing. It also includes design efficiency values that were adjusted based on the elevated current measured during testing. The intent of including the adjusted design values is to illustrate the theoretical impact of the elevated current and to validate the measured efficiencies.

5.3.1 Input-Output Method

The input-output efficiency was calculated using measurements from the torque spool of the dynamometer, and using the electrical power measurements at the terminals of the generator and the connection point to the grid. Figure 93 is a plot of the combined gearbox and generator efficiency broken down by day. The efficiency values in this plot were calculated using the dynamometer low-speed shaft torque and speed measurement, and the electrical power measurement at the output of the generator. The data in Figure 93 are from four days of testing (August 7–10, 2007). The temperature dependence of the generator voltage causes the efficiency of the drivetrain to vary slightly, depending on the operating conditions. The extreme daily variability shown in Figure 93, however, points to malfunctioning measurement equipment. The data in Figure 93 for 400 kW show a variation in efficiency of 91% on August 10 and 98% on August 7. These results indicate that the accuracy and precision of the input and output power measurements are insufficient to perform efficiency calculations. The low-speed torque measurement likely is the greatest source of error or uncertainty in the efficiency calculations.

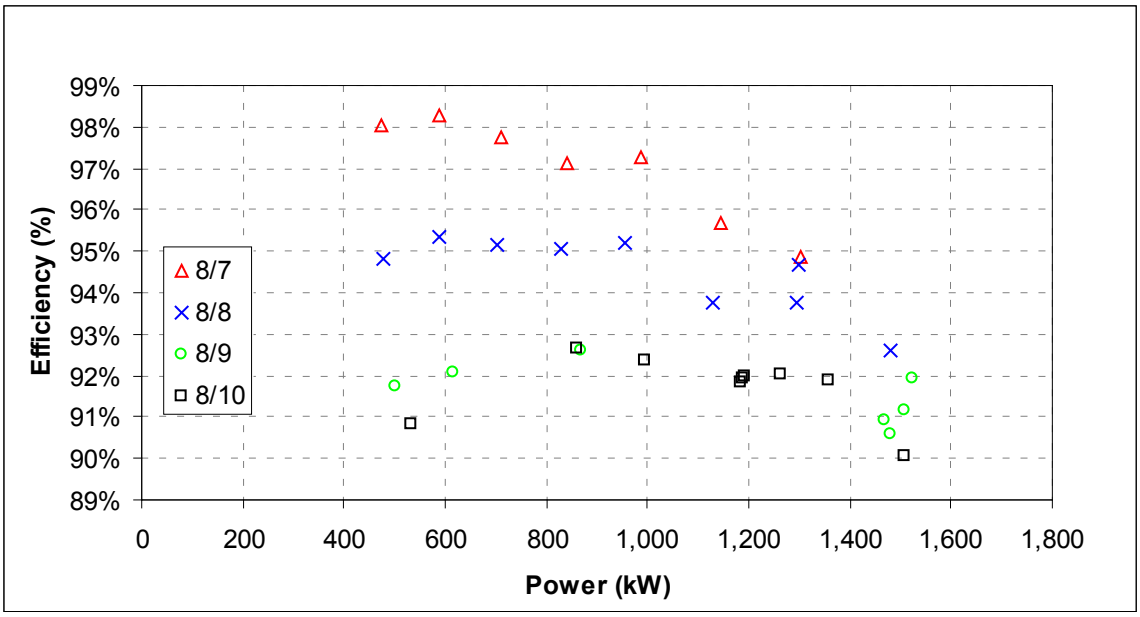

Figure 93. Combined gearbox and generator input-output efficiency by day

Figure 94 is a plot of the combined gearbox and generator input-output efficiency for the test runs when the drivetrain approached or achieved thermal equilibrium. Adjustment of the design efficiency calculations to include the measured current decreases the generator efficiency by almost 0.5% above 1.0 MW. It is difficult to evaluate the performance of the drivetrain prototype based on the data in Figure 94 because of the variability in efficiency (shown in Figure 93).

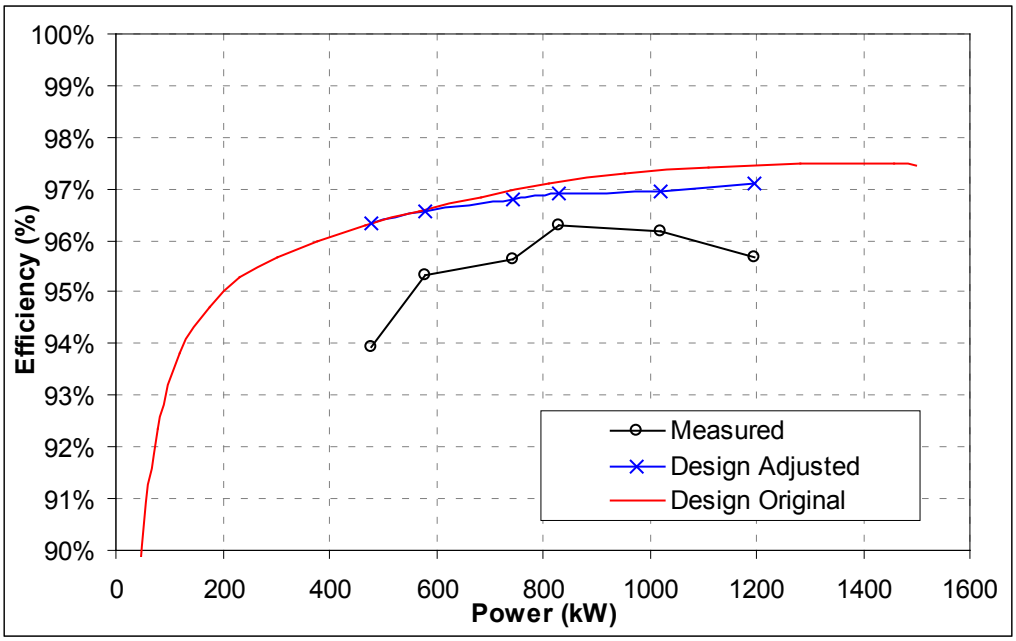

Figure 94. Combined gearbox and generator input-output efficiency

Figure 95 is a plot of the input-output efficiency of the power electronics and transformers for the test runs when the drivetrain approached or achieved thermal equilibrium.

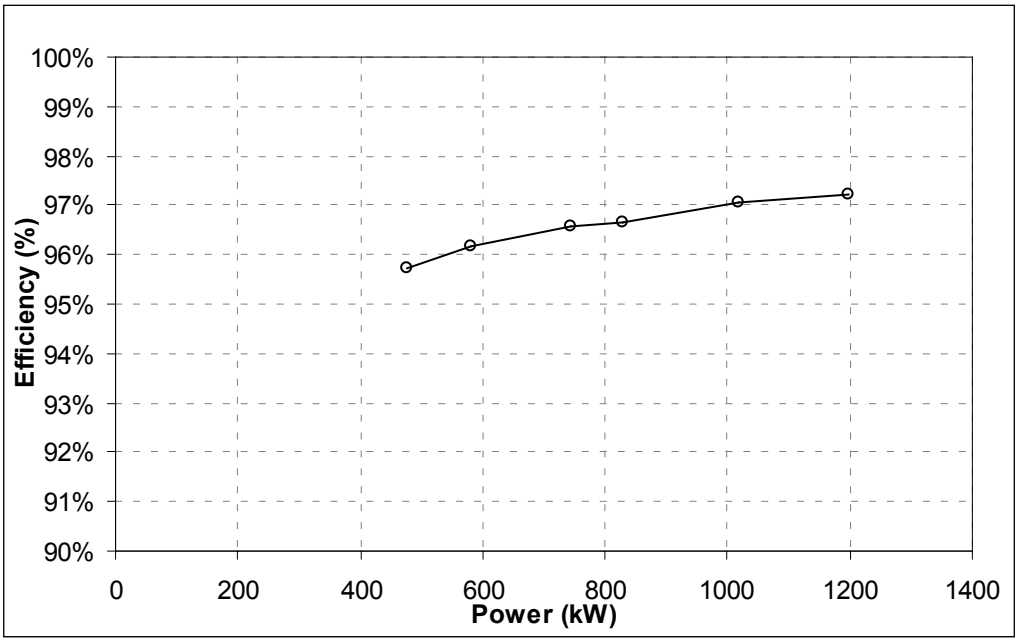

Figure 95. Power electronics and transformer input-output efficiency

5.3.2 Calorimetric Method

The calorimetric efficiency was calculated by estimating the following losses.

- Heat flux of the drivetrain case
- Conduction through the drivetrain stand
- Conduction through the gearbox lubrication system and generator coolant system

The heat flux of the drivetrain case was calculated using measurements taken from a thin-film heat-flux sensor, thermal imaging, and point temperature measurements. A heat-flux sensor was attached to the top of the drivetrain case, near the connection point between the generator and gearbox. Thermal imaging was used to estimate the average temperature of the gearbox and the drivetrain. The average temperature of the gearbox and generator was used in conjunction with the point heat-flux measurement and ambient temperature of the DTF to estimate the heat flux of the gearbox and generator cases. Figure 96 is an example of a thermal image of the drivetrain.

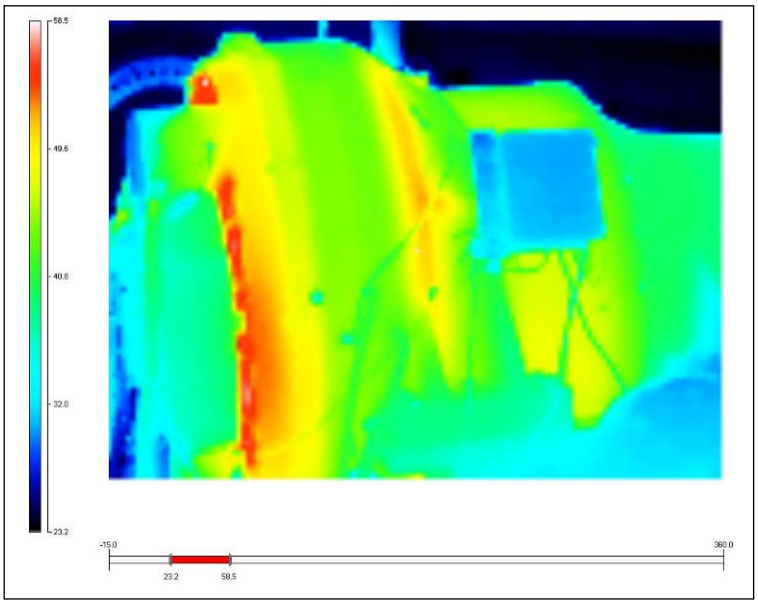

Figure 96. Thermal image example

The conduction of heat through the drivetrain stand was estimated by using thermal imaging to determine the temperature drop across the torque arms of the stand. The geometry of the arms was used in conjunction with the temperature measurements to estimate the heat flux in the stand. Calculations indicated that only a small fraction of the drivetrain's loss was conducted through the stand.

DNV calculated the conduction of the gearbox lubrication system and generator coolant system using the fluid supply and return temperatures and flow rate. The difference in the supply and return gearbox oil temperatures was between approximately 0°C and 1°C. The accuracy of the gearbox oil temperature measurements was insufficient to determine the temperature drop in the gearbox-oil coolant system. Because the loss calculations produced erroneous results, the heat loss in the gearbox-lubrication system was ignored in the final calculations.

It is difficult to separate the gearbox and generator heat loss because of the thermal coupling present. Figure 97, Figure 98, and Figure 99 provide plots of the measured and theoretical

efficiency of the gearbox, generator, and the entire drivetrain. The maximum power level for which the generator was able to operate at thermal equilibrium with stator and magnet temperature at less than the design values was 1.0 MW. Calorimetric efficiency calculations, however, were performed for a 1.2-MW test run. A 1.2-MW test run was performed and, as the drivetrain approached thermal equilibrium, the thermal design limits of the drivetrain were exceeded slightly. Due to the high stator temperatures, this test run was stopped before thermal equilibrium was reached. Prematurely stopping the 1.2-MW test run should've yielded greater-than-actual calorimetric efficiency.

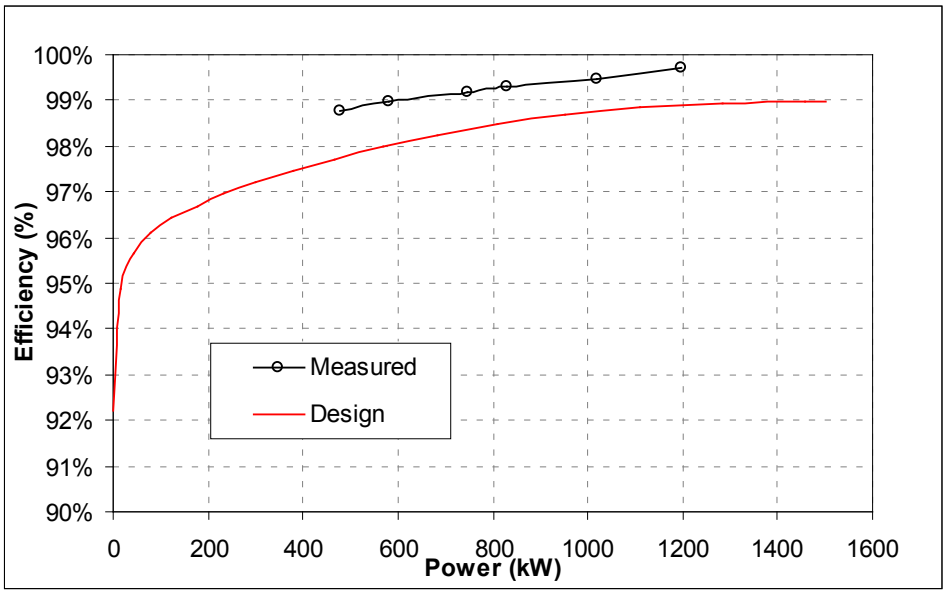

Figure 97. Gearbox calorimetric efficiency

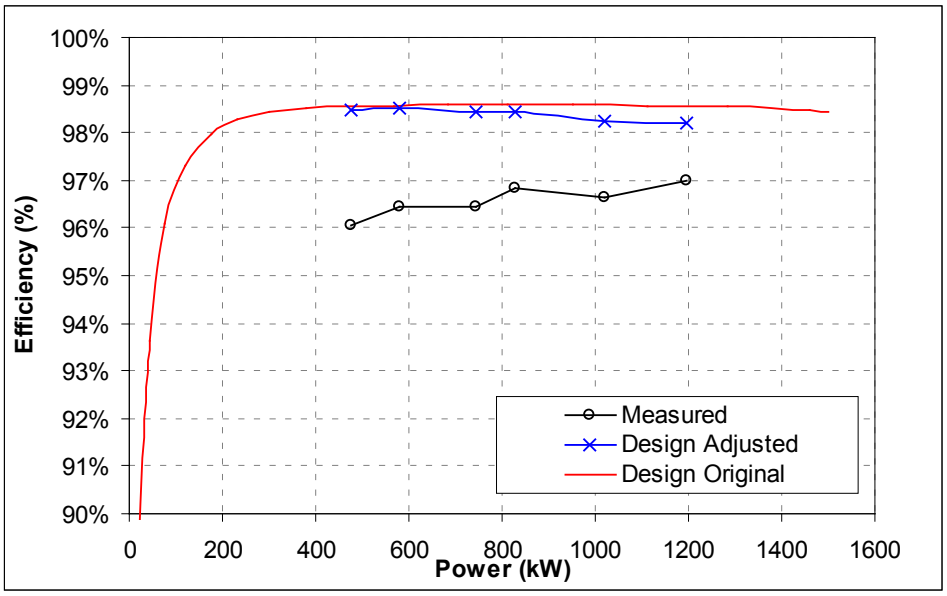

Figure 98. Generator calorimetric efficiency

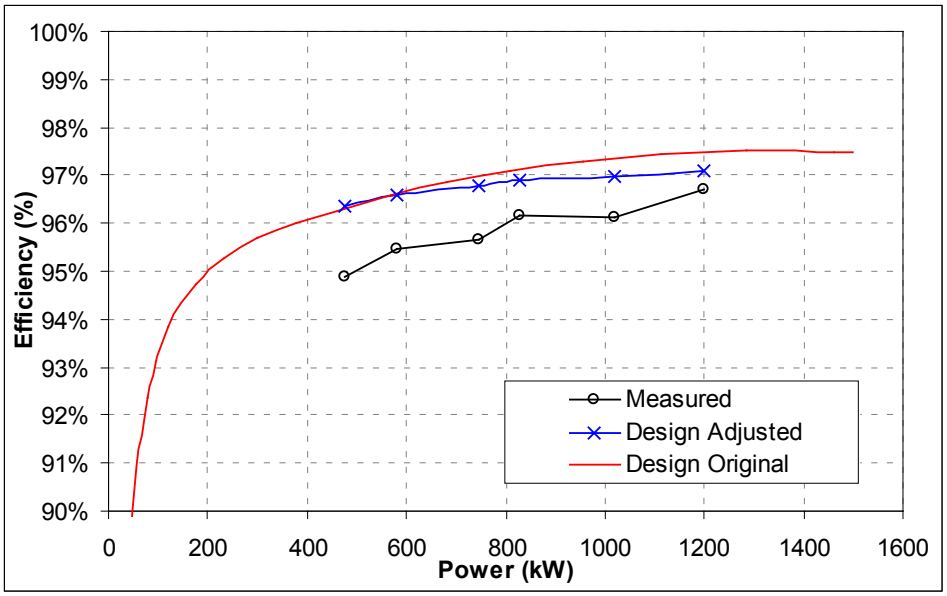

Figure 99. Combined gearbox and generator calorimetric efficiency

5.4 Vibration Levels

The vibration was measured in three orthogonal directions on the east and west side of the generator (see Figure 7 for accelerometer locations). Figure 100 and Figure 101 are representative frequency spectrum plots of the vibration of the drivetrain at the east and west accelerometers at one third rated power. These spectra are dominated by the even harmonics of the electrical frequency and by the gearbox meshing frequency fundamental and second harmonic. The electrical frequency at one third rated power is 53 Hz and the gearbox meshing frequency is 319 Hz. The gearbox meshing frequency fundamental and second harmonics are circled in red in the frequency plots. The spectra of the western accelerometer contain frequency content not present at the eastern accelerometer, especially in the Y and Z directions. During testing, the lubrication pump was mounted on the west side of the drivetrain; this could be responsible for the additional spectral content.

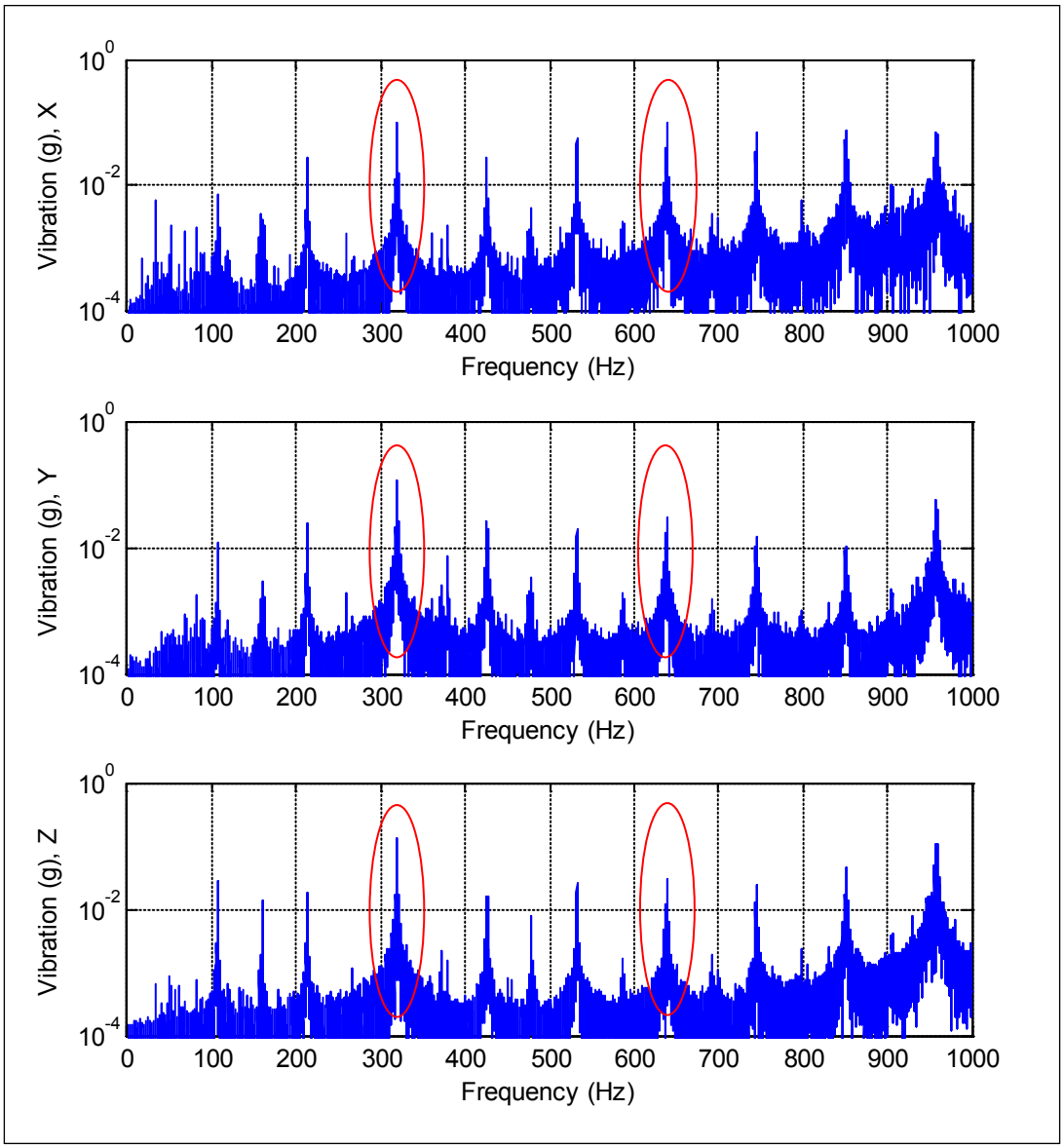

Figure 100. Velocity at one third rated power, east

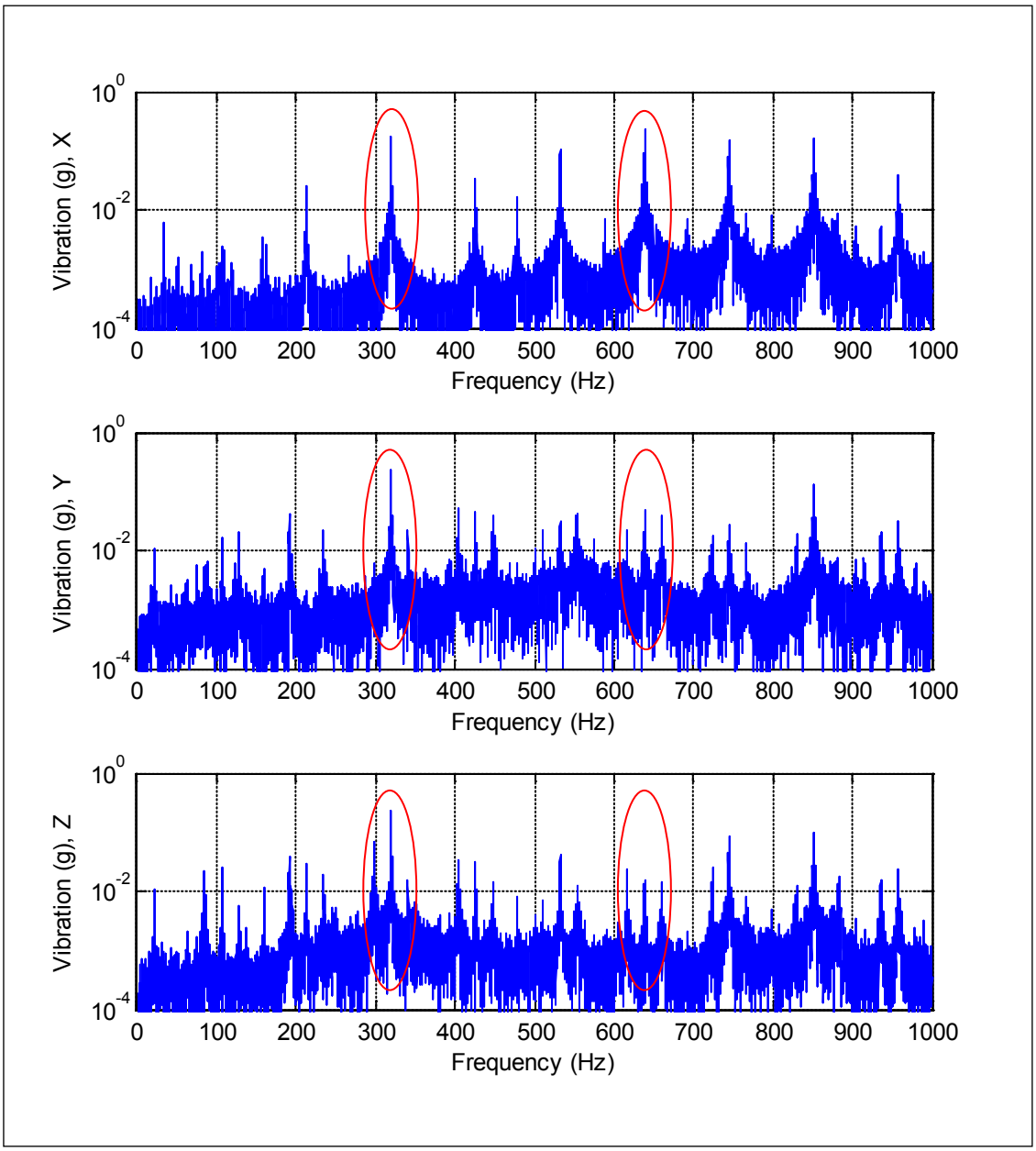

Figure 101. Vibration at one third rated power, west

Figure 102 and Figure 103 are representative frequency spectrum plots of the drivetrain vibration at the east and west accelerometers at rated power. The spectra are dominated by the fundamental and second harmonic of the meshing frequency of the gearbox—458 Hz and 917 Hz, respectively, at rated power. The electrical frequency harmonics present at one third rated power are significantly attenuated at rated power.

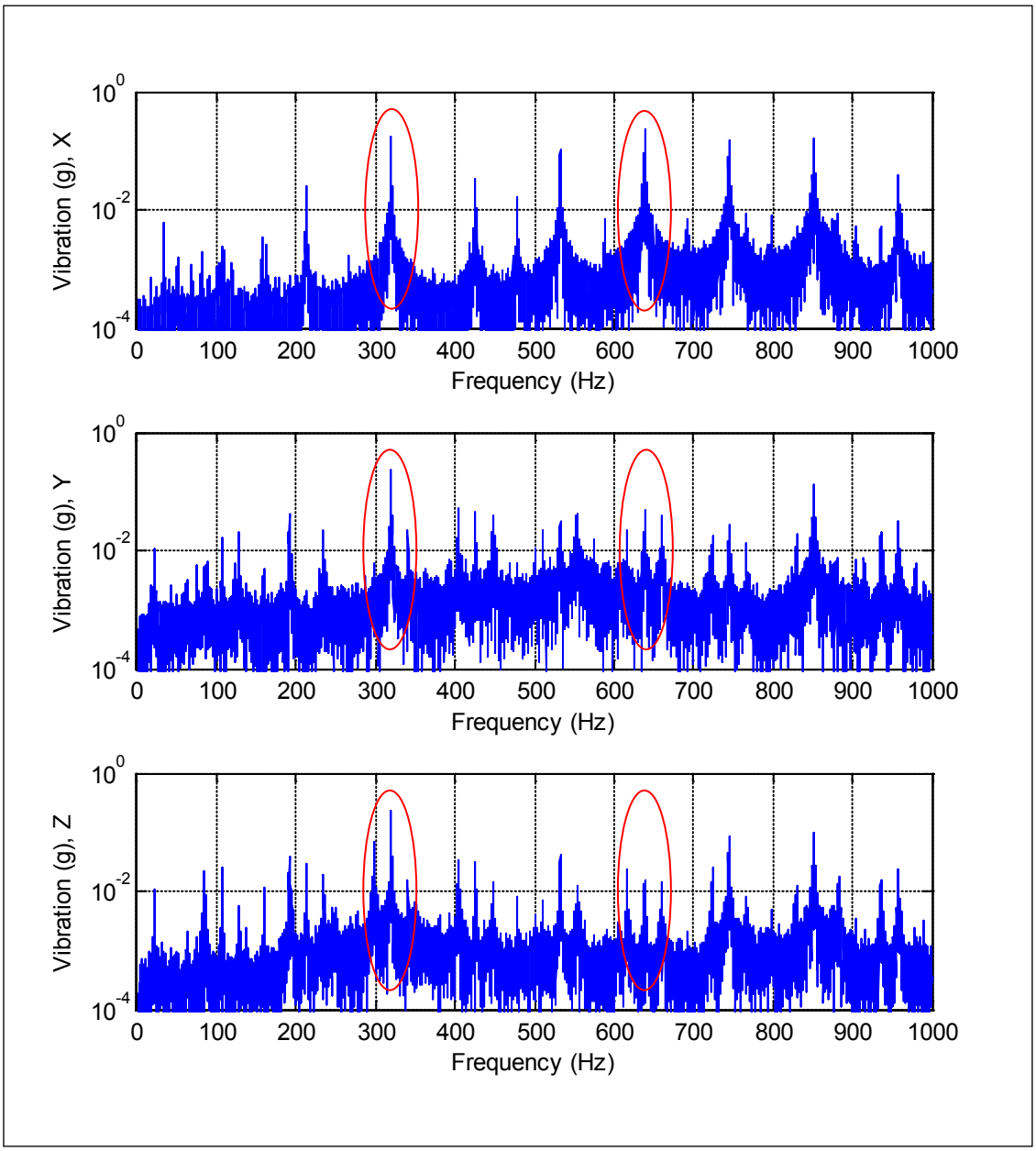

Figure 102. Vibration at rated power, east

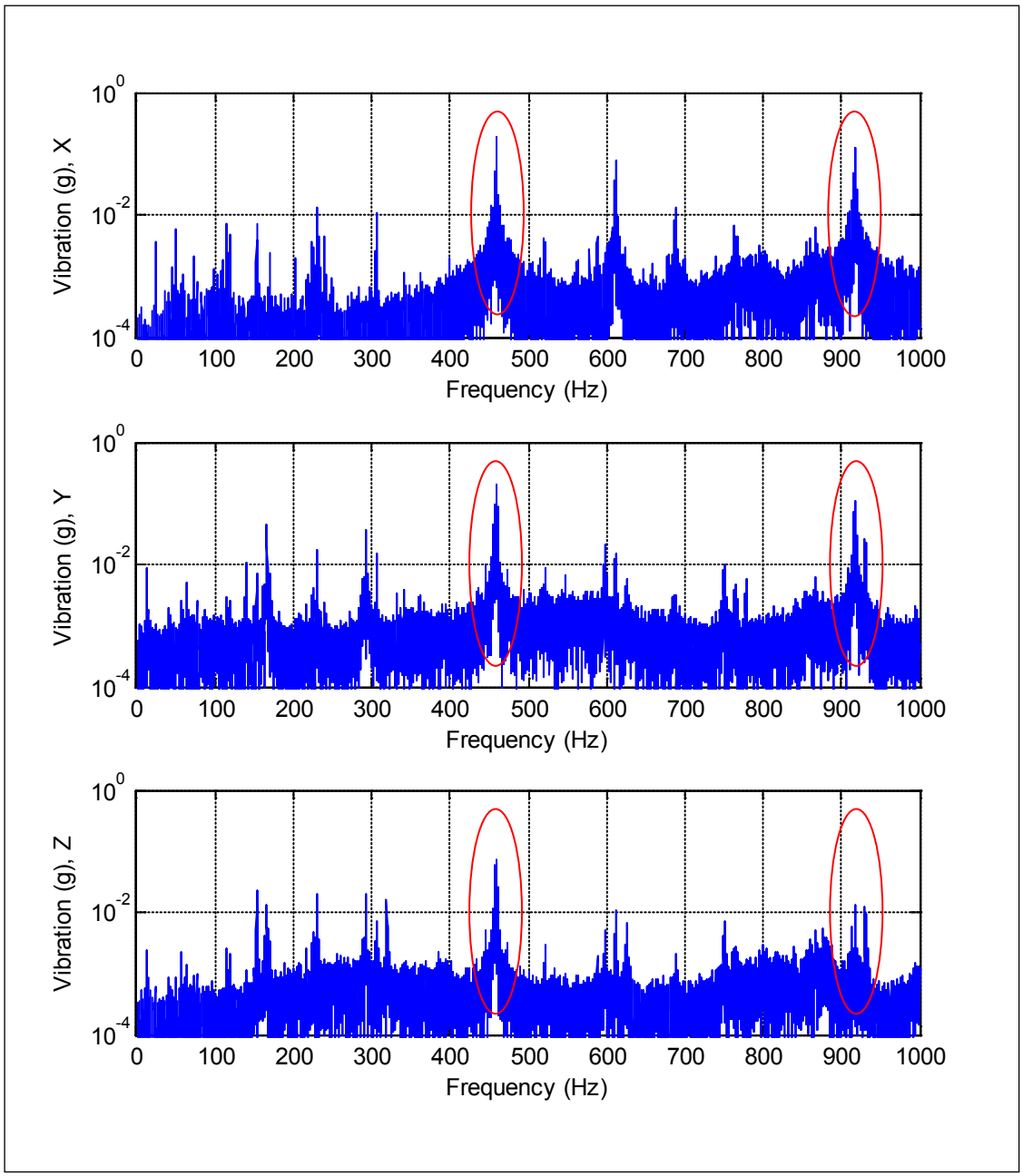

Figure 103. Vibration at rated power, west

Figure 104 and Figure 105 show plots of the gearbox meshing fundamental and second harmonic. There appears to be a resonance in the drivetrain at 800 kW in the Y and Z directions. The meshing fundamental vibration otherwise is flat.

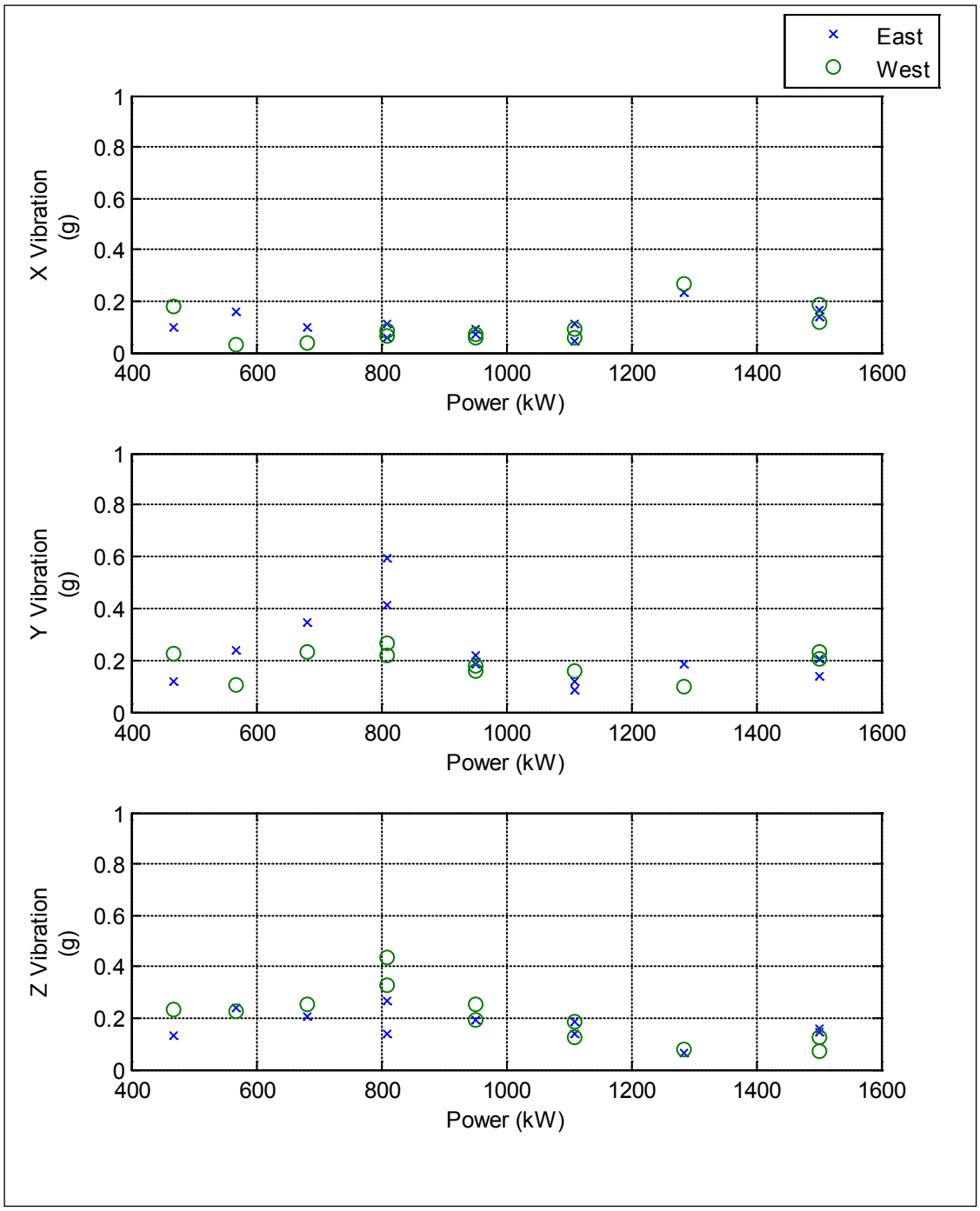

Figure 104. Magnitude of gearbox meshing frequency fundamental

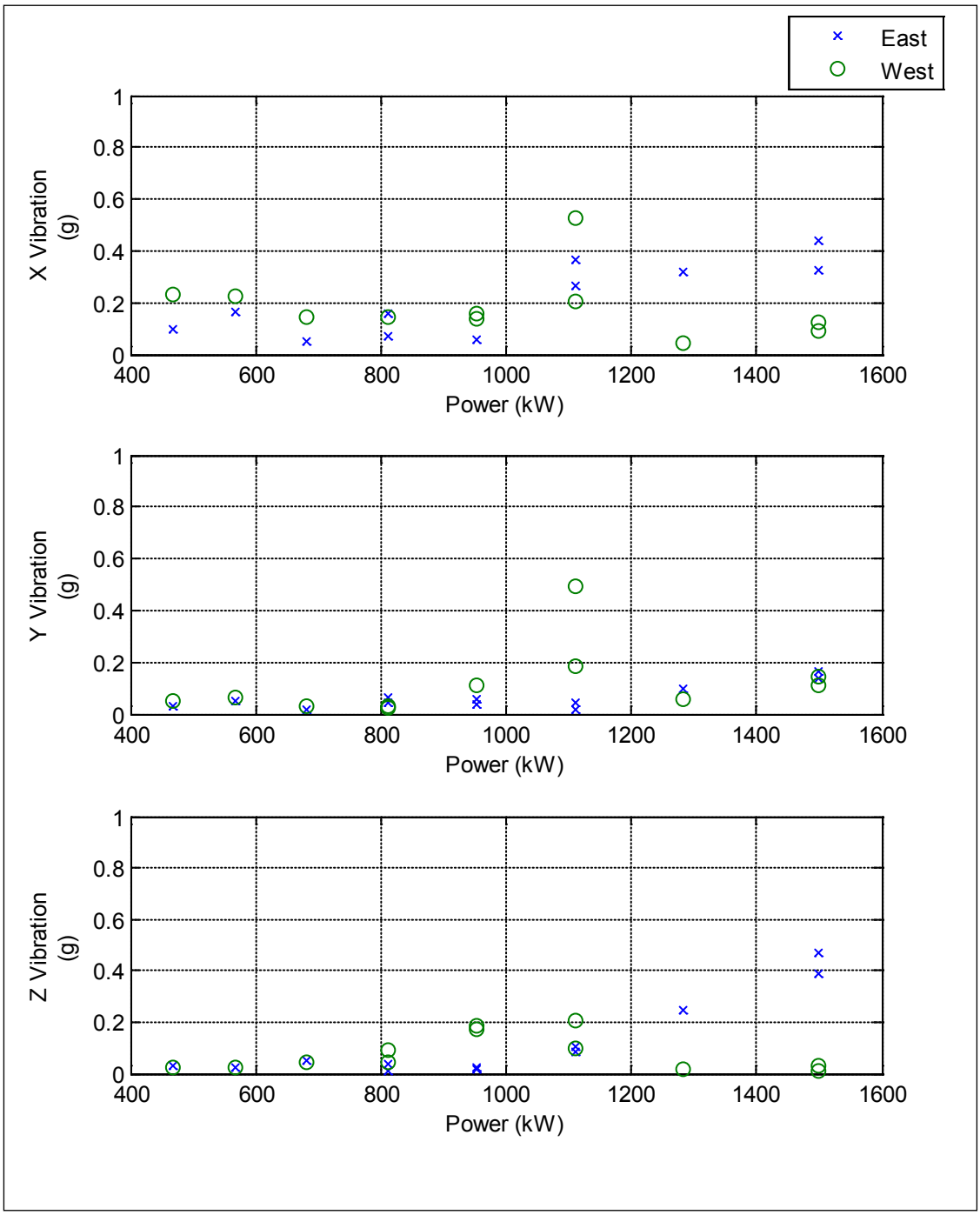

Figure 105. Magnitude of gearbox meshing frequency second harmonic

6 Conclusions

In general, the gearbox functioned as expected. The testing did not reveal any significant issues with the gearbox design or manufacture. The generator was able to operate at rated power but only for a short period before overheating occurred. The greatest power level for which the generator was able to achieve thermal equilibrium at less than the design limits was 1.0 MW.

During testing, the current and voltage levels of the generator were not consistent with the design specifications. The causes of the divergence between the measured and design values of current and voltage identified in this report are the lagging power factor of the generator, reduction in magnet strength with temperature, and increased voltage drop in the stator circuit. The power factor of the generator is immune to changes in temperature; however, the increased current caused by the lagging power factor caused some incremental increase in the loss in the windings. The interaction of the magnet temperature and the voltage and current levels formed a positive-feedback system that exacerbated electrical and thermal deviations from the design specifications.

Testing showed that the reworked series winding temperatures were significantly greater than the original parallel winding temperatures, even though the same cooling system was used for both winding configurations. The elevated series windings temperatures are the result of increased electrical resistance and thermal resistance. The increased electrical resistance amplifies the power loss in the windings, and increased thermal resistance reduces the ability of the cooling system to pull heat from the windings.

Calorimetric efficiency calculations showed greater than expected efficiency losses in the drivetrain, which suggests that the generator's overheating is at least in part caused by increased efficiency loss. A portion of the increased loss can be attributed to the greater than expected current levels. The design of the series windings should be reviewed and compared with test data, however, to ascertain the cause of the generator overheating at power levels greater than 1.0 MW.

The compact design of the drivetrain makes it more power dense than more conventional wind turbine drivetrain designs. The relatively high power density requires careful attention to thermal management. One of the lessons learned is that the design analysis should include perturbations on the system parameters to determine the sensitivity of the system to seemingly slight changes, especially in the case of positive-feedback systems.

Appendix A. Signal Lists

Table A-1. Instrumentation Connected to the Drivetrain Supervisory Controller and Ported to the Dyno Data-Acquisition System (1 Hz)

Measurement	Tag
Bearing lube temperature	BLT
Main bearing temperature	MBT
Dynamometer Test Facility ambient temp	AT
Gearbox case temp	GCT
Generator case heat flux	HF
Generator coolant supply temp	CST
Generator rotor coolant flow rate	RFR
Generator rotor coolant return temp	RRT
Generator stator coolant flow rate	SFR
Generator stator coolant return temp	SRT
Lube flow rate	LFR
Lube pump pressure	LPP
Lube return temperature	LRT
Lube supply pressure	LSP
Lube supply temperature	LST
Main shaft position	MSP
Main shaft speed	MSS
Outside of coil end-turn segment #2 temp	OET2
Inside of coil end-turn segment #2 temp	IET2
End of laminate tooth segment #2 temp	LTT2
Back iron laminate segment #2 temp	BIT2
Cold plate segment #2 temp	CPT2
Outside of coil end-turn segment #5 temp	OET5
Inside of coil end-turn segment #5 temp	IET5
End of laminate tooth segment #5 temp	LTT5
Back iron laminate segment #5 temp	BIT5
Cold plate segment #5 temp	CPT5
Outside of coil end-turn segment #8 temp	OET8
Inside of coil end-turn segment #8 temp	IET8
End of laminate tooth segment #8 temp	LTT8
Back iron laminate segment #8 temp	BIT8
Cold plate segment #8 temp	CPT8
Outside of coil end-turn segment #11 temp	OET11
Inside of coil end-turn segment #11 temp	IET11
End of laminate tooth segment #11 temp	LTT11
Back iron laminate segment #11 temp	BIT11

Measurement	Tag
Cold plate segment #11 temp	CPT11
Generator segment #2 temp	SEG2
Generator segment #3 temp	SEG3
Generator segment #5 temp	SEG5
Generator segment #6 temp	SEG6
Generator segment #7 temp	SEG7
Generator segment #8 temp	SEG8
Generator segment winding #9 temp	SEG9
Generator segment winding #10 temp	SEG10
Generator segment winding #11 temp	SEG11
Rectifier heatsink #1 temp	RHS1
Rectifier heatsink #2 temp	RHS2

Table A-2. Instrumentation Connected to the FastDAS System (2 kHz)

Measurement	Tag
Generator shaft torque	GST
Generator shaft position	GSP
Generator shaft index	GSI
Inverter #1 real power	IP1
Inverter #2 real power	IP2
Main shaft torque	MST
Main shaft speed	MSS
Planet bearing load; 0 degrees upwind	PBL1
Planet bearing load; 0 degrees center upwind	PBL2
Planet bearing load: 0 degrees center	PBL3
Planet bearing load: 0 degrees center downwind	PBL4
Planet bearing load: 0 degrees downwind	PBL5
Planet bearing load: 72 degrees upwind	PBL6
Planet bearing load: 72 degrees center	PBL7
Planet bearing load: 72 degrees downwind	PBL8
Planet bearing roller load	MRL
Planet bearing temperature	PBT
Planet gear displacement inboard	PGD3
Planet gear displacement lagging	PGD4
Planet gear displacement leading	PGD2
Planet gear displacement outboard	PGD1
Planet roller load trigger	MRT
Ring gear strain: 0 degrees upwind	RGS1
Ring gear strain: 0 degrees downwind	RGS2
Ring gear strain: 120 degrees upwind	RGS3

Measurement	Tag
Ring gear strain: 120 degrees downwind	RGS4
Ring gear strain: 240 degrees upwind	RGS5
Ring gear strain: 240 degrees downwind	RGS6
Sun gear axial displacement	SGA
Torque tube axial displacement	TTA
Torque tube radial displacement	TTR
Quadrant #1 phase A current	Q1IA
Quadrant #1 phase B current	Q1IB
Quadrant #1 phase C current	Q1IC
Quadrant #1 line AB voltage	Q1VAB
Quadrant #1 line BC voltage	Q1VBC
Quadrant #1 line CA voltage	Q1VCA
Rectifier #1 DC voltage	R1VDC
Quadrant #2 phase A current	Q2IA
Quadrant #2 phase B current	Q2IB
Quadrant #2 phase C current	Q2IC
Quadrant #2 line AB voltage	Q2VAB
Quadrant #2 line BC voltage	Q2VBC
Quadrant #2 line CA voltage	Q2VCA
Rectifier #2 DC voltage	R2VDC
Quadrant #3 phase A current	Q3IA
Quadrant #3 phase B current	Q3IB
Quadrant #3 phase C current	Q3IC
Quadrant #3 line AB voltage	Q3VAB
Quadrant #3 line BC voltage	Q3VBC
Quadrant #3 line CA voltage	Q3VCA
Rectifier #3 DC voltage	R3VDC
Quadrant #4 phase A current	Q4IA
Quadrant #4 phase B current	Q4IB
Quadrant #4 phase C current	Q4IC
Quadrant #4 line AB voltage	Q4VAB
Quadrant #4 line BC voltage	Q4VBC
Quadrant #4 line CA voltage	Q4VCA
Rectifier #4 DC voltage	R4VDC

Table A-3. Accelerometer Signals

Measurement	Tag
Sensor 1 X direction	X1
Sensor 1 Y direction	Y1
Sensor 1 Z direction	Z1
Sensor 2 X direction	X2
Sensor 2 Y direction	Y2
Sensor 2 Z direction	Z2

Table A-4. Calculated Channels

Measurement	Tag
Generator shaft power	GSP
Generator shaft speed	GSS
Main shaft power	MSP
Quadrant #1 average RMS* current	Q1I
Quadrant #1 average RMS voltage	Q1V
Rectifier #1 RMS voltage	R1V
Quadrant #1 RMS real power	Q1P
Quadrant #1 RMS reactive power	Q1Q
Quadrant #2 average RMS current	Q2I
Quadrant #2 average RMS voltage	Q2V
Rectifier #2 RMS voltage	R2V
Quadrant #2 RMS real power	Q2P
Quadrant #2 RMS reactive power	Q2Q
Quadrant #3 average RMS current	Q3I
Quadrant #3 average RMS voltage	Q3V
Rectifier #3 RMS voltage	R3V
Quadrant #3 RMS real power	Q3P
Quadrant #3 RMS reactive power	Q3Q
Quadrant #4 average RMS current	Q4I
Quadrant #4 average RMS voltage	Q4V
Rectifier #4 RMS voltage	R4V
Quadrant #4 RMS real power	Q4P
Quadrant #4 RMS reactive power	Q4Q

*RMS = root mean squared